

## STAR FORMATION SUPPRESSION DUE TO JET FEEDBACK IN RADIO GALAXIES WITH SHOCKED WARM MOLECULAR GAS

LAURANNE LANZ<sup>1</sup>, PATRICK M. OGLE<sup>1</sup>, KATHERINE ALATALO<sup>2†</sup>, PHILIP N. APPLETON<sup>1,3</sup>

<sup>1</sup> Infrared Processing and Analysis Center, California Institute of Technology, MC100-22, Pasadena, CA 91125, USA; llanz@caltech.edu

<sup>2</sup> Observatories of the Carnegie Institution of Washington, 813 Santa Barbara Street, Pasadena, CA 91101, USA

<sup>3</sup> NASA Herschel Science Center, IPAC, California Institute of Technology, MC100-22, Pasadena, CA 91125, USA

*Draft version September 16, 2021*

### ABSTRACT

We present *Herschel* observations of 22 radio galaxies, selected for the presence of shocked, warm molecular hydrogen emission. We measured and modeled spectral energy distributions in 33 bands from the ultraviolet to the far-infrared to investigate the impact of jet feedback on star formation activity. These galaxies are massive, early-type galaxies with normal gas-to-dust ratios, covering a range of optical and infrared colors. We find that the star formation rate (SFR) is suppressed by a factor of  $\sim 3 - 6$ , depending on how molecular gas mass is estimated. We suggest this suppression is due to the shocks driven by the radio jets injecting turbulence into the interstellar medium (ISM), which also powers the luminous warm H<sub>2</sub> line emission. Approximately 25% of the sample shows suppression by more than a factor of 10. However, the degree of SFR suppression does not correlate with indicators of jet feedback including jet power, diffuse X-ray emission, or intensity of warm molecular H<sub>2</sub> emission, suggesting that while injected turbulence likely impacts star formation, the process is not purely parameterized by the amount of mechanical energy dissipated into the ISM. Radio galaxies with shocked warm molecular gas cover a wide range in SFR–stellar mass space, indicating that these galaxies are in a variety of evolutionary states, from actively star-forming and gas-rich to quiescent and gas-poor. SFR suppression appears to have the largest impact on the evolution of galaxies that are moderately gas-rich.

*Subject headings:* galaxies: active - galaxies: evolution - galaxies: ISM - galaxies: jets - galaxies: star formation

### 1. INTRODUCTION

#### 1.1. AGN Feedback via Radio Jets

Active galactic nucleus (AGN) feedback on the interstellar medium (ISM) is thought to be an important factor in regulating star formation activity in galaxies (e.g., Hopkins et al. 2006). In our current paradigm of galaxy evolution, supported by numerical simulations, feedback can clear galaxies of gas and thereby suppress the star formation activity as well as supermassive black hole growth (e.g. Silk & Rees 1998; Di Matteo et al. 2005). However, our understanding of the details involved and the variety of means via which the AGN can impact its host remains incomplete

One type of feedback is the interaction between radio jets and the ISM, which may have either positive or negative effects on the star formation rate (SFR; Wagner & Bicknell 2011). Hydrodynamical simulations of such interactions have shown that a radio jet may couple strongly to an inhomogeneous, clumpy ISM, injecting turbulence and depositing energy by creating cocoons of hot X-ray emitting gas (Sutherland & Bicknell 2007). The expansion of these bubbles can then spread the effects of the radio jet across the host galaxy. The net effect may suppress star formation by driving shocks and turbulence into the ISM, thereby rendering the molecular gas infertile to star formation, or by driving outflows that can remove the raw materials for new stars (e.g., Guillard et al. 2012). Neutral, ionized, and molecular outflows have all been found in radio galaxies (e.g. Emonts et al. 2005; Feruglio et al. 2010; Mahony et al. 2013; Morganti et al. 2013, 2015; García-Burillo et al. 2014; Alatalo 2015).

Star formation suppression has been conclusively measured, based on resolved molecular observations and detailed modeling of the spectral energy distributions (SEDs) in only a few galaxies. It was demonstrated in NGC 1266, whose AGN has a small radio jet (Nyland et al. 2013) and is driving a massive molecular outflow (Alatalo et al. 2011), where star formation activity is suppressed by a factor of 50–150 (Alatalo et al. 2015b). Karouzos et al. (2013) found hints that radio-loud AGN hosts have a lower SFR than inactive galaxies but could not examine the star formation efficiency. Guillard et al. (2015) recently discussed how the turbulence being injected into the ISM of 3C 326N could explain the quenching of its star formation activity.

#### 1.2. Molecular Hydrogen Emission Galaxies

To study the impact of jet feedback on the star formation activity in their host galaxies, the ideal laboratories are galaxies where we already have evidence of interaction of the jets with the ISM. One class of such galaxies are molecular hydrogen emission galaxies (MOHEGs; Ogle et al. 2007, 2010). These galaxies are identified by the *Spitzer Space Telescope* (Werner et al. 2004) by their high mid-infrared (MIR) H<sub>2</sub> emission relative to their star formation-related emission (24  $\mu$ m or polycyclic aromatic hydrocarbons (PAHs)). Specifically, MOHEGs are defined to have  $L(\text{H}_2\ 0-0\ \text{S}(0)-\text{S}(3))/L(\text{PAH}_{7.7\mu\text{m}}) > 0.04$ , a ratio that is too large to be produced solely by photoelectric heating in photodissociation regions (Ogle et al. 2010). Using this criterion to select galaxies therefore excludes those where the warm molecular emission is predominantly due to heating by star formation activity.

Ogle et al. (2010) explored potential heating mechanisms for this warm molecular emission in a sample of radio galax-

<sup>†</sup> Hubble fellow

ies. They ascertained that X-ray heating by an AGN was insufficient, since these radio galaxies do not contain the high-luminosity, high-ionization AGN necessary. They could not rule out the mechanism of cosmic ray heating but calculated that a very high cosmic ray density would be required to explain the observed  $H_2$  emission. Therefore, they determined that the most likely mechanism was shock heating, which has been seen in radio galaxies (e.g., Labiano et al. 2013; Scharwächter et al. 2013) and is a likely result of the interaction between the radio jet and the ISM. This picture is further supported by the correlation found by Lanz et al. (2015) between the MIR  $H_2$  luminosity and the diffuse X-ray luminosity in radio MOHEGs, as both would be powered by the dissipation of the jet’s mechanical energy into the ISM. Therefore, radio MOHEGs provide an excellent sample for investigating the effect of jet feedback on star formation activity.

We present ultraviolet (UV) to far-infrared (FIR) SEDs of 22 radio MOHEGs, which we use to analyze the properties of the host galaxies. We describe the sample selection and the data analysis, including new *Herschel* photometry, in §2. In §3, we discuss our SED fitting methodology and the caveats involved and test the reliability of our SED-derived parameters. We use these galaxy parameters to examine the colors, ISM properties, and star formation activity of this sample in §4 and summarize our conclusions in §5. We comment on individual galaxies and present the details of UV–FIR images and fitted SEDs in the appendix.

## 2. OBSERVATIONS AND ANALYSIS

### 2.1. Sample

Our sample is derived from the surveys of Ogle et al. (2010; 15 sources) and Guillard et al. (2012; 7 sources) of radio galaxies observed with the *Spitzer* Infrared Spectrograph (IRS; Houck et al. 2004), containing both core-dominated (i.e., FR I; Fanaroff & Riley 1974) and lobe-dominated (FR II) sources. The Ogle et al. galaxies were selected from the 3CRR catalog with a redshift ( $z < 0.13$  for FR I and  $z < 0.22$  for FR II) and flux cuts ( $S_\nu(178 \text{ MHz}) > 15 \text{ Jy}$  for FR I and  $> 16.4 \text{ Jy}$  for FR II). The redshift cut insured that the purely rotational quadrupole transitions  $H_2$  line series (0–0 S(0) to 0–0 S(7)) was observable with IRS. The Guillard et al. galaxies were selected to have neutral outflows and have some sources in common with the Ogle et al. sample.

We specifically focus on those galaxies identified as MOHEGs.<sup>2</sup> Table 1 presents the sample, including their morphologies, environments, and distances. The Guillard galaxies extend the range of star formation activity, but are not systematically different from the Ogle galaxies. Throughout this paper, we assume a cosmology with Hubble constant  $H_0 = 70 \text{ km s}^{-1} \text{ Mpc}^{-1}$ , matter density parameter  $\Omega_M = 0.3$ , and dark energy density  $\Omega_\Lambda = 0.7$  (Spergel et al. 2007). For the two galaxies with  $z < 0.01$ , we use redshift-independent distances calculated by Tonry et al. (2001).

### 2.2. Observations and Data Reduction

In order to examine the properties of the host galaxies of these radio MOHEGs, we created UV–FIR SEDs, based on

<sup>2</sup> Although 3C 31 falls just outside the MOHEG criterion on the  $H_2$ /PAH ratio, Ogle et al. (2010) argued that it should also be called a radio MOHEG, since it has a larger ratio than the SINGS galaxies, but has a lower ratio than most MOHEGs due to strong PAH7.7  $\mu\text{m}$  emission. PKS1549-79 has a similar ratio and likewise has strong PAH7.7  $\mu\text{m}$  emission.

observations from *Galaxy Evolution Explorer* (GALEX; Martin et al. 2005), Sloan Digital Sky Survey (SDSS; York et al. 2000), the 2 Micron All Sky Survey (2MASS; Skrutskie et al. 2006), *Spitzer* (Werner et al. 2004), *Wide-field Infrared Survey Explorer* (WISE; Wright et al. 2010), and *Herschel* (Pilbratt et al. 2010). In the next sections, we describe the reduction we performed on these data. For ease of reading, we confine the details of the observations (Table A1) and measured photometry (Table A2) to the appendix, where we also comment on peculiarities of the individual galaxies and present UV–FIR images and fitted SEDs.

#### 2.2.1. Ultraviolet (GALEX) Photometry

All but two of our galaxies were observed by GALEX. Mosaics of the longest observations were retrieved from the Mikulski Archive for Space Telescopes using GalexView version 1.4.10. In the case of 3C 433, only a near-UV (NUV) observation is available. We used the conversions from count rate to fluxes provided by Goddard Space Flight Center (2004)<sup>3</sup> and corrected for foreground extinction due to the Milky Way dust using the extinction laws given by Wyder et al. (2005) and the  $N_H$  of Kalberla et al. (2005)<sup>4</sup>. Background estimates were measured near each galaxy in source-free regions. Photometric uncertainties consist of the Poisson uncertainty added in quadrature with a 10% calibration uncertainty (Goddard Space Flight Center 2004).

#### 2.2.2. Optical (SDSS) Photometry

Sixteen of our galaxies have SDSS images available in DR12 (Alam et al. 2015). We retrieved mosaics of each galaxy in all five *ugriz* filters from the DR12 Science Archive Server<sup>5</sup>. All were taken in Drift mode with 53.9 s exposure times. We corrected for foreground extinction, using the extinction corrections of Stoughton et al. (2002) with the same  $N_H$  as for the GALEX corrections. Background estimates were measured near each galaxy in source-free regions. Photometric uncertainties consist of the Poisson uncertainty added in quadrature with a 3% (*gri*) or 5% (*uz*) calibration uncertainty (Stoughton et al. 2002). For galaxies lacking SDSS observations (six galaxies), *UBVR* photometry or limits were obtained from the literature (see §2.2.7).

#### 2.2.3. Near-infrared (2MASS) Photometry

Our sample has complete near-infrared (NIR) coverage from 2MASS. We retrieved mosaics from the NASA/IPAC Infrared Science Archive (IRSA), preferably from the Large Galaxy Atlas (Jarrett et al. 2003). The counts measured in the images were converted to magnitudes using the magnitude zeropoints given in the header of each image and then to Janskys using the flux conversions of Cohen et al. (2003b). Background estimates were measured near each galaxy in source-free regions and photometric uncertainties are the sum in quadrature of the uncertainty due the flux conversion factor uncertainty, a calibration uncertainty of 3%, and Poisson uncertainty (Cutri et al. 2006).

#### 2.2.4. Mid-infrared Photometry

<sup>3</sup> [http://galexgi.gsfc.nasa.gov/docs/galex/FAQ/counts\\_background.html](http://galexgi.gsfc.nasa.gov/docs/galex/FAQ/counts_background.html)

<sup>4</sup> Obtained from <http://heasarc.gsfc.nasa.gov/cgi-bin/Tools/w3nh/w3nh.pl>

<sup>5</sup> <http://dr12.sdss3.org./fields>

Table 1  
Sample

Name <sup>a</sup>	Other		$D_L^c$ (Mpc)	Morphology <sup>d</sup>	Environment <sup>e</sup>	Aperture		Size <sup>f</sup>	Available Data <sup>g</sup>
	Names	$z^b$				R.A.(J2000)	Dec.(J2000)		
3C 31	N 383	0.0170	73.8	Ep; I	Close pair	+32:24:45.21	98''.8 × 73''/5(40°) <sup>h</sup>	1,2,3,4,5,6,7,8	
3C 84	N 1275, Per. A	0.0176	76.4	cD+D; I	Perseus CC	+41:30:42.11	84''/2 × 77''/9(27°) <sup>h</sup>	1,2,3,4,5,6,7,8	
3C 218	Hyd. A	0.0549	245	cD; I	Abell780 CC	-12:05:43.39	27''/5 × 23''/9(51°) <sup>h</sup>	1, 3, 4, 5, 6, 7, 8, 10	
3C 236*	...	0.1005	463	E; II	Single	+34:54:10.43	23''/9 × 19''/6(322°)	2,3,4,5,6,7,8, 11	
3C 270	N 4261	0.0074	32.0 <sup>†</sup>	Ep; I	Virgo Member	+05:49:29.63	106''/6 × 90''/4(66°) <sup>h</sup>	1,2,3,4,5,6, 9	
3C 272.1	N 4374, M 84	0.0034	18.0 <sup>†</sup>	Ep; I	Virgo Member	+12:53:12.92	117''/8 × 112''/3(30°) <sup>h</sup>	1,2,3,4,5,6, 9	
4C 12.50*	PKS 1549+12	0.1217	568	S0; II	Merger	+12:17:24.04	33''/0 × 33''/0(0°)	1,2,3,4,5,6,7,8	
3C 293	U 8782	0.0450	199	S0; I	Pair	+13:52:17.821	+31:26:46.50	1,2,3,4,5,6, 9	
MRK 668*	OQ 208	0.0766	347	Sa; CSO	Pair	+14:07:00.400	+28:27:14.70	1,2,3,4,5,6,7,8	
3C 305*	IC 1065	0.0416	184	Ep; I	Single	+14:49:21.625	+63:16:14.43	1,2,3,4,5,6,7,8	
3C 310	VV 204b	0.0538	240	Ep+D; II	Poor cluster	+15:04:57.179	+26:00:58.33	1,2,3,4,5,6,7,8	
3C 315	...	0.1083	501	S0; II	Close pair	+15:13:40.055	+26:07:30.44	2,3, 5,6,7,8	
3C 317	U 9799	0.0345	152	cD+D; I	A2052 CC	+15:52:09.140	+07:01:17.62	1,2,3,4,5,6,7,8	
3C 326N	...	0.0895	409	Ep+D; II	Pair	+15:52:09.140	+20:05:47.24	1,2,3,4,5,6,7,8	
PKS 1549-79*	...	0.1522	725	E; CSO	Single	+15:56:58.900	-79:14:04.30	1, 3, 5, 7,8,9,10	
3C 338	N 6166	0.0304	133	cD; Ip	A2199 CC	+16:28:38.202	+39:33:04.70	1,2,3,4,5,6,7,8	
3C 386	...	0.0169	73.3	E; I	Single	+18:38:26.251	+17:11:49.94	1, 3,4,5,6,7,8	
3C 424	...	0.1270	595	Ep; I	Group	+20:48:12.099	+07:01:17.05	1, 3, 5, 7,8,10	
IC 5063*	...	0.0113	48.8	Ep; II	Pair	+20:52:02.402	-57:04:07.58	1, 3,4,5,6,7,8,10	
3C 433	...	0.1016	468	S0; II	Group	+21:23:44.565	+25:04:27.56	1, 3, 5, 7,8,10	
3C 436	...	0.2145	1060	Ep; II	Single	+21:44:11.700	+28:10:19.00	1,2,3, 5, 7,8	
3C 459*	...	0.2201	1090	Ep; II	Single	+23:16:35.230	+04:05:18.50	1,2,3, 5,6,7,8	

<sup>a</sup> The \* indicates that the source is from Guillard et al. (2012) rather than Ogle et al. (2010).

<sup>b</sup> Redshifts were taken from NED.

<sup>c</sup> Luminosity distance calculated assuming  $H_0 = 70 \text{ km s}^{-1} \text{ Mpc}^{-1}$ ,  $\Omega_M = 0.3$ , and  $\Omega_\Lambda = 0.7$  (Wright 2006; Spergel et al. 2007), except for galaxies at  $z < 0.01$  (<sup>†</sup>), where distances were taken from Tonry et al. (2001).

<sup>d</sup> Host morphology from Ogle et al. (2010): E—elliptical, Ep—peculiar elliptical, cD—cluster dominant, S0—lenticular. The notation “+D” indicates a significant exponential disk component. I or II indicate the Fanaroff & Riley (1974) type of radio jet (p—peculiar), while CSO indicates a compact symmetric object.

<sup>e</sup> Cluster, group, or pair membership from Ogle et al. (2010). CC—cool X-ray core cluster.

<sup>f</sup> Apertures are given as semi-major axis × semi-minor axis (position angle given counter-clockwise from north; see also Section 2.2.6).

<sup>g</sup> The numbers listed correspond to the following observations being available: 1: *GALEX*, 2: *SDSS*, 3: *2MASS*, 4: *Spitzer* IRAC, 5: *WISE*, 6: *Spitzer* MIPS, 7: *Herschel* PACS, and 8: *Herschel* SPIRE. Ancillary literature photometry is also marked if used: 9: *IRAS*, 10: optical, and 11: UV.

<sup>h</sup> Exclusion regions were placed on the companion(s) or nearby background/foreground sources.

<sup>i</sup> These galaxies lie at the center of clusters in a nest with several close companions, which we have excluded; however, as a result we may be excluding some of the source flux or some contamination may remain.

<sup>j</sup> The PACS and SPIRE images have significant background/foreground structure in this aperture, and the galaxy is a point source at *Herschel* wavelength, so we use the point source aperture.

<sup>k</sup> This aperture is smaller than the point source apertures in MIR—FIR, but there is a nearby optically bright point source. Therefore, this aperture is used in UV—NIR bands with larger point source apertures at longer wavelengths.

*Spitzer* IRAC— Sixteen of our galaxies were observed with the Infrared Array Camera (IRAC; Fazio et al. 2004) as part of nine different programs. Pipeline-created mosaics (S18.25.0) were retrieved from the *Spitzer* Heritage Archive. The *Spitzer* fluxes required aperture corrections. We determined the effective radius of each elliptical aperture<sup>6</sup> and used the extended source flux corrections given in the IRAC Instrument Handbook<sup>7</sup>. Background estimates were measured in the same field in regions selected to mimic the content of background and foreground objects in the apertures in the outskirts of the galaxies. Photometric uncertainties consist of the sum in quadrature of the 3% calibration uncertainty, which typically dominates, and the error measured from the uncertainty images (Cohen et al. 2003a).

*WISE*— Our sample has complete coverage by *WISE*. We retrieved mosaics from IRSA. Counts were converted to fluxes via magnitudes using the zeropoints given in the All-Sky Explanatory Supplement (Cutri et al. 2015). *WISE* fluxes require both an aperture and a color correction, depending on the shape of the SED. We first determined which power-law or blackbody model best fits the photometry and then applied those color corrections (Wright et al. 2010). Aperture corrections are given for the default point source aperture (8.25'' for 3.4  $\mu\text{m}$ –12  $\mu\text{m}$  and 16.5'' for 22  $\mu\text{m}$ )<sup>8</sup> in the All-Sky Explanatory Supplement (Cutri et al. 2015), as are point spread function (PSF) images. We derive aperture corrections by measuring the ratio of the flux contained in the default point source aperture in the PSF images to the flux contained in our desired aperture, and multiplying that ratio by the standard correction. Photometric uncertainties consist of the sum in quadrature of the uncertainty in the flux conversion factor, the Poisson uncertainty, and calibration uncertainties of 2.4%, 2.8%, 4.5%, and 5.7%, respectively, in order of increasing wavelength (Cutri et al. 2015).

### 2.2.5. Far-infrared Photometry

*Spitzer* MIPS— Eighteen of our galaxies were observed with *Spitzer*'s Multiband Imaging Photometer (MIPS; Rieke et al. 2004), as part of nine different programs. Pipeline-created mosaics (S18.12.0 or S18.13.0) were retrieved from the *Spitzer* Heritage Archive. At 70 and 160  $\mu\text{m}$ , we use the filtered mosaics, which are better corrected for artifacts and are recommended for point sources, as none of our galaxies are resolved by MIPS at these longer wavelengths. MIPS fluxes require aperture corrections. Aperture corrections at several radii are given in the MIPS instrument Handbook<sup>9</sup>. We estimate the radius as the effective radius of the aperture (see footnote 9) and interpolate between the available aperture corrections. Photometric uncertainties consist of the sum in quadrature of the calibration uncertainty (4% at 24  $\mu\text{m}$  and 15% at 70 and 160  $\mu\text{m}$ ) and the error measured from the uncertainty images (Engelbracht et al. 2007). MIPS 70  $\mu\text{m}$  photometry is only used in the absence of Photoconductor Array Camera and Spectrometer (PACS) 70  $\mu\text{m}$  photometry; MIPS 160  $\mu\text{m}$  photometry is only used in the absence of PACS 160  $\mu\text{m}$  photometry.

*Herschel* PACS— Nineteen of our galaxies were observed with the PACS (Poglitsch et al. 2010) instrument on *Herschel*, which observed at 160  $\mu\text{m}$  in conjunction with either 70  $\mu\text{m}$  or 100  $\mu\text{m}$ . All 19 were observed at 100  $\mu\text{m}$ , but only nine were observed at 70  $\mu\text{m}$ . About 75% were taken as part of a Cycle 1 Open Time (OT1) program on radio jet feedback (P.I. Ogle), but we also use PACS observations taken as part of five other programs. Level 0 data were retrieved from the *Herschel* Science Archive and processed to Level 1 using the calibration trees of version 12.1.0 of the *Herschel* Interactive Processing Environment (HIPE; Ott 2010) to prepare the products necessary to create mosaics using the 2013 July 31 version of Scanamorphos (Roussel 2013). PACS photometry requires both color and aperture corrections. Color corrections are available for a range of blackbody models with temperatures between 5 and 1000 K (Müller et al. 2011); we used the color correction for the blackbody whose temperature best fit our photometry. HIPE contains aperture corrections for 140 different radii. We derive aperture corrections for our elliptical apertures at their effective radii (see footnote 9) by interpolating between the HIPE values. Photometric uncertainties for PACS bands consists the sum in quadrature of a statistical uncertainty based on the background fluctuations (following the method of Dale et al. 2012) and a 10% calibration uncertainty (Paladini et al. 2012). We find good agreement between the MIPS and PACS photometry at 70 and 160  $\mu\text{m}$  for those galaxies observed with both, but preferentially use the PACS photometry where available.

*Herschel* SPIRE— The same nineteen galaxies observed with PACS were also observed with the Spectral and Photometric Imaging Receiver (SPIRE; Griffin et al. 2010), with about 75% taken as part of the OT1 program of P. Ogle. Additional data from four other programs were also used. The data were retrieved from the *Herschel* Science Archive and processed through HIPE using the default pipeline scripts to create Small Map mode mosaics (calibration trees v11.0). SPIRE photometry requires both color and aperture corrections. Color corrections are available for a range of power-law models with indices between  $-4$  and  $5$  and include color-dependent beam shape corrections, since image units are in Jy per beam (Valtchanov 2014). In contrast to PACS, SPIRE documentation only had aperture corrections for its default point source apertures (22'', 30'', and 42'' at 250  $\mu\text{m}$ , 350  $\mu\text{m}$ , and 500  $\mu\text{m}$ , respectively). Therefore, we obtained PSF images<sup>10</sup> and derived aperture corrections in the same manner as for the *WISE* photometry. For seven of the 19 galaxies with SPIRE data, the aperture determined at optical/MIR wavelengths (see §2.2.6) is smaller than the point source aperture at one or more SPIRE bands. In these cases, we measured the SPIRE photometry in the point source aperture instead. Photometric uncertainties consist of the sum in quadrature of a statistical uncertainty calculated in the same manner as for the PACS bands and a 10% systematic uncertainty<sup>11</sup> (Pearson et al. 2014). The *Herschel* photometry of three of our galaxies has previously been published (3C 84 by Mittal et al. 2012, 3C 326N by Guillard et al. 2015, and IC 5063 by Meléndez

<sup>6</sup>  $r_{\text{eff}} = \sqrt{a \times b}$  for semimajor axis  $a$  and semiminor axis  $b$

<sup>7</sup> <http://irsa.ipac.caltech.edu/data/SPITZER/docs/irac/iracinstrumenthandbook/30/>

<sup>8</sup> [http://wise2.ipac.caltech.edu/docs/release/allsky/expsup/sec4\\_4c.html](http://wise2.ipac.caltech.edu/docs/release/allsky/expsup/sec4_4c.html)

<sup>9</sup> <http://irsa.ipac.caltech.edu/data/SPITZER/docs/mips/mipsinstrumenthandbook/50/>

<sup>10</sup> <https://nhscsci.ipac.caltech.edu/sc/index.php/Spire/PhotBeamProfileDataAndAnalysis>

<sup>11</sup> SPIRE literature indicates the calibration uncertainty is 4–5%. However, Pearson et al. (2014), amongst others, argues that aperture photometry is a less reliable method than some of the tools found in HIPE, such as Time-line Fitter, which are not easily applicable to our study, which seeks to use consistent extraction apertures. Therefore, we use a higher systematic uncertainty.

**Table 2**  
Literature Properties

Galaxy	Warm H <sub>2</sub> <sup>a</sup>		Cold H <sub>2</sub>		References <sup>d</sup>	Stellar Size <sup>e</sup> (kpc)	X-rays <sup>f</sup>		Jet Power		References <sup>i</sup>
	Log(L) (erg s <sup>-1</sup> )	Log(M) [M <sub>⊙</sub> ]	H <sub>2</sub> /PAH <sub>7.7μm</sub>	Log(M) [M <sub>⊙</sub> ]			Size <sup>c</sup> (kpc)	Log(L <sub>X,diff</sub> ) (erg s <sup>-1</sup> )	Log(L <sub>X,AGN</sub> ) (erg s <sup>-1</sup> )	S <sub>178MHz</sub> <sup>g</sup> (Jy)	
3C 31	40.32	8.37	0.030	8.95	1.0 (1)	14 × 10 (1)	41.07	40.67	18.3	0.44	(1)
3C 84	41.81	<8.91	0.560	10.47	14.3 × 7.2 (1)	13 × 11 (1)	44.10	42.91	68.2	1.8	(1)
3C 218	41.10	9.30	0.124	9.26	8.5 (2)	14 × 11 (3)	43.67	41.69	228 <sup>j</sup>	54	(2)
3C 236	41.73*	9.26	>0.469	9.31	1.3 (1)	15 × 11 (1)	42.11	43.02	20.5	17	(2)
3C 270	39.30	<7.48	0.096	<6.82	... (4)	11 × 9 (1)	40.96	41.08	53.3	0.30	(2)
3C 272.1	39.01	6.90	0.126	6.77	... (4)	8 (1)	41.46	39.34	21.3	0.037	(1)
4C 12.50	42.50*	10.61	0.213	10.73	4.2 (1)	16 (1)	42.29	43.34	4.60	5.7	(3)
3C 293	41.76	9.57	0.242	10.32	10.6 (1)	19 × 11 (1)	41.39	42.78	13.8	2.2	(1)
MRK 668	41.89*	<9.20	0.104	10.19	... (4)	10 × 7 (1)	41.7	42.5	0.12 <sup>k</sup>	0.058	(3)
3C 305	41.59*	<8.03	0.153	9.31	20.6 × 8.2 (2)	21 × 15 (1)	41.29	41.23	17.1	2.3	(1)
3C 310	40.86	8.23	>0.734	...	... (4)	10 (1)	41.47	40.11	61.0	14	(1)
3C 315	41.83	<8.52	0.625	...	... (4)	10 × 6 (1)	41.47	41.68	20.6	20	(1)
3C 317	40.59	<8.31	>0.707	7.93	2.6 (1)	17 × 10 (1)	43.30	41.30	49.0	4.6	(4)
3C 326N	41.73	9.34	>4.43	9.14	... (4)	10 × 7 (1)	41.37	40.63	22.2	14	(5)
PKS 1549-79	42.61*	<9.93	0.035	...	... (4)	11 (5)	43.1	44.7	22.0 <sup>l</sup>	44	(2)
3C 338	40.59	<8.30	>0.613	7.89	... (4)	12 × 9 (1)	43.45	40.30	51.1	3.7	(1)
3C 386	39.90	<7.60	>0.613	8.21	2.7 (2)	7 × 5 (2)	40.24	39.75	26.1	0.62	(1)
3C 424	41.97	9.52	>3.68	<9.79	... (4)	9 (5)	42.12	42.44	15.9	21	(4)
IC 5063	40.87*	8.94	0.137	8.69	4.6 × 2.3 (3)	7 × 6 (1)	41.34	42.97	7.47 <sup>m</sup>	0.086	(6, 7)
3C 433	42.13	10.36	0.648	<9.90	... (4)	9 (4)	42.62	43.90	61.3	51	(1)
3C 436	42.31	10.21	0.478	...	... (4)	10 × 9 (1)	42.30	43.53	19.4	82	(1)
3C 459	42.38*	<9.96	0.075	...	... (4)	11 (1)	42.80	43.24	30.8	140	(2)

<sup>a</sup> H<sub>2</sub> luminosities (0-0 S(0)-S(3)) marked with \* are from Guillard et al. (2012). All others are from Ogle et al. (2010), corrected as described in those papers for undetected lines. The warm masses are corrected for differences in distance assumptions and come from thermal modeling of the IRS SLEDs. Ratios of the H<sub>2</sub> luminosities to the 7.7 μm PAH luminosities are from the same papers.

<sup>b</sup> Mass is calculated assuming a typical  $\alpha_{\text{CO}} = 4.3 M_{\odot} (\text{K km s}^{-1} \text{pc}^2)^{-1}$ , corresponding to  $X_{\text{CO}} = 2 \times 10^{20} \text{ cm}^{-2} (\text{K km s}^{-1})^{-1}$  (Bolatto et al. 2013).

<sup>c</sup> If a single number is given, it is the radius of the disk. Otherwise, we give semimajor × semiminor axis. (1) extent from resolved CO; (2) extent from IRAC 8 μm; (3) extent from UV; (4) no information on extent, so we assume 1 kpc in radius (see also Section 2.2.8).

<sup>d</sup> References for H<sub>2</sub> masses and extent from CO observations: (1) Okuda et al. (2005); (2) Salomé & Combes (2003); (3) Salomé et al. (2013); (4) Labiano et al. (2013); (5) Okuda et al. (2013); (6) Ocaña Flaquer et al. (2010); (7) Dasys et al. (2014); (8) Labiano et al. (2014); (9) Braine & Dupraz (1994); (10) Nesvadba et al. (2010); (11) Smolčić & Riechers (2011); (12) Saripalli & Mack (2007); (13) Morganti et al. (2013); and (14) Evans et al. (2005).

<sup>e</sup> If a single number is given, it is the radius of the disk. Otherwise, we give semimajor × semiminor axis. Extent from (in order of preference): (1) SDSS g; (2) IRAC 3.6 μm; (3) IRAC 4.5 μm; (4) 2MASS K; or (5) unresolved so we assume 4'' (the 2MASS resolution), corresponding to the sizes given.

<sup>f</sup> Diffuse 0.5–8 keV luminosities as calculated in Lanz et al. (2015), except for Mrk 668 and PKS 1549-79 (see Appendix B). AGN luminosities (2–10 keV) are likewise from Lanz et al. (2015) and references therein.

<sup>g</sup> The 178 MHz flux density on Baars et al. (1977) scale.

<sup>h</sup> Jet power calculated using the formula of Punnsly (2005):  $P_{\text{jet}} = 6.7 \times 10^{44} (1+z)^2 Z^2 S_{178\text{MHz}} \text{ erg s}^{-1}$ , where  $Z = 3.31 - 3.65 \times ((1+z)^4 - 0.203(1+z)^3 + 0.749(1+z)^2 + 0.444(1+z) + 0.205)^{-0.125}$ . Guillard et al. (2012) used the version of equation 2 (defining  $Z$ ) of Punnsly (2005) containing a typographical error, which is corrected in arXiv:astro-ph/0503267 (Punnsly 2015, private communication). The use of the incorrect formula results in a median factor of ~30 difference in the jet power, increasing with proximity.

<sup>i</sup> References for the 178 MHz flux: (1) Laing & Peacock (1980); (2) Kühr et al. (1981); (3) Stanghellini et al. (1998); (4) Kellermann et al. (1998); (5) Laing et al. (1983); (6) Large et al. (1981); and (7) Mauch et al. (2003).

<sup>j</sup> Extrapolated assuming a power-law from measurements at 160 and 468 MHz.

<sup>k</sup> Extrapolated assuming a power-law from measurements at 327, 365, and 610 MHz.

<sup>l</sup> Extrapolated assuming a power-law from measurements at 468 and 960 MHz.

<sup>m</sup> Extrapolated assuming a power-law from measurements at 408 and 843 MHz.

et al. 2014), with which we typically have good agreement.

### 2.2.6. Aperture Determination

For consistency, we sought to use matched apertures across our SEDs. In order to determine the aperture necessary to fully capture both the optical and infrared (IR) emission, we used the SExtractor algorithm (Bertin & Arnouts 1996) to determine Kron apertures in the SDSS and *WISE* images. In the absence of SDSS images, we used the IRAC images. We measured the *ugriz* and *WISE* photometry in the largest SDSS- and *WISE*-derived apertures, determined whether there was a significant difference in the photometry, and examined the extent of the apertures relative to other sources in the field. Using this information, we selected the aperture that captured all the flux at both optical and MIR wavelengths, while minimizing contamination due to foreground or background sources. Some of our galaxies have companions or exist in clusters. We used the results of SExtractor to help define exclusion regions to minimize the contamination to the flux of these other sources. In Table 1, we provide the size and orientation of the apertures used and note which also have exclusion regions applied. 3C 310 and 3C 338 lie in the centers of clusters in a nest of galaxies, making it particularly difficult to exclude all of the flux from neighboring galaxies without removing flux from the host galaxy. Therefore, the photometry of these galaxies should be treated with caution. Similarly, 3C 459 lies near an optically bright foreground star. Therefore, the best aperture at short wavelengths is quite small in order to minimize contamination. At longer wavelengths, we use the (larger) recommended point source apertures. The measured photometry and upper limits ( $3\sigma$ ) are given in Table A2.

### 2.2.7. Literature Photometry and Properties

Table A2 also gives the photometry we gathered from the literature. We only use *Infrared Astronomical Satellite* (*IRAS*) photometry when PACS data are lacking, particularly at  $70\ \mu\text{m}$ . For those galaxies without optical images from SDSS, we first searched for *UBV* photometry in the Third Reference Catalog (RC3; de Vaucouleurs et al. 1991). Thereafter, we used the NASA Extragalactic Database (NED)<sup>12</sup> to find *UBVR* photometry available in the literature. Since these photometry were not measured in the same aperture we used, we only use these data if they agree with the shape of the SED traced by measured UV and NIR photometry and with larger uncertainties than reported to reduce the weight of these points in our fits. Only 3C 236's lack of UV photometry from *GALEX* can be remedied by existing literature photometry, in this case from the *Hubble Space Telescope* (Tremblay et al. 2010). For galaxies without IRAC or MIPS observations, we obtained photometry at 8 and  $24\ \mu\text{m}$  estimated from the IRS spectra as part of the IRS enhanced products in the Spitzer Heritage Archive. These galaxies are typically at sufficiently high redshift that the whole galaxy is contained within the slit.

We also collected CO-derived molecular masses and extents from the literature. We corrected these masses for discrepancies in the distances assumed in these papers and here. Much uncertainty still remains on the precise conversion, and its dependence on galactic parameters such as metallicity (e.g., Narayanan et al. 2012; Bolatto et al. 2013) or radiation intensity (e.g. in (ultra-)luminous IR galaxies; Bolatto et al. 2013, and references therein), between CO lu-

minosity (or integrated line intensity,  $I_{\text{CO}}$ ) and the associated mass (or column) of molecular hydrogen, which is typically accumulated in the  $\alpha_{\text{CO}}$  (or  $X_{\text{CO}}$ ) parameter. The literature-derived CO masses were calculated with a variety of  $\alpha_{\text{CO}}$  or  $X_{\text{CO}}$ , so we also adjusted these masses to assume a common  $\alpha_{\text{CO}} = 4.3 M_{\odot} (\text{K km s}^{-1} \text{pc}^2)^{-1}$  equivalent to  $X_{\text{CO}} = 2 \times 10^{20} \text{cm}^{-2} (\text{K km s}^{-1})^{-1}$  (Bolatto et al. 2013). The resulting masses are given in Table 2. We also give warm molecular masses and luminosities, as well as the ratio in luminosity between  $\text{H}_2$  and PAHs.

Table 2 also summarizes the X-ray and radio properties of these galaxies. Lanz et al. (2015) measured the diffuse X-ray emission, excluding the AGN, for the 20 galaxies from this sample that had *Chandra* observations. Since that paper, an observation of Mrk 668 (Obs. ID 16071) has become public and was analyzed in an identical manner. PKS 1549-79 has only been observed with *XMM-Newton*, which has much poorer spatial resolution. For this galaxy, we fit the spectrum with a thermal component (effectively our diffuse emission) and an absorbed power-law (effectively the AGN). Appendix B provides additional details of this reduction. In the last columns of Table 2, we also give the jet power calculated with the formula of Punsly (2005) from the 178 MHz flux density.

### 2.2.8. Extent of the Star-forming Region

The most difficult aspect of localizing galaxies on the Kennicutt-Schmidt (K-S; Kennicutt 1998) plot of the surface density of star formation versus the surface density of molecular gas is measuring the surface area. Although 17 of our 22 galaxies have CO line intensities or limits, only six of these were observed with instruments capable of spatially resolving the molecular emission (typically an interferometer). For these galaxies, we assume, as is commonly done, that the extent of the star-forming region is the same as that of the molecular disk. For an additional four galaxies, we can estimate the extent based on the size of the PAH (IRAC  $8\ \mu\text{m}$ ) or UV emission as a proxy. For the rest, no information on the extent of the star-forming disk exists within current observations. Since these galaxies are typically early-type galaxies (ETGs), we use the typical radius of 1 kpc measured in ATLAS<sup>3D</sup> galaxies (Davis et al. 2014). Further, Davis et al. (2013) found that ATLAS<sup>3D</sup> typically had a CO radius  $\sim 20\%$  of the stellar extent radius, which for our galaxies correspond to 1–2 kpc. The position of these galaxies on the K-S diagram should be taken as preliminary, pending resolved molecular observations. The sizes we use, and from where they were determined, are given in Table 2.

## 3. SED FITTING

### 3.1. Method

To estimate SFR, stellar and dust masses, and dust temperatures, we used the SED fitting code MAGPHYS (da Cunha et al. 2008). MAGPHYS fits SEDs with a combination of UV–NIR stellar spectral libraries from Bruzual & Charlot (2003) and a simple, physically motivated model for IR emission from dust developed in da Cunha et al. (2008). It models the ISM as a mix of diffuse dust interspersed with denser, warmer stellar birth clouds. The IR dust libraries have five components: a fixed PAH spectrum shape derived from the M17 SW star-forming region (Madden et al. 2006), a NIR continuum associated with the PAH emission modeled by a modified blackbody ( $\beta = 1$ ) at 850 K, a hot MIR continuum modeled by the sum of two modified blackbodies ( $\beta = 1$ ) at 130 K and 250

<sup>12</sup> <https://ned.ipac.caltech.edu/>

**Table 3**  
Galaxy Parameters

Galaxy	MAGPHYS <sup>a</sup>						AGN	
	$M_*$ ( $10^{11} M_\odot$ )	SFR ( $M_\odot \text{ yr}^{-1}$ )	$L_{\text{Dust}}$ ( $10^{10} L_\odot$ )	$M_{\text{Dust}}$ ( $10^7 M_\odot$ )	$T_{\text{Warm}}$ (K) <sup>b</sup>	$T_{\text{Cold}}$ (K) <sup>c</sup>	$\alpha^d$	$\text{Log}(\nu L_\nu)$ ( $6\mu\text{m}; L_\odot$ )
3C 31	2.95 <sup>+0.07</sup> <sub>-0.07</sub>	0.162 <sup>+0.004</sup> <sub>-0.001</sub>	0.871 <sup>+0.006</sup> <sub>-0.026</sub>	1.32 <sup>+0.27</sup> <sub>-0.14</sub>	39.8 <sup>+9.6</sup> <sub>-6.3</sub>	20.8 <sup>+0.5</sup> <sub>-0.8</sub>	2.0	42.3
3C 84	2.40 <sup>+0.06</sup> <sub>-0.40</sub>	7.76 <sup>+0.31</sup> <sub>-4.11</sub>	10.2 <sup>+0.5</sup> <sub>-5.6</sub>	11.0 <sup>+6.9</sup> <sub>-6.5</sub>	59.6 <sup>+0.1</sup> <sub>-0.1</sub>	19.4 <sup>+0.4</sup> <sub>-0.1</sub>	3.0	43.6
3C 218	1.45 <sup>+0.25</sup> <sub>-0.10</sub>	3.63 <sup>+0.08</sup> <sub>-0.68</sub>	2.19 <sup>+0.05</sup> <sub>-0.15</sub>	7.76 <sup>+0.89</sup> <sub>-0.68</sub>	39.2 <sup>+8.3</sup> <sub>-1.4</sub>	15.4 <sup>+0.1</sup> <sub>-0.2</sub>	...	...
3C 236	1.00 <sup>+1.51</sup> <sub>-0.26</sub>	0.251 <sup>+0.876</sup> <sub>-0.217</sub>	2.88 <sup>+1.90</sup> <sub>-0.31</sub>	10.7 <sup>+1.8</sup> <sub>-4.4</sub>	55.2 <sup>+3.6</sup> <sub>-6.1</sub>	18.3 <sup>+0.7</sup> <sub>-0.5</sub>	2.3	43.5
3C 270 <sup>e</sup>	0.91 <sup>+0.53</sup> <sub>-0.58</sub>	0.0794 <sup>+0.0206</sup> <sub>-0.0519</sub>	0.0813 <sup>+0.0187</sup> <sub>-0.0254</sub>	0.0724 <sup>+0.1181</sup> <sub>-0.0537</sub>	46.6 <sup>+9.0</sup> <sub>-10.6</sub>	21.4 <sup>+2.6</sup> <sub>-3.9</sub>	2.0	41.7
3C 272.1 <sup>e</sup>	0.79 <sup>+0.44</sup> <sub>-0.19</sub>	0.0437 <sup>+0.0288</sup> <sub>-0.0327</sub>	0.0794 <sup>+0.0097</sup> <sub>-0.0308</sub>	0.0661 <sup>+0.1201</sup> <sub>-0.0510</sub>	44.0 <sup>+9.3</sup> <sub>-9.5</sub>	21.3 <sup>+2.7</sup> <sub>-4.0</sub>	2.0	41.3
4C 12.50	2.45 <sup>+0.36</sup> <sub>-0.06</sub>	24.5 <sup>+0.6</sup> <sub>-18.9</sub>	182 <sup>+9</sup> <sub>-153</sub>	100. <sup>+1</sup> <sub>-49</sub>	59.7 <sup>+0.1</sup> <sub>-1.2</sub>	15.8 <sup>+0.1</sup> <sub>-0.6</sub>	3.0	44.5
3C 293	0.65 <sup>+0.29</sup> <sub>-0.25</sub>	0.871 <sup>+0.453</sup> <sub>-0.195</sub>	3.31 <sup>+0.40</sup> <sub>-0.49</sub>	2.00 <sup>+0.58</sup> <sub>-0.92</sub>	58.4 <sup>+0.8</sup> <sub>-4.7</sub>	24.1 <sup>+0.3</sup> <sub>-1.6</sub>	1.6	43.1
MRK 668	0.91 <sup>+0.04</sup> <sub>-0.02</sub>	1.23 <sup>+0.08</sup> <sub>-0.01</sub>	17.4 <sup>+0.8</sup> <sub>-0.1</sub>	6.46 <sup>+0.18</sup> <sub>-0.29</sub>	54.9 <sup>+1.9</sup> <sub>-11.3</sub>	24.7 <sup>+0.2</sup> <sub>-0.1</sub>	2.0	44.6
3C 305	0.93 <sup>+0.27</sup> <sub>-0.40</sub>	0.295 <sup>+1.157</sup> <sub>-0.007</sub>	2.75 <sup>+0.88</sup> <sub>-0.57</sub>	2.24 <sup>+0.33</sup> <sub>-0.20</sub>	45.8 <sup>+6.4</sup> <sub>-8.8</sub>	23.8 <sup>+0.4</sup> <sub>-1.0</sub>	2.5	43.1
3C 310 <sup>e</sup>	2.24 <sup>+0.05</sup> <sub>-0.69</sub>	0.0398 <sup>+0.0002</sup> <sub>-0.0207</sub>	0.0741 <sup>+0.0003</sup> <sub>-0.0078</sub>	0.0776 <sup>+0.0604</sup> <sub>-0.0239</sub>	42.7 <sup>+11.0</sup> <sub>-9.0</sub>	22.7 <sup>+1.6</sup> <sub>-2.0</sub>	...	...
3C 315	0.25 <sup>+0.01</sup> <sub>-0.06</sub>	2.00 <sup>+0.05</sup> <sub>-0.65</sub>	1.82 <sup>+0.04</sup> <sub>-0.12</sub>	1.12 <sup>+0.83</sup> <sub>-0.45</sub>	55.5 <sup>+3.2</sup> <sub>-6.5</sub>	20.4 <sup>+2.2</sup> <sub>-2.3</sub>	...	...
3C 317	3.39 <sup>+0.08</sup> <sub>-1.44</sub>	0.513 <sup>+0.002</sup> <sub>-0.169</sub>	0.891 <sup>+0.006</sup> <sub>-0.155</sub>	0.309 <sup>+0.001</sup> <sub>-0.068</sub>	58.7 <sup>+0.1</sup> <sub>-0.1</sub>	23.3 <sup>+0.1</sup> <sub>-0.1</sub>	...	...
3C 326N	1.55 <sup>+0.04</sup> <sub>-0.04</sub>	0.087 <sup>+0.106</sup> <sub>-0.046</sub>	0.454 <sup>+0.249</sup> <sub>-0.157</sub>	0.605 <sup>+0.376</sup> <sub>-0.219</sub>	56.6 <sup>+2.4</sup> <sub>-6.2</sub>	20.8 <sup>+1.4</sup> <sub>-1.8</sub>	...	...
PKS 1549-79	0.23 <sup>+0.62</sup> <sub>-0.13</sub>	38.0 <sup>+23.6</sup> <sub>-15.6</sub>	112 <sup>+62</sup> <sub>-14</sub>	12.0 <sup>+3.7</sup> <sub>-2.3</sub>	53.5 <sup>+4.7</sup> <sub>-5.8</sub>	23.7 <sup>+1.0</sup> <sub>-2.4</sub>	2.0	45.2
3C 338 <sup>f</sup>	2.00 <sup>+0.05</sup> <sub>-0.09</sub>	0.603 <sup>+0.004</sup> <sub>-0.024</sub>	0.339 <sup>+0.002</sup> <sub>-0.014</sub>	0.871 <sup>+0.006</sup> <sub>-0.589</sub>	...	...	...	...
3C 386	0.20 <sup>+0.02</sup> <sub>-0.04</sub>	0.0794 <sup>+0.0865</sup> <sub>-0.0716</sub>	0.132 <sup>+0.009</sup> <sub>-0.020</sub>	0.191 <sup>+0.072</sup> <sub>-0.043</sub>	57.4 <sup>+1.9</sup> <sub>-3.0</sub>	19.5 <sup>+0.9</sup> <sub>-1.0</sub>	...	...
3C 424 <sup>e</sup>	0.26 <sup>+0.20</sup> <sub>-0.11</sub>	0.0501 <sup>+0.0879</sup> <sub>-0.0363</sub>	0.324 <sup>+0.105</sup> <sub>-0.054</sub>	3.55 <sup>+0.72</sup> <sub>-1.26</sub>	48.2 <sup>+8.2</sup> <sub>-11.0</sub>	15.4 <sup>+0.7</sup> <sub>-0.3</sub>	2.0	42.9
IC 5063	0.40 <sup>+0.02</sup> <sub>-0.08</sub>	0.759 <sup>+0.356</sup> <sub>-0.004</sub>	3.16 <sup>+1.30</sup> <sub>-0.01</sub>	1.91 <sup>+1.06</sup> <sub>-0.01</sub>	60.0 <sup>+0.1</sup> <sub>-1.0</sub>	19.4 <sup>+0.1</sup> <sub>-0.1</sub>	3.0	43.4
3C 433	1.12 <sup>+0.03</sup> <sub>-0.38</sub>	3.63 <sup>+0.65</sup> <sub>-0.15</sub>	9.55 <sup>+0.00</sup> <sub>-0.43</sub>	2.57 <sup>+0.04</sup> <sub>-0.10</sub>	59.9 <sup>+0.1</sup> <sub>-0.1</sub>	24.7 <sup>+0.1</sup> <sub>-0.1</sub>	2.4	44.3
3C 436	1.55 <sup>+0.49</sup> <sub>-0.14</sub>	0.427 <sup>+0.031</sup> <sub>-0.322</sub>	4.57 <sup>+0.22</sup> <sub>-0.31</sub>	3.31 <sup>+0.58</sup> <sub>-0.29</sub>	46.4 <sup>+7.8</sup> <sub>-9.1</sub>	24.4 <sup>+0.4</sup> <sub>-0.8</sub>	2.0	43.4
3C 459	0.36 <sup>+0.01</sup> <sub>-0.02</sub>	195 <sup>+5</sup> <sub>-48</sub>	182 <sup>+4</sup> <sub>-23</sub>	28.8 <sup>+5.2</sup> <sub>-0.5</sub>	59.8 <sup>+0.1</sup> <sub>-0.1</sub>	24.6 <sup>+0.1</sup> <sub>-0.1</sub>	3.0	44.1

<sup>a</sup> Uncertainties take into account both the uncertainty in the best fit as well as the variation during the iterative fitting.

<sup>b</sup> Warm component restricted to 30–60 K and assumes  $\beta = 1.5$ .

<sup>c</sup> Cold component restricted to 15–25 K and assumes  $\beta = 2$ .

<sup>d</sup> Power-law index of the AGN model restricted to be between 1 (approximating a face-on torus) and 3 (effectively an edge-on torus).

<sup>e</sup> These SEDs are poorly sampled in the IR and are not very well fit in the FIR, so the parameters should be used with caution.

<sup>f</sup> 3C 338 only has upper limits at  $\lambda > 60 \mu\text{m}$ , so the derived dust mass and luminosity and SFR should be considered upper limits. Similarly, we do not have concrete information on its dust temperatures.

K, a warm (30–60 K) dust component modeled as a modified blackbody ( $\beta = 1.5$ ), and a cold (15–25 K) dust component modeled as a modified blackbody ( $\beta = 2$ ). The warm dust component is assumed to exist both in the diffuse ISM and in denser birth clouds, while the cold dust exists only in the diffuse ISM. The model shape of the different dust components (i.e.  $\beta$ ) is determined based on the likely size of the grains emitting primarily at those temperatures (see da Cunha et al. 2008 for further details).

In order to determine the physical parameters associated with each SED, MAGPHYS combines UV–NIR and IR spectral libraries, each with 50,000 models calculated for a range across each parameter, such that the energy absorbed in the UV/visible regime is re-emitted in the IR. These models are convolved with the response functions of each filter for which the user has provided photometry. MAGPHYS does not so much fit for its derived parameters as determine how well the photometry of each of its models (and their associated parameters) match observations. As a result, in addition to determining which model matches best, MAGPHYS creates probability distribution functions (PDFs) for each of its parameters, indicating the likelihood of its value. The parameters we use in this work are the median of these distributions with the range of parameter values with 16%–84% likelihood providing the

bulk of the uncertainty.

MAGPHYS does not currently include an AGN component, and many of our galaxies have a significant MIR contribution likely due to an AGN. Sajina et al. (2012) described an empirical SED model for UV–FIR SEDs which includes a component associated with AGN tori, modeled as a broken, tapered, power-law:

$$F_{\text{AGN}} = \frac{\nu}{\left(\frac{\nu}{\nu_0}\right)^\alpha e^{0.5\nu} + \left(\frac{\nu}{\nu_0}\right)^{-0.5} + \left(\frac{\nu}{0.3\nu_0}\right)^{-3.0}} \quad (1)$$

The effect of dust sublimation is captured by the exponential tapering, and the  $\nu^{-3}$  component acts as the Rayleigh-Jeans tail of a dust component (with  $\beta = 1$ ), softened by the flatter component ( $\nu^{-0.5}$ ).

Including another component such as this one into MAGPHYS is an endeavor beyond the scope of this paper. Instead, we used an iterative method to fit both the Sajina AGN component and a host galaxy (via MAGPHYS) in order to better model our SEDs. First, we fit the SED purely with MAGPHYS. Then we subtracted the photometry associated with the best MAGPHYS fit and fit the MIR residuals (5–24  $\mu\text{m}$ ) with the Sajina AGN. We fix  $\nu_0$  in order to have a peak in the MIR, within the range used by Sajina et al. (2012). We tried both

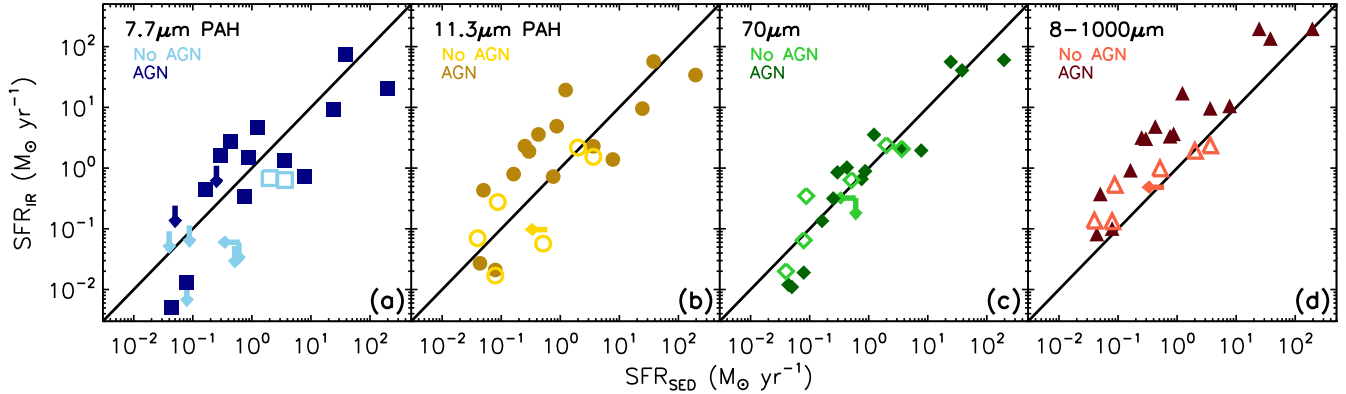


**Figure 1.** Comparison of the SED-derived SFR with SFR calculated from several IR relations, with solid, darker symbols indicating that the SED fit included an AGN component and unfilled, lighter-colored symbols indicating an AGN component did not improve the SED fit. SFRs calculated based on the luminosity of the  $7.7\ \mu\text{m}$  PAH (a) and  $11.3\ \mu\text{m}$  PAH (b) show some dispersion but correlate well with the SED-derived SFR. (c) The SFR calculated from the  $70\ \mu\text{m}$  relation of Calzetti et al. (2010) agrees well with the SED-derived SFR, as the SED at this wavelength is generally dominated by the host galaxy. In contrast, the SFR calculated from the  $8\text{--}1000\ \mu\text{m}$  luminosity ((d) Kennicutt 1998) is often too large, particularly when the SED is better fit with a MIR AGN component.

fits with  $\alpha = 2$  and with a free  $\alpha = [1, 3]$ .<sup>13</sup> The photometry associated with the better AGN fit is subtracted from the observed fluxes, and the resulting photometry is fit again with MAGPHYS.<sup>14</sup> We iterate several times between the MAGPHYS fits and the MIR AGN fits until the MAGPHYS fit no longer improves. If adding the AGN component has not significantly improved the fit, then we use the original (pre-AGN) fit; otherwise we include the AGN component. Fifteen of the 22 SED fits improve significantly with the inclusion of an AGN component. We add the parameter variation seen over the iterations to the uncertainties from the MAGPHYS 16%–84% parameter likelihood range, as a means of estimating the impact of different AGN models on the parameters. Table 3 summarizes the derived parameters.

We tested whether beginning with the AGN component, rather than the host component, affects the fit. When the AGN component is weak (e.g., 3C 31) or moderate (e.g., 3C 236), there is very little difference. For strong AGNs (e.g., IC 5063), fit iterations starting with the AGN component converge to a model with a slightly stronger AGN contribution and an SFR lower by a factor of  $\sim 2$ , within the reliability of our SFR (see §3.2.1). Additionally, if the SFR are indeed lower than those derived with our methodology in the 3–8 of our galaxies with the strongest MIR AGN, then this will only strengthen the results we discuss in §4.2.

We tested the reliability of the AGN contribution by fitting a subset of our sample with another IR-only SED fitting program, DecomIR (Mullaney et al. 2011), which pairs one of five host galaxy templates with a piece-wise AGN model consisting of two power laws and a modified blackbody. Our DecomIR fits of galaxies requiring significant AGN contributions with our fitting method (e.g., 3C 236 and IC 5063) yield AGN fractional contributions to the  $8\text{--}35\ \mu\text{m}$  of  $\sim 75\%$ , similar to the MIR AGN fractions in our fits. Further, DecomIR fits of galaxies where our method does not require an AGN (e.g., 3C 218 and 3C 326N) yield MIR AGN fractions  $< 20\%$ .

### 3.2. Parameter Comparison

<sup>13</sup>  $\alpha = 1$  corresponds approximately to a face-on torus, whereas  $\alpha = 3$  better models edge-on tori.

<sup>14</sup> In some cases, the model photometry in a band is larger than the observed photometry. In these cases, we treat the observed flux as an upper limit in the subsequent fit, which adds substantially to the  $\chi^2$  value if the model of that fit is larger than this data point.

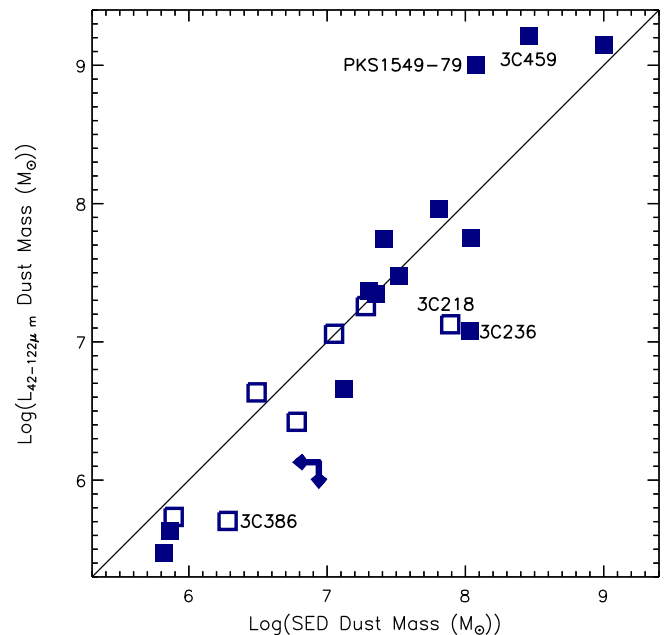


**Figure 2.** Comparison of the SED-derived dust mass with a estimate of dust mass based on the  $42\text{--}122\ \mu\text{m}$  luminosity. Solid symbols include an AGN in the fit. The five labeled galaxies have differences greater than a factor of 3. 3C 459 and PKS 1549–79 are both ULIRGs and peak at shorter wavelengths, corresponding to warmer temperatures. The difference in derived mass for 3C 218, 3C 236, and 3C 386 is more likely due to SEDs dominated by a colder component than the 25 K assumed in the IR luminosity-based estimate of dust mass (see §3.2.2 for further details).

In our examination of galaxy properties, we will use the parameters derived from the SED fitting. Since the SFR, dust mass, and stellar mass will be key properties, we first examine how these SED-derived values compare to those from simpler methods. This comparison will also provide some guidance in future studies with more limited observational data sets.

#### 3.2.1. SFR

Figure 1 shows the comparison of the SFR obtained from the MAGPHYS fit<sup>15</sup> with four other measures of SFR. We examined how the MAGPHYS SFR compares to SFR calculated

<sup>15</sup> MAGPHYS calculates SFR from the average SFR of the last 100 Myr of the star formation history.



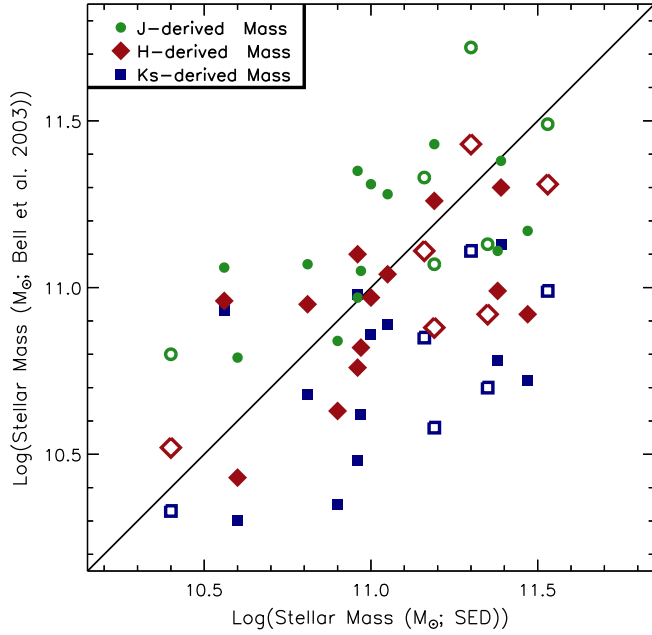


**Figure 3.** Comparison of the SED-derived stellar mass with the mass calculated from a color-dependent mass-to-light relation for the three 2MASS bands. Solid symbols include an AGN in the fit. The SED-derived masses agree best with the  $H$ -band derived masses within a factor of 2.

from the PAH fluxes from Ogle et al. (2010) and Guillard et al. (2012).<sup>16</sup> We find that these SFRs correlate well with the SED-derived values but with dispersions of  $\sim 0.7$  dex (Fig. 1ab). Some of this dispersion may also be due to the fact that the IRS slit did not fully cover the host for all of our galaxies.<sup>17</sup>

One of the most common estimates of SFR is based on the IR luminosity, such as the 8–1000  $\mu\text{m}$  relation of Kennicutt (1998) (Fig. 1d). However, many of these galaxies have sizable MIR contributions likely due to warm dust heated by an AGN. Therefore, it is not surprising that the total IR SFR is biased high compared to the SED-derived value for our galaxies. In contrast, if we only examine FIR emission where the host galaxy dominates (e.g. 70  $\mu\text{m}$ ; Fig. 1c), the SFRs correlate much better with a dispersion of 0.4 dex.

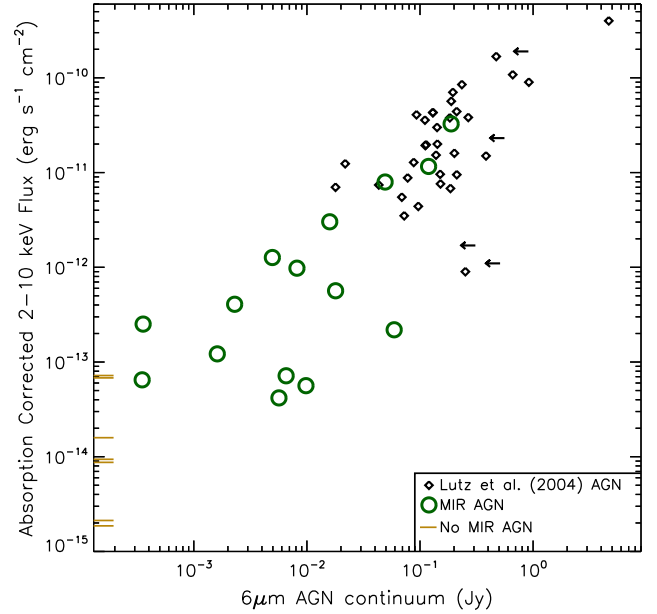
### 3.2.2. Dust Mass

Figure 2 compares the MAGPHYS-derived dust mass with an estimate of the dust mass based on the 42–122  $\mu\text{m}$  luminosity. We assume a simple model of a single modified blackbody with a dust emissivity power-law index of  $\beta = 1.8$  and a typical temperature of 25 K (as suggested for example by Scoville et al. 2014). We find that there is good agreement (dispersion of 0.46 dex), despite the simple assumptions of the second estimate.

The galaxies that deviate the most provide interesting insights on the estimation of dust mass. In Figure 2, we identified the five galaxies whose estimates of dust mass differ by more than a factor of three. The three with lower dust masses in the simple model (3C 218, 3C 236, and 3C 386) all have cold dust temperatures from MAGPHYS

<sup>16</sup> We use the same formulae as Ogle et al. (2010) but with our assumed distances:  $\text{SFR}(\text{PAH}_{7.7\mu\text{m}}) = 2.4 \times 10^{-9} L(\text{PAH}_{7.7\mu\text{m}})/L_{\odot}$  and  $\text{SFR}(\text{PAH}_{11.3\mu\text{m}}) = 9.2 \times 10^{-9} L(\text{PAH}_{11.3\mu\text{m}})/L_{\odot}$ .

<sup>17</sup> This issue was previously noted for a subset of these radio galaxies in the appendix of Alatalo et al. (2015b).



**Figure 4.** Comparison of the SED-derived 6  $\mu\text{m}$  AGN continuum flux with the 2–10 keV AGN flux, showing that our galaxies fall along the correlation seen for more luminous AGN by Lutz et al. (2004).

below 20 K. Since dust mass varies with dust temperature as  $M_D \propto T^{-(4+\beta)}$ , a decrease in temperature from 25 to 20 K increases the derived dust mass by a factor of 3.6 (assuming  $\beta = 1.8$ ). PKS 1549-79 and 3C 459 are two of our three ultra-luminous IR galaxies (ULIRGs), which tend to have typically hotter dust (e.g., Clements et al. 2010) and therefore peak at shorter wavelengths than less luminous galaxies. As a result, the dust mass derived from their 42–122  $\mu\text{m}$  luminosity is overestimated. The third ULIRG, 4C 12.50, is well fit by a 15.8 K cold dust temperature, so the two effects cancel out. Similarly, 3C 84 has a temperature just under 20 K, but it has a relative high luminosity as a luminous IR galaxy (LIRG). We conclude that the SED-derived values provide a good estimate of the dust masses due to the ability of this method to fit multiple thermal components.

### 3.2.3. Stellar Mass

We also compare the MAGPHYS-derived stellar mass determined based on the star formation history associated with the best fit model with masses calculated from a color-dependent mass-to-light relation (Fig. 3; Bell et al. 2003). We use  $g-r$  colors if we have SDSS observations, or  $B-V$  colors if available, along with the luminosity in the three 2MASS bands.<sup>18</sup> We find good agreement with  $H$ -band derived masses, which are intermediate between the  $J$ -band and  $K_s$ -band masses, with a dispersion of 0.26 dex. The dispersion across the set of 2MASS-derived masses is 0.32 dex. We do not see significant differences between the best fits of those galaxies better modeled with and without a MIR AGN.

### 3.2.4. AGN

Approximately two-thirds (15/22) of our sample was better fit with the inclusion of a MIR AGN component. Lutz et al.

<sup>18</sup> The Bell et al. (2003) relations assume a different initial mass function than MAGPHYS, but the effect on the mass calculated is small ( $< 1\%$  difference).

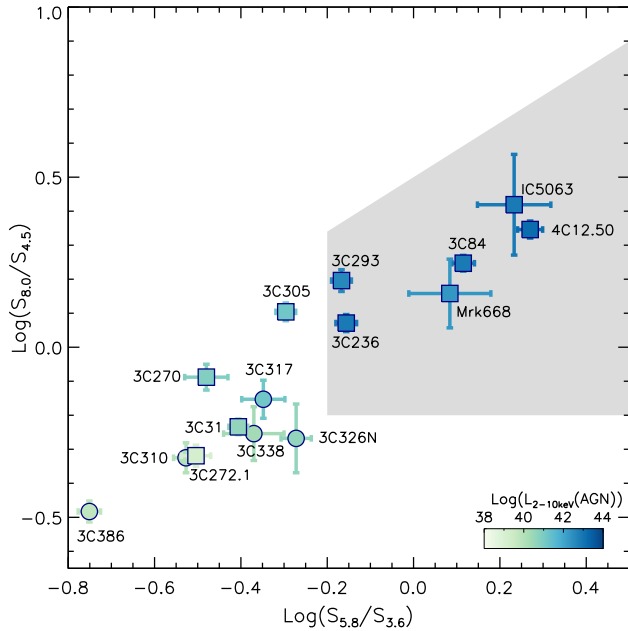


**Figure 5.** The  $S_{5.8\mu\text{m}}/S_{3.6\mu\text{m}}$  versus  $S_{8.0\mu\text{m}}/S_{4.5\mu\text{m}}$  IRAC colors with the AGN-dominated region defined by Lacy et al. (2004) shown in light gray. AGNs with X-ray (2–10 keV) luminosities (which defines the color of the points) all fall within the “Lacy” wedge. However, not all MIR AGNs (squares) do.

(2004) found a correlation between  $6\mu\text{m}$  and 2–10 keV fluxes and luminosities (see also Goulding et al. 2011). In Figure 4, we find that our galaxies broadly fall along this correlation, despite our AGN being typically weaker than those looked at by Lutz et al. (2004). Those galaxies whose SEDs do not require a MIR AGN have the lowest hard X-ray flux. This test bolsters the dependability of our SED decomposition.

We also examine the IRAC colors of our galaxies in Figure 5. Only fifteen galaxies were observed with all four bands of IRAC, but we find that those galaxies with the most X-ray luminous AGN all fall within the region identified by Lacy et al. (2004) as AGN-dominated. Four galaxies whose SEDs are best fit with a MIR AGN fall outside this wedge, but these are amongst the weakest in our sample in both their X-ray and IR emission associated with an AGN.

### 3.3. Caveats

We discuss individual peculiarities of each galaxy in Appendix A, but there several common caveats, which we discuss below.

#### 3.3.1. MIR Spectral Variations

MAGPHYS includes a PAH component via the use of a template based on the spectrum of the star-forming region M17 SW (Madden et al. 2006; da Cunha et al. 2008). Therefore, it assumes a particular ratio between the different PAH lines, which is kept fixed. For example, this template has a  $7.7\mu\text{m}/11.3\mu\text{m}$  ratio of  $\sim 3.9$ .<sup>19</sup> In our sample, that ratio ranges from 0.73–5.0 with a median value of 2.3 (Ogle et al. 2010). This difference in ratios may explain fit discrepancies in IRAC  $8\mu\text{m}$  and *WISE*  $12\mu\text{m}$  bands (e.g., the fits of 3C 218 and 3C 386 show an excess of modeled PAH emission in the long-wavelength IRAC bands.) However, the PAH

<sup>19</sup> Based on a PAHFIT (Smith et al. 2007) fit of the template.

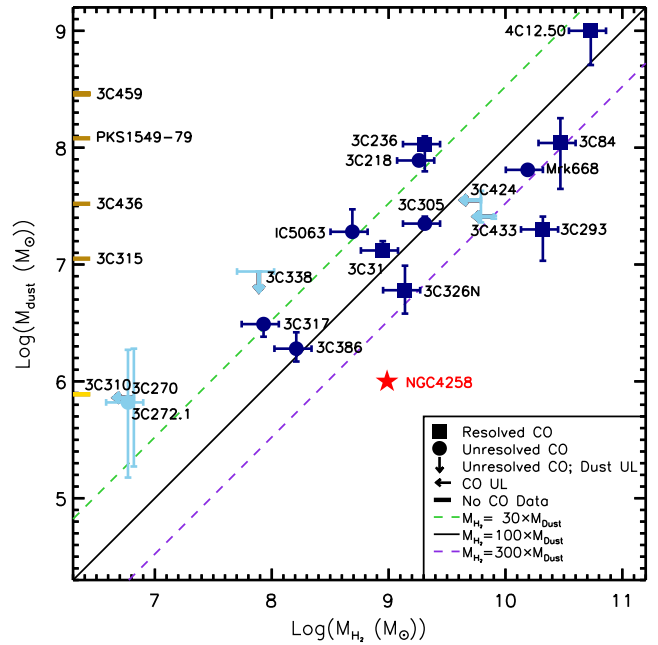


**Figure 6.** Molecular gas mass (calculated with a common  $X_{\text{CO}} = 2 \times 10^{20} \text{ cm}^{-2} (\text{K km s}^{-1})^{-1}$ ) compared to the dust mass derived from the SED fits. Most of our galaxies have normal GDRs, although 3C 293 has a particularly high ratio (Lanz et al. 2015; Papadopoulos et al. 2008 has suggested its CO emission is enhanced by shocks). Darker symbols have more reliable dust masses. 3C 270 and 3C 272.1, in particular, should be used with caution. For comparison, we show the MOHEG NGC 4258 (red star) discussed by Ogle et al. (2014).

component contributes very little to the dust mass (da Cunha et al. 2008 estimates it contributes at most a few percent), and the SFR is primarily influenced by the UV and FIR emission. Therefore, the uncertainty introduced by this fixed PAH ratio has little impact on the final estimated SFRs and dust masses. Similarly, the spectra of our galaxies (Ogle et al. 2010) show a range of silicate emission and absorption at  $10\mu\text{m}$ , which is not taken into account in our fitting. However, like the PAH features, this spectral component will not greatly affect the SFRs and dust masses we derive.

#### 3.3.2. FIR Excess

Several of our galaxies show excess emission over the Rayleigh-Jeans tail of the MAGPHYS dust continuum, likely due to one of two causes. First, since our sample consists of radio galaxies, we would not be surprised to detect synchrotron emission, possibly even at wavelengths observed with *Herschel*. However, analysis of one of these SEDs (3C 84) by Leipski et al. (2009) concluded that there was little synchrotron contribution to the FIR emission. Second, these galaxies could contain additional dust cooler than the 15 K limit of MAGPHYS. MAGPHYS does not currently contain either a synchrotron component or another cooler dust component, and adding a new component would require generating many new models. The good agreement between our SED-derived SFRs and the  $70\mu\text{m}$  SFR (where this excess is not present), as well as the good match of our fits to the FIR peaks, suggests that the impact of this unmodeled component is unlikely to have a significant impact on our SFR. There may be a more important impact on the dust mass, as a cold component could contribute significant additional mass. However, an increase in dust mass would only strengthen the results we discuss in §4.2.

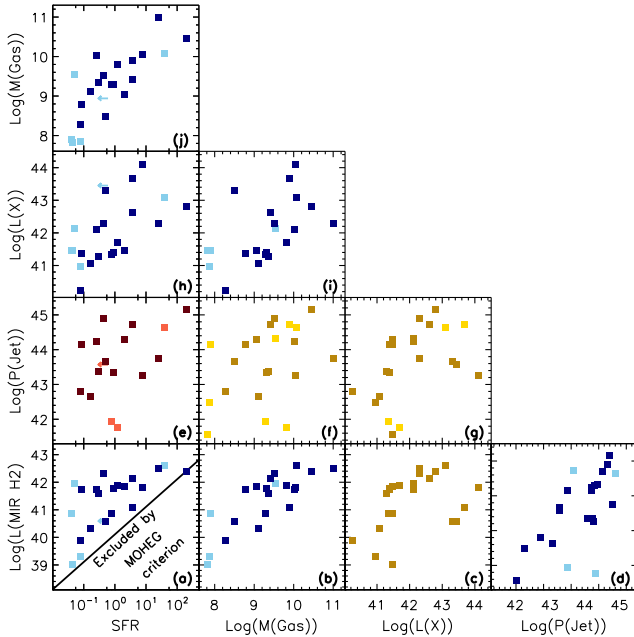


**Figure 7.** Comparison of galaxy and feedback properties:  $\text{H}_2$  luminosity from IRS ( $\text{erg s}^{-1}$ ) in the S(0)–S(3) lines; SFR from MAGPHYS ( $M_{\odot} \text{ yr}^{-1}$ ); cold molecular mass calculated from the dust mass ( $M_{\odot}$ ); diffuse X-ray luminosity ( $\text{erg s}^{-1}$ ) in the 0.5–8 keV band; and jet power ( $\text{erg s}^{-1}$ ). Blue symbols have significant correlations ( $p < 0.01$ ) and yellow symbols indicate suggestive correlations ( $p < 0.05$ ), calculated based on darker symbols that have more secure parameter values.

### 3.3.3. Limited SED Coverage

A minority of our galaxies have limited FIR coverage. Three were not observed with *Herschel*. In the case of 3C 293, the combination of MIPS and *IRAS* photometry yields a good fit, but for 3C 270 only two of these bands are detected. Its SED, as well as that of 3C 272.1, are not well fit in the FIR, so their parameters are used with caution. 3C 338 and 3C 310 were both observed with *Herschel*, but were either not detected or their FIR emission could not be disentangled from those of close companions that appear to dominate at these wavelengths. Since 3C 310 has one FIR data point, we use its derived parameters with caution, but given the complete lack of photometric detections of 3C 338 at  $\lambda > 30 \mu\text{m}$ , we consider its derived SFR, dust mass, and dust luminosities to be upper limits.

In the UV regime, only one galaxy, 3C 315, has no data. However, five others only have upper limits (although these are used to restrict the fits). PKS 1549-79 has a well defined SED in the IR, but only has one (literature-derived) UV-optical data point. 3C 424 likewise has a poorly sampled SED overall, so its parameters should be treated with caution and have large uncertainties associated with them.

The parameters associated with these fits are more uncertain than those from better sampled SEDs. Therefore, in the figures that follow, we indicate them with lighter symbols to guide the reader in determining which data points are more reliable.

## 4. DISCUSSION

### 4.1. ISM Properties

Given the uncertainty in the conversion factor from CO luminosity to molecular gas mass, we assume a common  $X_{\text{CO}}$  ( $2 \times 10^{20} \text{ cm}^{-2} (\text{K km s}^{-1})^{-1}$ ; Bolatto et al. 2013) to calculate the gas mass in all the galaxies for which literature CO

observations exist (Table 2). Figure 6 compares this gas mass to the dust mass we derive from the SED fits. Most of our galaxies have gas-to-dust ratios (GDRs) within a factor of a few of the typical ratio found in the Milky Way ( $\sim 100$ ). The most extreme ratio is found in 3C 293 ( $\sim 10^3$ ; Lanz et al. 2015). Higher excitation CO lines have been measured in that galaxy (Papadopoulos et al. 2008), whose spectral line energy distribution (SLED) is consistent with shock-excitation. As a result, the assumed  $X_{\text{CO}}$  could be too high, as this galaxy could emit more CO per amount of molecular mass than a galaxy whose CO is not shocked. Papadopoulos et al. (2010) further argued that the effect of shock-induced turbulent heating would have a much larger effect on the gas phase than on the dust phase. Similarly a high GDR was seen in the inner regions of NGC 4258, shown for comparison in Figure 6, where warm  $\text{H}_2$  was mapped along the axis of the radio jet (Ogle et al. 2014).

Based on Figure 6, however, such an apparently high GDR does not appear to be a common property of all radio MOHEGs. 3C 293 is not clearly peculiar in the parameters we have examined. It lies in the middle of the range of both galaxy parameters (e.g. SFR, stellar mass, and dust mass) and feedback-associated parameters (e.g. jet power,  $\text{H}_2$  luminosity, and diffuse X-ray luminosity), and like many of our sample, it has a companion. It is therefore difficult to identify the cause of the particularly large shock-excitation in 3C 293, although the relative geometry of the jet and molecular gas distribution may play a role. Further exploration of the CO SLED of the full sample would also provide greater insight into whether any others also show indications of shock-excitation in the higher CO lines.

We also examine whether galaxy properties, including ISM properties such as GDR and gas fraction, correlate with properties potentially related to jet feedback, such as the diffuse X-ray luminosity (which may be powered by dissipation of mechanical energy of the jet into the ISM) and the jet power. We show in Figure 7 the subset that shows significant or suggestive correlations, as calculated with the Spearman’s rank correlation statistic<sup>20</sup> (Press et al. 1986). We do not find significant correlations for either the GDR or the gas fraction, except with  $\text{H}_2$  luminosity, which is likely due to the strong correlations of all three of these parameters with the gas mass (Fig. 7b). We also do not find that the fitted cold dust temperature correlates with any other galaxy property.

This sample was selected in part based on the presence of  $\text{H}_2$  emission in the purely rotational 0–0 lines in the MIR, so our galaxies all contain significant warm molecular emission. Table 2 gives the luminosities of this component, measured in the S(0)28.2  $\mu\text{m}$ –S(3)9.66  $\mu\text{m}$  lines, which ranges from  $7 \times 10^{38} - 8 \times 10^{42} \text{ erg s}^{-1}$ . For most of our galaxies, the bulk of this gas is at  $\sim 100\text{K}$  and comprised between 5% and 80% of the molecular reservoir (see also Ogle et al. 2010). We do not find correlations between the fraction of gas in the warm component and proxies of jet feedback. Fig. 7a shows that the  $L(\text{H}_2)$ –SFR parameter space not excluded by the MOHEG criterion is approximately uniformly covered by our galaxies, suggesting that the correlation is a selection effect. In contrast, the correlations of  $L(\text{H}_2)$  with jet power (Fig. 7d,  $p \sim 0.008$ ) and diffuse X-ray luminosity (Fig. 7c,  $p \sim 0.027$ ; see also Lanz et al. 2015) supports the interpretation that these two luminosities are powered by the dissipa-

<sup>20</sup> We used the `r_correlate` routine in IDL. A  $p$ -value less than 0.05 is suggestive; when  $p$ -values are less than 0.01 the correlation is more significant.

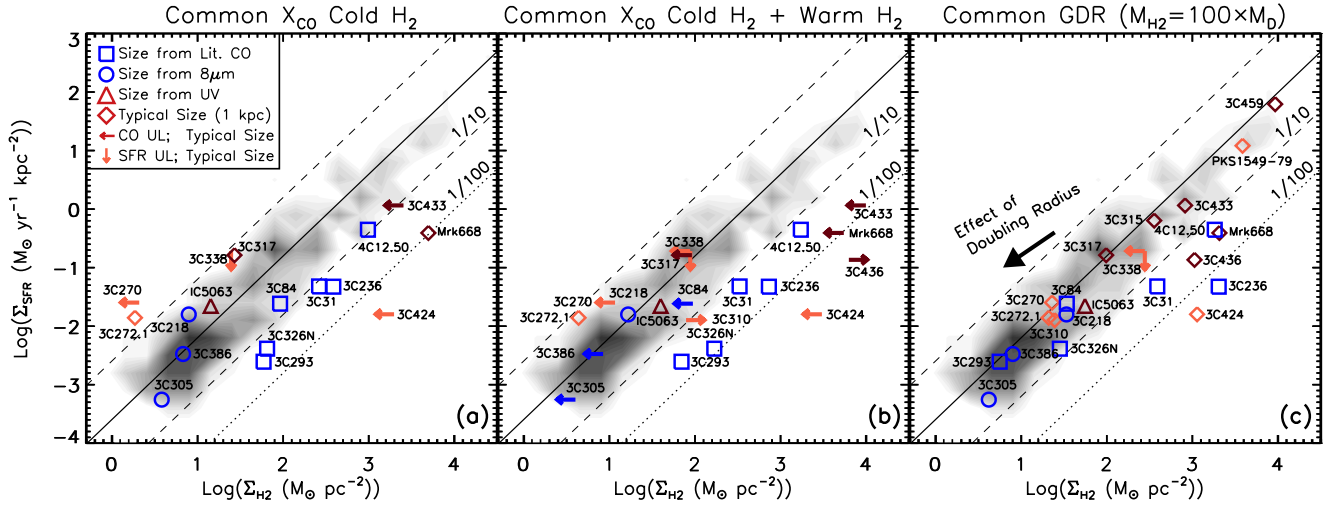


**Figure 8.** Surface density of star formation compared to surface density of molecular gas (K–S diagrams; Kennicutt 1998; the solid line is the K–S relation) calculated (a) from CO luminosity assuming a common  $X_{\text{CO}}$  ( $2 \times 10^{20} \text{ cm}^{-2} (\text{K km s}^{-1})^{-1}$ ), (b) for the total (cold as in a + warm) molecular gas, or (c) a common GDR. The lower limits on total gas surface density are for those galaxies that have not been observed in CO. For comparison, the underlying grayscale contours show the typical extent of normal galaxies (spirals from Kennicutt 1998 and Fisher et al. 2013, CO-detected ETGs from Davis et al. 2014, and the Shi et al. 2011 galaxies). We find that MOHEGs tend to fall on the suppressed side of the typical relation, but only three (3C 31, 3C 236, and Mrk 668) have suppressions greater than a factor of ten in all three K–S plots (3C 436 unfortunately does not have CO data). Darker symbols have more reliable SFRs and dust masses.

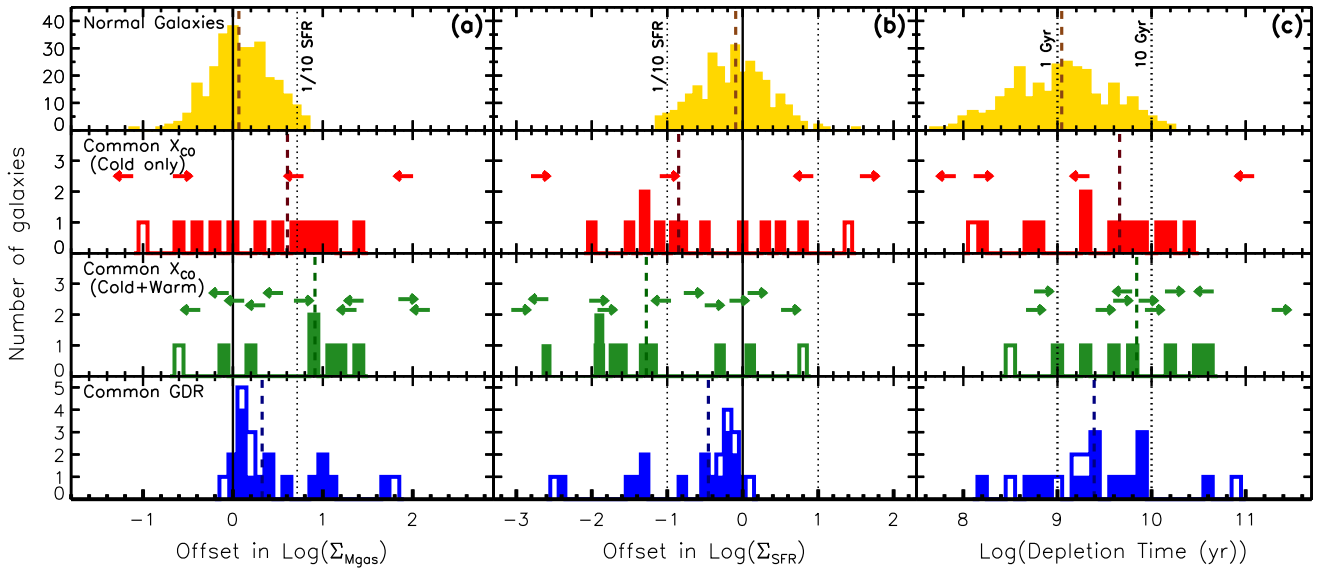


**Figure 9.** Histograms comparing the distributions of offsets from the K–S relation (a, b) in Figure 8 and the depletion times of the molecular reservoir (c). The dashed line shows the median of each sample. In the lower three rows, the filled histograms correspond to the darker symbols of Figure 8, whose SFR and dust mass are more reliable. These histograms show that the median offset (or depletion time) is typically larger (by about a factor of two) when molecular mass are calculated from CO luminosity than from dust mass; adding the warm gas mass further increases the offset. The dust-mass based values have a smaller dispersion and more clearly show an overall shift to lower SFR.

tion of the jet’s mechanical energy into the ISM. We do not find correlation between the  $\text{H}_2/\text{PAH}$  ratio and either galaxy or feedback properties, suggesting that while this ratio is indicative of shocked gas, it may not be a good proxy for the strength of jet feedback.

#### 4.2. Star Formation Suppression in Radio MOHEGs

To account for the uncertainty in  $X_{\text{CO}}$  factor and the incomplete availability of molecular observations of our sample, we calculate molecular gas masses and surface densities as well as the associated depletion times in three different ways: (1) from the CO luminosity assuming a common  $X_{\text{CO}}$  as described earlier, (2) from the sum of the CO-derived

cold molecular mass (i.e. method 1) and the warm molecular mass calculated by Ogle et al. (2010) or Guillard et al. (2012), and (3) from the dust mass assuming a common GDR of 100 (which Fig. 6 shows to be a reasonable estimate). In Figure 8, we plot all three derived molecular surface densities against the surface density of star formation on the K–S (Kennicutt 1998) diagram, compared to the relation found by those authors of  $\Sigma_{\text{SFR}} \propto \Sigma_{\text{gas}}^{1.4}$ . For comparison, we also show contours of normal galaxies from Kennicutt (1998), Fisher et al. (2013), and Shi et al. (2011) and CO-detected ETGs from Davis et al. (2014), whose gas masses and SFRs have been corrected to assume the same  $X_{\text{CO}}$  and initial mass function as our measurements. These galaxies largely have SFRs

within a factor of ten of the predicted value from the K–S relation.

We find that the K–S diagrams show a tendency for radio MOHEGs to lie below the K–S relation. When assuming a common  $X_{\text{CO}}$ , the observed star formation suppression appears larger, with a clustering around a suppression of SFR by a factor of ten. However, the scatter is fairly large, and particularly at low molecular surface densities (e.g.  $\lesssim 30 M_{\odot} \text{pc}^{-2}$ ), what remains of our sample would appear to be in agreement with normal galaxies. Since the cooling timescale of warm  $\text{H}_2$  is short ( $10^4$  years; Guillard et al. 2009) and this gas mass may therefore be quickly available to form stars, we also placed our galaxies on the K–S diagram using the total gas mass (both cold from CO luminosity and warm from IRS observations; Fig. 8b). The primary effect is to increase the gas mass and the derived star formation suppression.

Since our sample was selected to have indications of jet-driven turbulence in the ISM, we might imagine that some (or all) of these galaxies could likewise have CO further excited by the warm, turbulent medium, perhaps resulting in more CO emission on average per mass of molecular gas. Therefore, we also place galaxies on the K–S diagram using a gas mass calculated from the dust mass assuming a common GDR (Fig. 8c). We find a smaller scatter with the bulk of our sample falling between the K–S relation and a suppression of SFR by a factor of ten (within the wings of the comparison sample of normal galaxies). However, given that most of our galaxies cluster around a normal GDR (e.g., Sandstrom et al. 2013) when assuming a typical relation between CO luminosity and molecular mass, the offset we see for many of these galaxies is unlikely to be purely explained by the use of an inaccurate  $X_{\text{CO}}$ . To test this effect, however, we examine the significance of offsets both for the complete sample and without including those galaxies with GDR larger or smaller than typical by a factor of five.

Figure 9 shows histograms of the offsets from the K–S relation in both axes for each sample, quantifying the tendencies we have described above. When assuming  $X_{\text{CO}}$  (cold gas only), we find offsets of factors of  $\sim 3$  and  $\sim 6$  in surface density of molecular gas and SFR, respectively, with scatters of 0.85 and 1.2 dex. Adding the warm component to the molecular reservoir, drives the median offsets to large factors of  $\sim 8$  and  $\sim 18$ , although these medians do not taken into account the numerous limits. If we only look at the subset of galaxies with the normal GDR, the median offsets change little; if we require the GDR to be even closer to normal GDR, the median offsets become further different from the comparison population. Finally, the median offsets are smaller with common GDR (factors of  $\sim 2$  and  $\sim 3$ ), but the scatter is smaller (0.75 and 1.0 dex). The GDR histograms show that our sample has a large fraction with only slight suppression but with a long tail.

We calculate the Wilcoxon–Mann–Whitney (WMW)<sup>21</sup> and Kolmogorov–Smirnov (KS)<sup>22</sup> statistics, comparing our samples to the normal galaxies. Comparing the cold  $X_{\text{CO}}$  set with the normal galaxies, both statistics find a suggestive indication that the samples do not come from a common parent distribution (WMW:  $p = 0.044$ ; KS:  $p = 0.0090$ ). There are too few galaxies with accurate total (cold+warm) molecular masses for the WMW statistics to provide a meaning-

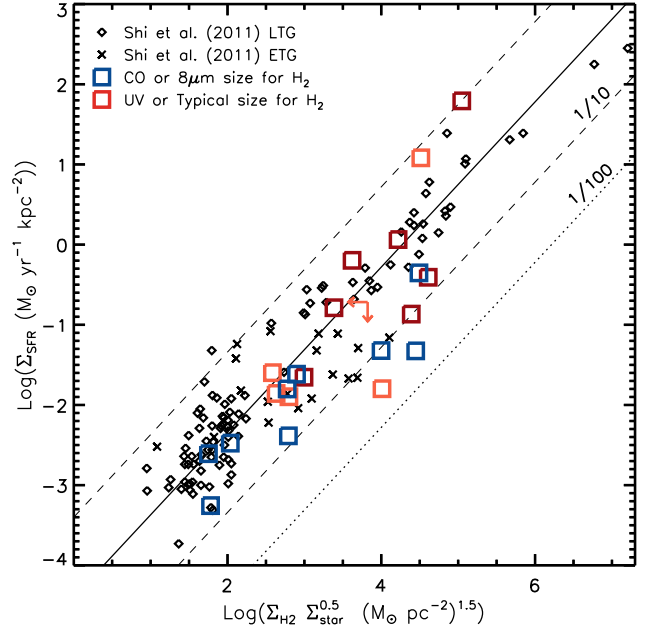


**Figure 10.** Surface density of star formation compared to surface density of molecular gas and stellar mass (extended Schmidt law; Shi et al. 2011). For comparison, the small black symbols show the Shi et al. (2011) galaxies. Radio MOHEGs lie below the Shi relation, which may also be due to their hosts being ETGs, although the lenticular ETGs looked at by Shi et al. (2011, crosses) have higher sSFRs (Fig. 11). Darker symbols have more reliable SFRs and dust masses.

ful assessment, but the KS statistics shows, as expected, a greater departure from the distribution of the normal galaxies ( $p = 0.0022$ ). As with the median comparisons, if we exclude those galaxies with GDRs that deviate from typical, we still find statistical differences compared to the normal galaxies (WMW:  $p = 0.03$ ; KS:  $p = 0.004 - 0.02$ ). For the larger GDR set, the WMW shows a significant difference from the normal galaxies ( $p = 0.00054$ ), while the KS statistic is only suggestive ( $p = 0.0064$ ). If we increase the assumed radius where we do not know the molecular extent to 2 kpc, the significance decreases but is still suggestive (WMW:  $p = 0.016$ ; KS:  $p = 0.06$ ).

Three galaxies show consistent suppression by more than a factor of ten in all three K–S plots. While 3C 31 is fairly consistent in its position, 3C 236 shows a suppression (a factor of  $\sim 20$ ) based on its CO-derived cold molecular mass, but it has a low GDR, so when a common GDR is assumed, it is pushed past a factor of 200. The extent of the molecular disk in the third galaxies, Mrk 668, is currently unknown. Assuming a typical radius of 1 kpc, its SFR is suppressed by a factor of 30–95. As the arrow on Figure 8c shows, a change in the assumed radius does not quite move galaxies purely along the K–S relation. Instead, an increase in radius also acts to reduce any suppression observed. For Mrk 668, we calculate it would need a molecular disk of radius  $\geq 3.6$  kpc to bring it back in the range of normal galaxies (i.e. within a factor of 10 of the K–S relation) in the most conservative mass estimate, on the edge of the range of radii (1–4 kpc) found by Davis et al. (2013) for CO-emitting ETGs, suggesting this galaxy is likely to have a large degree of suppression.

3C 436, which has not been observed in CO, has a surface density of star formation and molecular gas that suggest a star formation suppression by a factor of  $\sim 30$ , requiring a disk with a radius of 4.2 kpc to bring 3C 436 within a factor of

<sup>21</sup> IDL routine RS\_TEST

<sup>22</sup> IDL routine kstwo

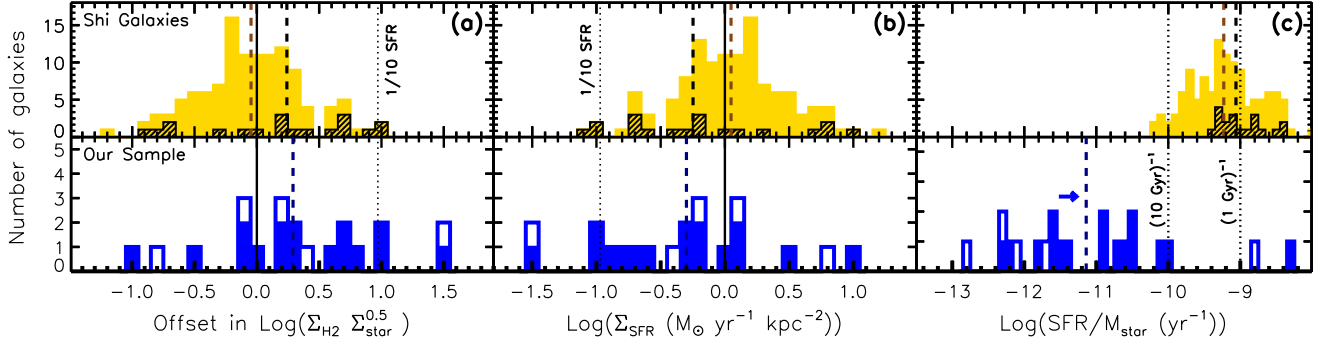


**Figure 11.** Histograms comparing the distributions of offsets (a, b) in Figure 10, as well as the sSFR (c). The dashed line shows the median of each sample. For the Shi et al. (2011) galaxies, we also highlight the ETGs with the black, hashed histograms. In the lower row, the filled histograms correspond to the darker symbols of Figure 10, whose SFR, dust mass, and stellar mass are more reliable. Our galaxies have a similar distribution to the Shi ETGs, but their sSFR are noticeably smaller than those of the Shi sample.

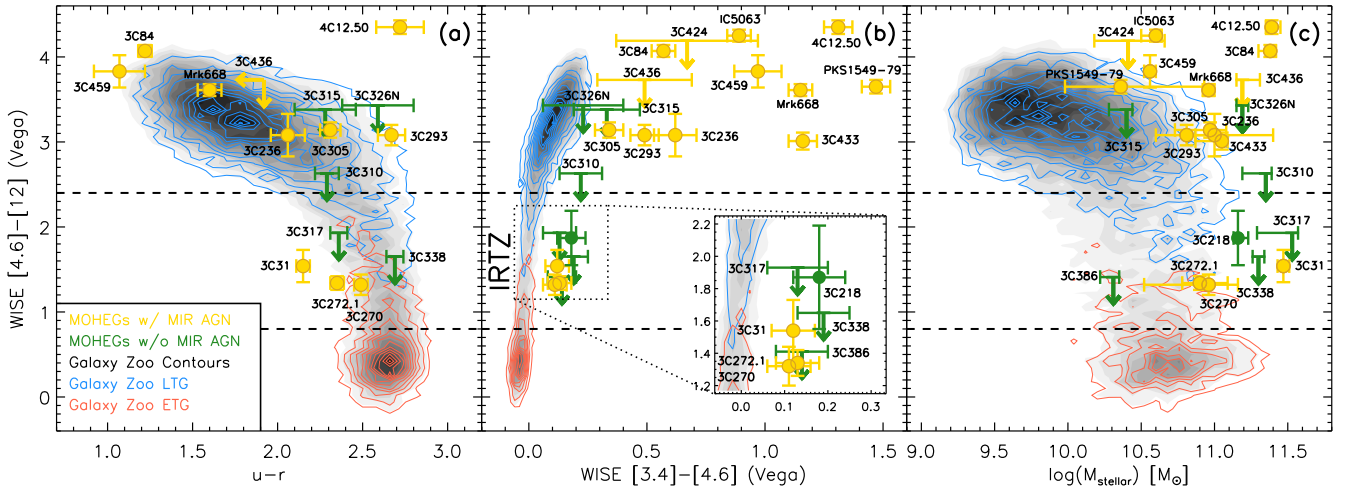


**Figure 12.** Radio MOHEGs with (yellow points) and without (green points) MIR AGNs (based on the SED fit) are compared to ERGs (red contours) and LTGs (blue contours) galaxies from the Galaxy Zoo (Lintott et al. 2008; Alatalo et al. 2014; Schawinski et al. 2014), in the *WISE* [4.6]–[12] color vs. (a)  $u-r$  color, (b) *WISE* [3.4]–[4.6] color, and (c) stellar mass. The presence of a MIR AGN tends to push galaxies to a higher [4.6]–[12] color. Our galaxies show a wide range of optical colors, likely the result of a variety of dust content. In *WISE* color-color space, radio MOHEGs have little overlap with Galaxy Zoo galaxies, instead falling into a region primarily occupied by AGNs (Stern et al. 2012). The color–mass diagram shows that our sample galaxies are typically more massive than the Galaxy Zoo galaxies.

10 of K–S (i.e. the range of normal galaxies). Its sizable warm molecular content also positions 3C 436 significantly away from the K–S relation (Fig. 8b), further supporting the presence of significant star formation suppression in this system. In contrast, 3C 310 (likewise unobserved in CO) lies almost on the K–S relation when using the dust mass to estimate the molecular reservoir; however, its warm molecular gas mass suggests it could be suppressed in star formation by over a factor of 10.

While the galaxies described above often shift in position along the horizontal axis between the different K–S plots, they still generally suggest a consistent shift toward suppressed star formation that cannot be fully explained by the peculiarities of the individual systems. The only galaxy in our sample where the apparently significant star formation suppression (by a factor of  $\sim 30$  in Fig. 8a) can be attributed to an inaccurate  $X_{\text{CO}}$  factor is 3C 293, which exhibits a very large GDR of  $\sim 1000$ . In contrast to many in this sample, its CO SLED has been well-mapped to high- $J$  CO lines, and it has a particular shape indicating a strong shock-excited component that may be driving its high CO luminosity (see Papadopoulos et al. 2008). Indeed, when we assume a normal GDR, it lies on the K–S relation. As noted in the previous section, however,

3C 293 does not show peculiarities in the other properties we have examined in this study, so the cause of its particular ISM state remains uncertain.

In Figure 9c, we compare the depletion times of the molecular reservoir ( $\tau = M_{\text{H}_2}/\text{SFR}$ ) of our reference galaxies and for our sample based on our three estimates of the molecular content. Normal galaxies have a median depletion time of  $\sim 1$  Gyr (consistent with the findings of Leroy et al. 2008) extending out to 0.1 and 10 Gyr, with only 2.4% of the sample with depletion times greater than 10 Gyr. In contrast, the median depletion times of radio MOHEGs are 2 Gyr (common GDR), 4 Gyr (common  $X_{\text{CO}}$  – cold only), and 6 Gyr (common  $X_{\text{CO}}$  – cold + warm), with 10–30% of the sample with depletion times greater than 10 Gyr. WMW and KS statistics are suggestive that the  $X_{\text{CO}}$  (cold only:  $p = 0.015$ ; 0.023),  $X_{\text{CO}}$  (cold+warm: KS  $p = 0.064$ ), and GDR ( $p = 0.0047$ ; 0.028) samples have a different distribution of depletion times from the normal galaxies.

Reassuringly, both statistics indicate that our three samples originate from the same distribution. Further, the KS statistic indicates that those galaxies with a normal GDR could come from the same distribution as those whose GDRs deviate. Since the three methods of calculating molecular mass yield

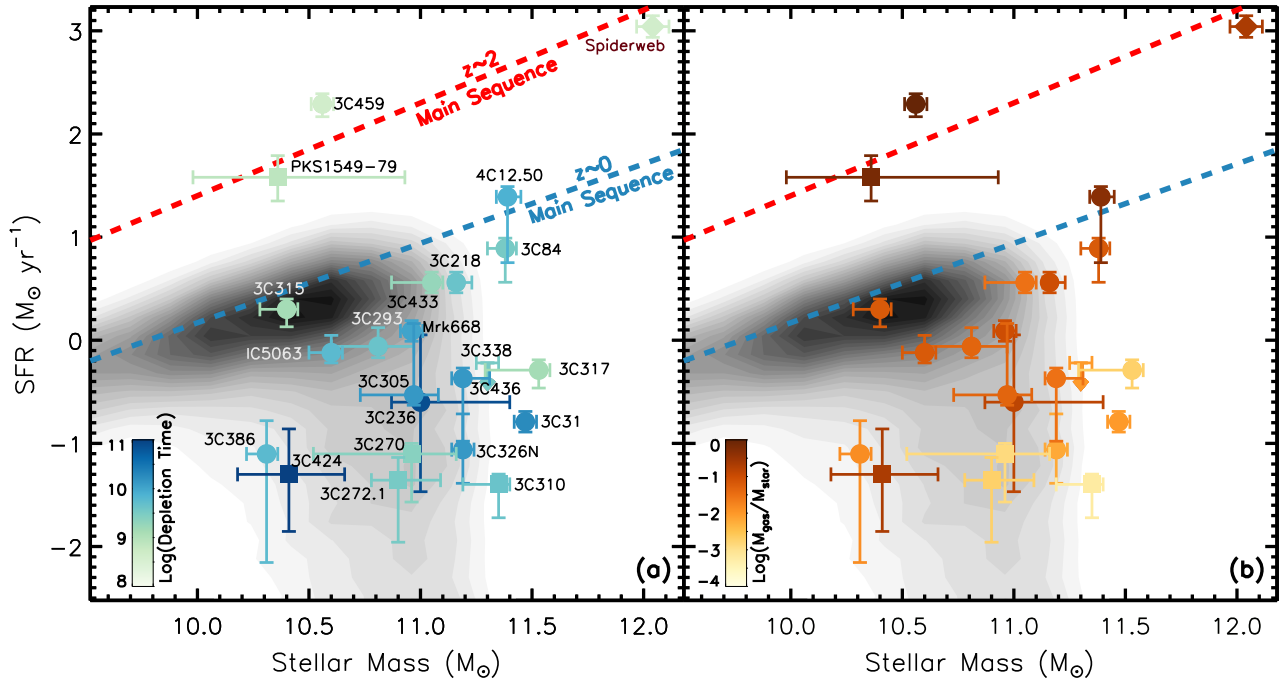


**Figure 13.** The galaxy mass–SFR relation of our galaxies compared with a large sample of SDSS galaxies (gray contours; Chang et al. 2015), whose SFRs and stellar masses were likewise determined with MAGPHYS, showing the “star formation main sequence” with a tail at the high mass and low SFR of ETGs. The blue dashed line show the main sequence at  $z \sim 0$  (Elbaz et al. 2007). Our points are colored by their common GDR depletion times (a) and gas-richness (b) with squares having more reliable SFRs. Radio MOHEGs cover a large fraction of the parameter space, although many fall in the ETG tail. Our ULIRGs are found above the main sequence. Depletion time does not clearly correlate with position relative to the main sequence, but gas-poor galaxies tend to fall further off the main sequence. For comparison, we show high redshift radio MOHEG, the Spiderweb Galaxy, along with its associated main sequence at  $z \sim 2$  (Daddi et al. 2007).

qualitatively similar and quantitatively consistent results, we will use molecular gas masses derived from dust masses for the remainder of the paper, since this method also provides the masses for all our radio galaxies.

Shi et al. (2011) suggested that stellar mass might also play a role in the regulation of the star formation efficiency and found a tight relation between star formation efficiency and stellar mass surface density that extended the K–S relation to galaxies that the K–S law had previously been unable to explain, including low surface brightness galaxies. Specifically, while the K–S relation can be re-cast as free fall in a gas-dominated gravitational potential, they argue that the stellar contribution to the gravitational potential can also be important, although they also considered that stellar mass (and its surface density) may be a proxy for more complex physics such as the impact of the kinetic and radiative energy dumped into the ISM by stars.

In Figure 10, we investigate where our sample falls on their “extended Schmidt law.” As in the K–S plots, we find that our sample tends to fall below the Shi relation, indicating that the suppression we observe in the K–S plots cannot simply be attributed to galaxy types where the K–S might fail. The offsets between our sample and the Shi galaxies are shown in Figure 11ab, where we also indicate the distribution of the ETGs over the whole Shi sample. The ETGs in the Shi sample (crosses) broadly fall on their relation, although they too tend to be a bit below the relation (with a median SFR surface density a factor of  $\sim 2$  lower than total sample) and have a suggestive statistical difference with late-type galaxies (LTGs) of the Shi sample (WMW:  $p = 0.017$ ; KS:  $p = 0.0096$ ). Our galaxies are statistically different from the whole Shi et al. sample (WMW:  $p = 0.0030$ ; KS:  $p = 0.0092$ ), but cannot be distin-

guished from the Shi ETGs.

The Shi et al. ETGs, however, tend to be primarily lenticulars, while our sample is dominated by ellipticals. The turbulence injected into the gas reservoir of radio MOHEGs is likely to further disperse their ISM from a disk into a larger volume. As a result, for these galaxies, the volume density of gas may be more important for determining the star formation efficiency in the case when the gas is not distributed in a disk. For example, some of our galaxies (e.g. 3C 84) have substantial gas contents in filamentary distributions that are poorly modeled as a disk.

Figure 11c compares the specific SFRs (sSFRs). The Shi et al. (2011) galaxies typically have sSFR of  $10^{-9.23} \text{ yr}^{-1}$ , with an even higher median for the ETGs of  $10^{-9.06} \text{ yr}^{-1}$ . In contrast, over 90% of our sample have sSFR below  $10^{-10} \text{ yr}^{-1}$  with a median sSFR of  $10^{-11.41} \text{ yr}^{-1}$ . WMW and KS statistics find very significant differences ( $p \ll 0.001$ ) between the distributions of the sSFRs of our sample compared to the Shi sample, even if we restrict our comparison to the Shi ETGs.

In short, we find statistical differences between the star formation efficiency and sSFR in our galaxies compared to normal galaxies in the several comparisons based on different estimates of the molecular reservoir. Our galaxies typically form stars less efficiently than normal galaxies with a suppression that cannot be explained by their stellar mass distribution or excitation of the CO gas resulting in a general over-estimation of the molecular gas mass.

Since we find an overall suppression in star formation, we investigated whether the degree of suppression correlates with galaxy or feedback properties. We parameterize the degree of suppression in two ways: the molecular gas depletion time

and the ratio of the expected SFR (if the molecular gas was forming stars as efficiently as predicted by the K–S relation) to the observed SFR. We do not find significant correlations between these values and gas mass, gas fraction, warm  $H_2$  luminosity, AGN luminosity, or jet power, suggesting that the relationship between feedback and the degree of suppression is complex and neither process is primarily dependent on or reflected in a single galaxy property.

#### 4.3. Radio MOHEGs in Galaxy Evolution

In Figure 12, we plot our galaxies on color–color and color–mass diagrams presented in Alatalo et al. (2014). Radio MOHEGs span a large range of optical and IR colors and are typically more massive than the underlying Galaxy Zoo distributions shown for comparison (Lintott et al. 2008; Schawinski et al. 2014). MOHEGs also tend to be dustier and more gas-rich than less active ETGs, yielding bluer optical colors and larger [4.6]–[12] colors. Our sample also has larger [3.4]–[4.6] colors compared to the Galaxy Zoo galaxies, likely driven by AGN contributions, since MOHEGs with MIR AGNs tend to have particularly larger *WISE* colors since the AGN contributes more strongly to the longer wavelength of each color.

Few of our galaxies fall into the optical “green valley” or the IR transition zone (IRTZ), typically crossed as galaxies transition from blue actively star-forming galaxies to red-and-dead systems. The five that fall into the IRTZ have minimal AGN contributions and are also the most gas-poor of our sample. We do not find correlations between any of the three colors and measures of star formation suppression.

Figure 13 compares the SFRs and stellar masses of our galaxies (colored according to their depletion times and gas-richness) to those of a large sample of SDSS galaxies whose properties were calculated from MAGPHYS (Chang et al. 2015). The contours show the star formation main sequence (Elbaz et al. 2007; Wuyts et al. 2011) with a tail toward large masses and low SFRs where red-and-dead ETGs are typically found. Radio MOHEGs are found primarily below the main sequence, but they range across more than three orders of magnitude of SFR, indicating that they exist in hosts at a variety of evolutionary stages.

Alatalo et al. (2015a) found a trend between depletion time and distance from the star formation main sequence for Hickson Compact Group (HCG) galaxies showing star formation suppression. In contrast, Radio MOHEGs are much more diverse. While those with longer depletion times lie well below the main sequence, those with the shorter depletion times are found both above and below the main sequence, suggesting that the subset with short depletion times is a mix of two populations: gas-rich galaxies with high SFRs (e.g. 3C 459, PKS 1549-79) and gas-poor galaxies with low SFRs (e.g. 3C 317, 3C 270). These two groups could also be a single population caught at different evolutionary stages. Radio MOHEGs are therefore likely to be found in galaxies with a greater variety of gas-richness than the relative homogeneity of HCGs. We find a correlation between gas-richness and distance from the star formation main sequence (Fig. 13b).

For comparison, we also shown in Figure 13 the Spiderweb galaxy (PKS1138-26; Ogle et al. 2012), a much higher redshift ( $z = 2.16$ ) MOHEG, which is a strong radio source in an unvirialized proto-cluster. It has a particularly large reservoir of warm molecular gas (eight times more massive than lower redshift radio galaxies), but with a depletion time similar to the ULIRGs 3C 459 and PKS1549-79. However, it has a

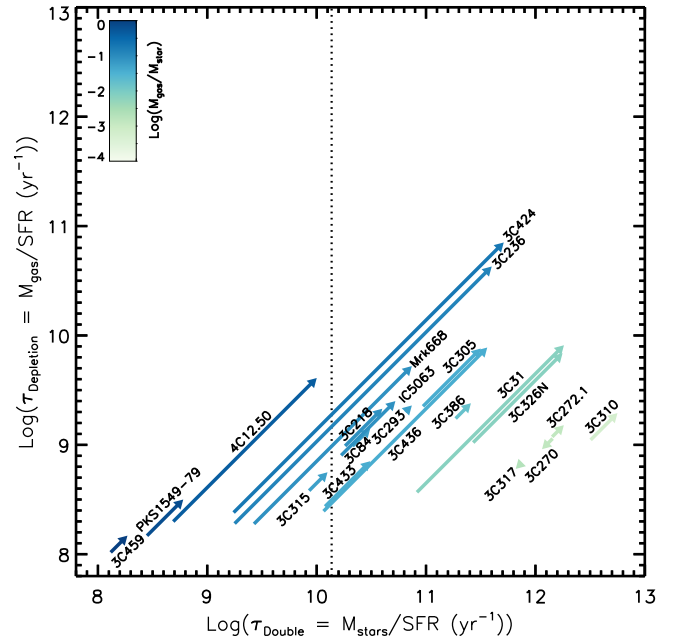


**Figure 14.** Change in the time it would take to double the stellar mass and deplete the molecular reservoir at the current SFR from the times assuming star formation at the efficiency predicted by the Kennicutt–Schmidt relation to the times based on the observed SFR (arrow head), colored by gas richness. Longer arrows are more suppressed galaxies. Gas-poor galaxies show little change and have doubling times much longer than a Hubble time (dotted line). Very gas-rich galaxies also change little, with depletion and doubling times much smaller than a Hubble time. Galaxies with intermediate gas-richness tend to show the largest increases in times and are most likely to feel significant impacts on their evolution due to suppression of star formation activity.

lower gas-richness than these ULIRGs and instead lies close to the main sequence at its redshift, making it a more massive, earlier analog to the radio galaxies just below the main sequence.

#### 4.4. When is Star Formation Suppression Important?

Given the mass of our galaxies and their low sSFRs (Fig. 11c), it is pertinent to ask whether the suppression of star formation in these systems will have a significant effect on the evolution of these galaxies. To that end, we compare the time it would take to double the stellar mass of the galaxy and deplete the molecular reservoir to the time it would take if the galaxies were forming stars at the efficiency predicted by the K–S relation based on their molecular content (Fig. 14). In calculating these timescales, we assume that the SFRs remain at the observed and calculated (based on the current molecular content) rates, although the SFRs would likely decrease as raw materials are depleted, thereby increasing both timescales.

The most gas-poor galaxies tend to have the longest doubling times because they have so little raw material out of which to form new stars and therefore the evolution of their stellar mass is little changed by a decreased SFR due to suppression. These galaxies are well on their way to being red-and-dead and are the galaxies we find in (or close to) the IRTZ and green valley (Fig. 12).

On the other side of the gas-richness spectrum, our most gas-rich galaxies have such large molecular reservoirs that injecting turbulence into their ISM still leaves a sizable portion of their molecular gas in a state where star formation can occur at (or close to) normal efficiency. Therefore, the star for-



mation suppression will have a smaller effect on the evolution of these galaxies.

About a third of our galaxies show significant suppression that has the greatest potential to affect their future stellar mass. They tend to have intermediate gas-richness and, at the SFR predicted by K–S, five of them would have doubled their stellar mass in less than a Hubble time. However, the turbulence injected into their ISM due to jet feedback has likely rendered their molecular gas infertile and thereby sizably increased the time to grow their stellar mass significantly. These galaxies would however expend their molecular reservoirs prior to doubling their stellar mass unless additional gas were to be accreted. Understanding the gas budget would require a better census of the available reservoirs of gas in the environment that could be accreted either through mergers or via gas flows. Further study of the molecular and neutral content of the inter-galactic medium as well as of the companion galaxies is needed to better understand the additional gas that may become available to these galaxies.

Outflows can also reduce star forming activity by stripping galaxies of the necessary raw materials. Many of our galaxies are known to have jet-driven outflows, in multiple gas phases including molecular (e.g., IC 5063 Morganti et al. 2015), ionized (e.g., 3C 293 Emonts et al. 2005), and neutral (see Guillard et al. 2012, for the eight galaxies from our sample with HI outflows). While these outflows can have mass fluxes as high as  $10\text{--}100 s M_{\odot} \text{ yr}^{-1}$ , only a small fraction of this mass is likely to fully escape the gravitational pull of the galaxy (e.g., Alatalo et al. 2015b), leaving the rest to potentially rain back onto the galaxy and reignite star formation or AGN activity. The relative importance of these outflows and the star formation suppression due to the injected turbulence on the evolution of galaxies is still poorly understood. A complete census of the different phases of the ISM in these galaxies and their kinematics would provide key clues with regards to loss of star-forming potential due to outflows compared to injected turbulence.

## 5. CONCLUSION

We modeled the UV–FIR SEDs of 22 radio galaxies with shocked warm molecular emission identified with *Spitzer* IRS and derived properties of the host galaxies to examine the impact of jet feedback. Figures A1–A14 show the UV–FIR images and fitted SEDs. The parameters derived from fitting these SEDs are consistent with parameters estimated via simpler relations relying on only one or a few bands. Based on the properties of these galaxies, our conclusions are as follows.

1. We find statistical evidence that star formation activity in radio MOHEGs has been suppressed by a factor of 3–6 compared to normal, star-forming galaxies, depending on whether we calculate molecular content based on dust mass or CO luminosity. Adding the warm molecular gas to our calculation of the molecular reservoir increases the suppression we measure. We do not, however, find a clear correlation between degree of star formation suppression and indicators of jet feedback, including jet power and shocked warm molecular luminosity.
2. Radio MOHEG hosts are typically massive, but in a variety of evolutionary states, covering a large range of optical and MIR colors, indicating a variety of dust content and MIR AGN contributions. These galaxies have

normal cold molecular GDRs when assuming a typical  $X_{\text{CO}}$ .

3. While this sample of radio MOHEGs primarily has early-type morphologies, it covers almost four orders of magnitude of SFR, including several LIRGs and ULIRGs. As a result, radio MOHEGs cover a large range of the SFR– $M_{\text{star}}$  space, but are primarily found in the high-mass, low-SFR tail of the star formation main sequence. Gas-rich galaxies tend to be above or near the main sequence, while gas-poor galaxies fall the farthest off of it.
4. Galaxies with an intermediate gas-richness have the greatest potential for large impacts on their future evolution through suppression of star formation by jet-driven turbulence. At least 25% of our sample will have smaller stellar masses when their star formation ends than if they had continued forming stars at the efficiency of normal star-forming galaxies. Further study is necessary to understand the impact of both gas accretion and gas loss due to outflows.

We thank Mark Lacy for his advice and useful discussion with regards to the Sajina model, as well as George Helou for suggesting the extended Schmidt law as another point of analysis, and Yong Shi, Michael Brown, and Aditya Togi, whose comments improved the revised version of this paper. This work made use of the remote access computing accounts of the NASA Herschel Science Center, which were very helpful in reducing the *Herschel* data. L.L. and P.M.O. acknowledges support for this work provided by NASA through an award issued by JPL/Caltech. Support for K.A. is provided by NASA through Hubble Fellowship grant #HST-HF2-51352.001 awarded by the Space Telescope Science Institute, which is operated by the Association of Universities for Research in Astronomy, Inc., for NASA, under contract NAS5-26555.

This work is based in part on observations made with *Herschel*, a European Space Agency Cornerstone Mission with significant participation by NASA. This publication used observations made with the *Spitzer Space Telescope*, which is operated by the Jet Propulsion Laboratory (JPL)/California Institute of Technology (Caltech) under a contract with NASA. Observations from the *Wide-field Infrared Survey Explorer*, which is a joint project of the University of California, Los Angeles, and JPL/Caltech, funded by the NASA, were also used. This publication makes use of data products from the Two Micron All Sky Survey, which is a joint project of the University of Massachusetts and the Infrared Processing and Analysis Center (IPAC)/Caltech, funded by the NASA and the NSF, as well as from the Sloan Digital Sky Survey (SDSS-III), whose funding has been provided by the Alfred P. Sloan Foundation, the Participating Institutions, the NSF, and the U.S. DOE Office of Science, and which is managed by the Astrophysical Research Consortium for the Participating Institutions of the SDSS-III Collaboration. Finally, this publication makes use of data from the *Galaxy Evolution Explorer*, retrieved from the Mikulski Archive for Space Telescopes (MAST), part of the Space Telescope Science Institute, which is operated by the Association of Universities for Research in Astronomy, Inc., under NASA contract NAS5-26555. Support for MAST for non-HST data is provided by

the NASA Office of Space Science via grant NNX09AF08G and by other grants and contracts.

This research has made use of the NASA/IPAC Extragalactic Database (NED) and the Infrared Science Archive (IRSA) which are operated by the JPL/Caltech, under contract with NASA; and NASA's Astrophysics Data System (ADS). We also used software provided by the High Energy Astrophysics Science Archive Research Center (HEASARC), which is a service of the Astrophysics Science Division at NASA/GSFC and the High Energy Astrophysics Division of the Smithsonian Astrophysical Observatory.

*Facilities:* *Herschel*, *Spitzer*, *WISE*, 2MASS, Sloan, *GALEX*

## REFERENCES

- Alam, S., Albareti, F. D., Allende Prieto, C., et al. 2015, *ApJS*, 219, 12
- Alatalo, K. 2015, *ApJ*, 801, L17
- Alatalo, K., Appleton, P. N., Lisenfeld, U., et al. 2015a, *ApJ*, 812, 117
- Alatalo, K., Blitz, L., Young, L. M., et al. 2011, *ApJ*, 735, 88
- Alatalo, K., Cales, S. L., Appleton, P. N., et al. 2014, *ApJ*, 794, L13
- Alatalo, K., Lacy, M., Lanz, L., et al. 2015b, *ApJ*, 798, 31
- Baars, J. W. M., Genzel, R., Pauliny-Toth, I. I. K., & Witzel, A. 1977, *A&A*, 61, 99
- Bell, E. F., McIntosh, D. H., Katz, N., & Weinberg, M. D. 2003, *ApJS*, 149, 289
- Bertin, E., & Arnouts, S. 1996, *A&AS*, 117, 393
- Bolatto, A. D., Wolfire, M., & Leroy, A. K. 2013, *ARA&A*, 51, 207
- Braine, J., & Dupraz, C. 1994, *A&A*, 283, 407
- Bruzual, G., & Charlot, S. 2003, *MNRAS*, 344, 1000
- Calzetti, D., Wu, S.-Y., Hong, S., et al. 2010, *ApJ*, 714, 1256
- Chang, Y.-Y., van der Wel, A., da Cunha, E., & Rix, H.-W. 2015, *ApJS*, 219, 8
- Clements, D. L., Dunne, L., & Eales, S. 2010, *MNRAS*, 403, 274
- Cohen, M., Megeath, S. T., Hammersley, P. L., Martín-Luis, F., & Stauffer, J. 2003a, *AJ*, 125, 2645
- Cohen, M., Wheaton, W. A., & Megeath, S. T. 2003b, *AJ*, 126, 1090
- Cutri, R., Skrutskie, M., Van Dyk, S., et al. 2006, Explanatory Supplement to the 2MASS All Sky Data Release and Extended Mission Products, IPAC, Pasadena, CA, <http://www.ipac.caltech.edu/2mass/releases/allsky/doc/explsup.html>
- Cutri, R., Wright, E., Conrow, T., et al. 2015, Explanatory Supplement to the WISE All-Sky Data Release Products, IPAC, Pasadena, CA, <http://wise2.ipac.caltech.edu/docs/release/allsky/expsup/>
- da Cunha, E., Charlot, S., & Elbaz, D. 2008, *MNRAS*, 388, 1595
- Daddi, E., Dickinson, M., Morrison, G., et al. 2007, *ApJ*, 670, 156
- Dale, D. A., Aniano, G., Engelbracht, C. W., et al. 2012, *ApJ*, 745, 95
- Dasyra, K. M., Combes, F., Novak, G. S., et al. 2014, *A&A*, 565, A46
- Davis, T. A., Alatalo, K., Bureau, M., et al. 2013, *MNRAS*, 429, 534
- Davis, T. A., Young, L. M., Crocker, A. F., et al. 2014, *MNRAS*, 444, 3427
- de Vaucouleurs, G., de Vaucouleurs, A., Corwin, Jr., H. G., et al. 1991, *Third Reference Catalogue of Bright Galaxies* (New York: Springer)
- Di Matteo, T., Springel, V., & Hernquist, L. 2005, *Nature*, 433, 604
- Drake, C. L., McGregor, P. J., & Dopita, M. A. 2004, *AJ*, 128, 955
- Elbaz, D., Daddi, E., Le Borgne, D., et al. 2007, *A&A*, 468, 33
- Emonts, B. H. C., Morganti, R., Tadhunter, C. N., et al. 2005, *MNRAS*, 362, 931
- Engelbracht, C. W., Blaylock, M., Su, K. Y. L., et al. 2007, *PASP*, 119, 994
- Evans, A. S., Mazzarella, J. M., Surace, J. A., et al. 2005, *ApJS*, 159, 197
- Fanaroff, B. L., & Riley, J. M. 1974, *MNRAS*, 167, 31P
- Fazio, G. G., Hora, J. L., Allen, L. E., et al. 2004, *ApJS*, 154, 10
- Feruglio, C., Maiolino, R., Piconcelli, E., et al. 2010, *A&A*, 518, L155
- Fisher, D. B., Bolatto, A., Drory, N., Combes, F., Blitz, L., & Wong, T. 2013, *ApJ*, 764, 174
- García-Burillo, S., Combes, F., Usero, A., et al. 2014, *A&A*, 567, A125
- Goddard Space Flight Center. 2004, *GALEX Observer's Guide*, GSFC, Greenbelt, MD, <http://galexgi.gsfc.nasa.gov/docs/galex/Documents/GALEXObserverGuide.pdf>
- Golombek, D., Miley, G. K., & Neugebauer, G. 1988, *AJ*, 95, 26
- González-Martín, O., & Vaughan, S. 2012, *A&A*, 544, A80
- Goulding, A. D., Alexander, D. M., Mullaney, J. R., Gelbord, J. M., Hickox, R. C., Ward, M., & Watson, M. G. 2011, *MNRAS*, 411, 1231
- Griffin, M. J., Abergel, A., Abreu, A., et al. 2010, *A&A*, 518, L3
- Guainazzi, M., Siemiginowska, A., Rodriguez-Pascual, P., & Stanghellini, C. 2004, *A&A*, 421, 461
- Guillard, P., Boulanger, F., Lehnert, M. D., et al. 2015, *A&A*, 574, A32
- Guillard, P., Boulanger, F., Pineau Des Forêts, G., & Appleton, P. N. 2009, *A&A*, 502, 515
- Guillard, P., Ogle, P. M., Emonts, B. H. C., et al. 2012, *ApJ*, 747, 95
- Hopkins, P. F., Hernquist, L., Cox, T. J., Di Matteo, T., Robertson, B., & Springel, V. 2006, *ApJS*, 163, 1
- Houck, J. R., Roellig, T. L., van Cleve, J., et al. 2004, *ApJS*, 154, 18
- Jansen, F., Lumb, D., Altieri, B., et al. 2001, *A&A*, 365, L1
- Jarrett, T. H., Chester, T., Cutri, R., Schneider, S. E., & Huchra, J. P. 2003, *AJ*, 125, 525
- Kalberla, P. M. W., Burton, W. B., Hartmann, D., et al. 2005, *A&A*, 440, 775
- Karouzos, M., Trichas, M., Im, M., Malkan, M., & the AKARI-NEP team. 2013, ArXiv e-prints
- Kellermann, K. I., Pauliny-Toth, I. I. K., & Williams, P. J. S. 1969, *ApJ*, 157, 1
- Kennicutt, Jr., R. C. 1998, *ApJ*, 498, 541
- Kühny, H., Witzel, A., Pauliny-Toth, I. I. K., & Nauber, U. 1981, *A&AS*, 45, 367
- Labiano, A., García-Burillo, S., Combes, F., et al. 2013, *A&A*, 549, A58
- . 2014, *A&A*, 564, A128
- Lacy, M., et al. 2004, *ApJS*, 154, 166
- Laing, R. A., & Peacock, J. A. 1980, *MNRAS*, 190, 903
- Laing, R. A., Riley, J. M., & Longair, M. S. 1983, *MNRAS*, 204, 151
- Lanz, L., Bliss, A., Kraft, R. P., et al. 2011, *ApJ*, 731, 52
- Lanz, L., Ogle, P. M., Evans, D., et al. 2015, *ApJ*, 801, 17
- Large, M. I., Mills, B. Y., Little, A. G., Crawford, D. F., & Sutton, J. M. 1981, *MNRAS*, 194, 693
- Leipski, C., Antonucci, R., Ogle, P., & Whysong, D. 2009, *ApJ*, 701, 891
- Leroy, A. K., Walter, F., Brinks, E., et al. 2008, *AJ*, 136, 2782
- Lintott, C. J., Schawinski, K., Slosar, A., et al. 2008, *MNRAS*, 389, 1179
- Lutz, D., Maiolino, R., Spoon, H. W. W., & Moorwood, A. F. M. 2004, *A&A*, 418, 465
- Madden, S. C., Galliano, F., Jones, A. P., & Sauvage, M. 2006, *A&A*, 446, 877
- Mahony, E. K., Morganti, R., Emonts, B. H. C., Oosterloo, T. A., & Tadhunter, C. 2013, *MNRAS*, 435, L58
- Martel, A. R., Baum, S. A., Sparks, W. B., et al. 1999, *ApJS*, 122, 81
- Martin, D. C., Fanson, J., Schiminovich, D., et al. 2005, *ApJ*, 619, L1
- Mauch, T., Murphy, T., Buttery, H. J., et al. 2003, *MNRAS*, 342, 1117
- Meléndez, M., Mushotzky, R. F., Shimizu, T. T., Barger, A. J., & Cowie, L. L. 2014, *ApJ*, 794, 152
- Mittal, R., et al. 2012, *MNRAS*, 426, 2957
- Morganti, R., Frieswijk, W., Oonk, R. J. B., Oosterloo, T., & Tadhunter, C. 2013, *A&A*, 552, L4
- Morganti, R., Oosterloo, T. A., Oonk, J. B. R., Frieswijk, W., & Tadhunter, C. N. 2015, ArXiv e-prints
- Moshir, M., Kopan, G., Conrow, T., et al. 1990, in *IRAS Faint Source Catalogue*, version 2.0 (1990)
- Mullaney, J. R., Alexander, D. M., Goulding, A. D., & Hickox, R. C. 2011, *MNRAS*, 414, 1082
- Müller, T., Okumura, K., & Klaas, U. 2011, PACS Photometer Passbands and Colour Correction Factors for Various Source SEDs, Tech. Rep. P1CC-ME-TN-038, European Space Agency
- Narayanan, D., Krumholz, M. R., Ostriker, E. C., & Hernquist, L. 2012, *MNRAS*, 421, 3127
- Nesvadba, N. P. H., Boulanger, F., Salomé, P., et al. 2010, *A&A*, 521, A65
- Nyland, K., Alatalo, K., Wrobel, J. M., et al. 2013, *ApJ*, 779, 173
- O'Brien, P. T., Reeves, J. N., & Braitto, V. 2010, in *Bulletin of the American Astronomical Society*, Vol. 42, AAS/High Energy Astrophysics Division #11, 664
- Ocaña Flaquer, B., Leon, S., Combes, F., & Lim, J. 2010, *A&A*, 518, A9
- Ogle, P., Antonucci, R., Appleton, P. N., & Whysong, D. 2007, *ApJ*, 668, 699
- Ogle, P., Boulanger, F., Guillard, P., et al. 2010, *ApJ*, 724, 1193
- Ogle, P., Davies, J. E., Appleton, P. N., et al. 2012, *ApJ*, 751, 13
- Ogle, P. M., Lanz, L., & Appleton, P. N. 2014, *ApJ*, 788, L33
- Okuda, T., Iguchi, S., & Kohno, K. 2013, *ApJ*, 768, 19
- Okuda, T., Kohno, K., Iguchi, S., & Nakanishi, K. 2005, *ApJ*, 620, 673
- Ott, S. 2010, in *Astronomical Society of the Pacific Conference Series*, Vol. 434, *Astronomical Data Analysis Software and Systems XIX*, ed. Y. Mizumoto, K.-I. Morita, & M. Ohishi, 139
- Paladini, R., Linz, H., Altieri, B., & Ali, B. 2012, Assessment analysis of the extended emission calibration for the PACS red channel, Tech. Rep. P1CC-NHSC-TR-034, NASA Herschel Science Center

- Papadopoulos, P. P., Kovacs, A., Evans, A. S., & Barthel, P. 2008, *A&A*, 491, 483
- Papadopoulos, P. P., van der Werf, P., Isaak, K., & Xilouris, E. M. 2010, *ApJ*, 715, 775
- Pearson, C., Lim, T., North, C., et al. 2014, *Experimental Astronomy*, 37, 175
- Pilbratt, G. L., Riedinger, J. R., Passvogel, T., et al. 2010, *A&A*, 518, L1
- Poglitich, A., Waelkens, C., Geis, N., et al. 2010, *A&A*, 518, L2
- Press, W. H., Flannery, B. P., & Teukolsky, S. A. 1986, *Numerical recipes. The art of scientific computing* (Cambridge: University Press, 1986)
- Punsly, B. 2005, *ApJ*, 623, L9
- Rieke, G. H., Young, E. T., Engelbracht, C. W., et al. 2004, *ApJS*, 154, 25
- Roussel, H. 2013, *PASP*, 125, 1126
- Sajina, A., Yan, L., Fadda, D., Dasyra, K., & Huynh, M. 2012, *ApJ*, 757, 13
- Salomé, P., & Combes, F. 2003, *A&A*, 412, 657
- Salomé, P., et al. 2006, *A&A*, 454, 437
- Sandstrom, K. M., Leroy, A. K., Walter, F., et al. 2013, *ApJ*, 777, 5
- Saripalli, L., & Mack, K.-H. 2007, *MNRAS*, 376, 1385
- Scharwächter, J., McGregor, P. J., Dopita, M. A., & Beck, T. L. 2013, *MNRAS*, 429, 2315
- Schawinski, K., Urry, C. M., Simmons, B. D., et al. 2014, *MNRAS*, 440, 889
- Scoville, N., Ausel, H., Sheth, K., et al. 2014, *ApJ*, 783, 84
- Shi, Y., Helou, G., Yan, L., et al. 2011, *ApJ*, 733, 87
- Silk, J., & Rees, M. J. 1998, *A&A*, 331, L1
- Skrutskie, M. F., Cutri, R. M., Stiening, R., et al. 2006, *AJ*, 131, 1163
- Smith, E. P., & Heckman, T. M. 1989, *ApJS*, 69, 365
- Smith, J. D. T., Draine, B. T., Dale, D. A., et al. 2007, *ApJ*, 656, 770
- Smith, R. K., Brickhouse, N. S., Liedahl, D. A., & Raymond, J. C. 2001, *ApJ*, 556, L91
- Smolčić, V., & Riechers, D. A. 2011, *ApJ*, 730, 64
- Spergel, D. N., Bean, R., Doré, O., et al. 2007, *ApJS*, 170, 377
- Stanghellini, C., O’Dea, C. P., Dallacasa, D., et al. 1998, *A&AS*, 131, 303
- Stern, D., Assef, R. J., Benford, D. J., et al. 2012, *ApJ*, 753, 30
- Stoughton, C., Lupton, R. H., Bernardi, M., et al. 2002, *AJ*, 123, 485
- Sutherland, R. S., & Bicknell, G. V. 2007, *ApJS*, 173, 37
- Tonry, J. L., Dressler, A., Blakeslee, J. P., et al. 2001, *ApJ*, 546, 681
- Tremblay, G. R., O’Dea, C. P., Baum, S. A., et al. 2010, *ApJ*, 715, 172
- Valtchanov, I. 2014, *The Spectral and Photometric Imaging Receiver Handbook*, European Space Agency, Madrid, Spain, [http://herschel.esac.esa.int/Docs/SPIRE/spire\\_handbook.pdf](http://herschel.esac.esa.int/Docs/SPIRE/spire_handbook.pdf)
- Varela, J., D’Onofrio, M., Marmo, C., et al. 2009, *A&A*, 497, 667
- Wagner, A. Y., & Bicknell, G. V. 2011, *ApJ*, 728, 29
- Werner, M. W., Roellig, T. L., Low, F. J., et al. 2004, *ApJS*, 154, 1
- Wright, E. L. 2006, *PASP*, 118, 1711
- Wright, E. L., Eisenhardt, P. R. M., Mainzer, A. K., et al. 2010, *AJ*, 140, 1868
- Wuyts, S., Förster Schreiber, N. M., van der Wel, A., et al. 2011, *ApJ*, 742, 96
- Wyder, T. K., Treyer, M. A., Milliard, B., et al. 2005, *ApJ*, 619, L15
- York, D. G., Adelman, J., Anderson, Jr., J. E., et al. 2000, *AJ*, 120, 1579

## APPENDIX

## A. IMAGING AND SED DETAILS

This appendix contains UV, optical or NIR, MIR, and FIR images of each of our galaxies (Figures A1–A6). We preferentially show SDSS images for the optical morphology, but use 2MASS in its absence. Similarly, we show *WISE* images only in the absence of IRAC imaging, and MIPS only in the absence of *Herschel* imaging. The optical or NIR image also contains the extraction aperture used as well as the exclusion regions placed on foreground objects or companion galaxies (see §2.2.6 for discussion on how these were determined).

Details of the observational parameters for all the images on which we measured photometry are given in Table A1, including an observation ID, the (mean) observation date, and the exposure time. For PACS observations, we note which bands were observed, while for MIPS observations we note which bands we opted to use. This is described in more detail in §2.2.5. The measured photometry, as well as the additional photometry culled from the literature or IRS enhanced products is given in Table A2.

The SEDs constructed from these photometry are shown in Figures A7–A14. For all galaxies, we tried fits both with and without an AGN component. However, we only show the AGN component if it improves the fit. For those galaxies where the fit is improved, we show both the best fit with and without an AGN component. The fitting process is described in §3, along with some caveats. We note specific concerns with regards to particular galaxies in the comments below. In addition to the fitted SEDs, we show the PDFs for six parameters from the MAGPHYS fits, again showing the results for both the best and non-AGN fits when an AGN component improves the fit.

*A1. Comments on Individual Galaxies*

**3C 31:** The top panel of Figure A1 shows that 3C 31 (NGC 383) has a close companion (NGC 382). Due to the relative proximity of 3C 31, these galaxies can be disentangled even at the resolution of SPIRE 500  $\mu\text{m}$ . Emission from its jet was previously detected by Lanz et al. (2011) at IRAC wavelengths but the contribution to the integrated SED is very small. A modest AGN contribution improves the SED fit (Figure A7), particularly in the FIR. Its IR spectrum has a normal PAH ratio but it has a silicate absorption feature that we do not model (Ogle et al. 2010).

**3C 84:** The brightest cluster galaxy (BCG) of the Perseus cluster, 3C 84 (NGC 1275) has significant filamentary structure in the UV (Figure A1). Its MIR (e.g. IRAC 8  $\mu\text{m}$ ) and FIR are dominated by the central region, although the PACS images may show some extended emission, particularly toward the northwest. Its SED (Fig. A7) shows significant MIR emission attributed to an AGN, which significantly improves the fit, as evidenced by the tighter PDFs, although we do not model the silicate emission at 10  $\mu\text{m}$  (Ogle et al. 2010). The IR luminosity of its host galaxy indicates that it is a LIRG. However, the SPIRE bands, especially at 500  $\mu\text{m}$ , show excess over the expected Rayleigh-Jeans dust emission, which is possibly due to synchrotron emission in this strong radio source. However, the SED analysis of Leipski et al. (2009) concluded that there was little synchrotron contribution to the MIR/FIR bump. It is one of three galaxies whose molecular mass is estimated from a CO(2–1) observation.

**3C 218:** 3C 218 (Hydra A) is the BCG of the Abell 780 cluster. It was not observed by SDSS, but we found *B* and *V* in the literature, and it was only observed in two IRAC bands. In addition to a small nearby companion visible in the 2MASS and IRAC images, but contributing little at UV and FIR wavelengths, there is another galaxy  $\sim 30''$  to the south–east, which is bright in the UV, MIR, and FIR. At PACS wavelengths, there exists a possible dusty bridge between these two galaxies. At the resolution of SPIRE 500  $\mu\text{m}$ , these sources begin to blend, so that photometry should be used with caution. Additionally, the

longer-wavelength SPIRE bands show possible synchrotron contamination similar to 3C 84. A MIR AGN component did little to improve the fit of this SED (Fig. A7), which is generally well fit by MAGPHYS, which is consistent with its star formation-dominated IRS spectrum (Ogle et al. 2010). Its CO observations were performed with a single dish telescope (IRAM 30m), so the extent of its molecular disk was not determined. We therefore estimate the extent of its star-forming/molecular disk for the extent of its  $8\ \mu\text{m}$  (i.e. PAH) emission.

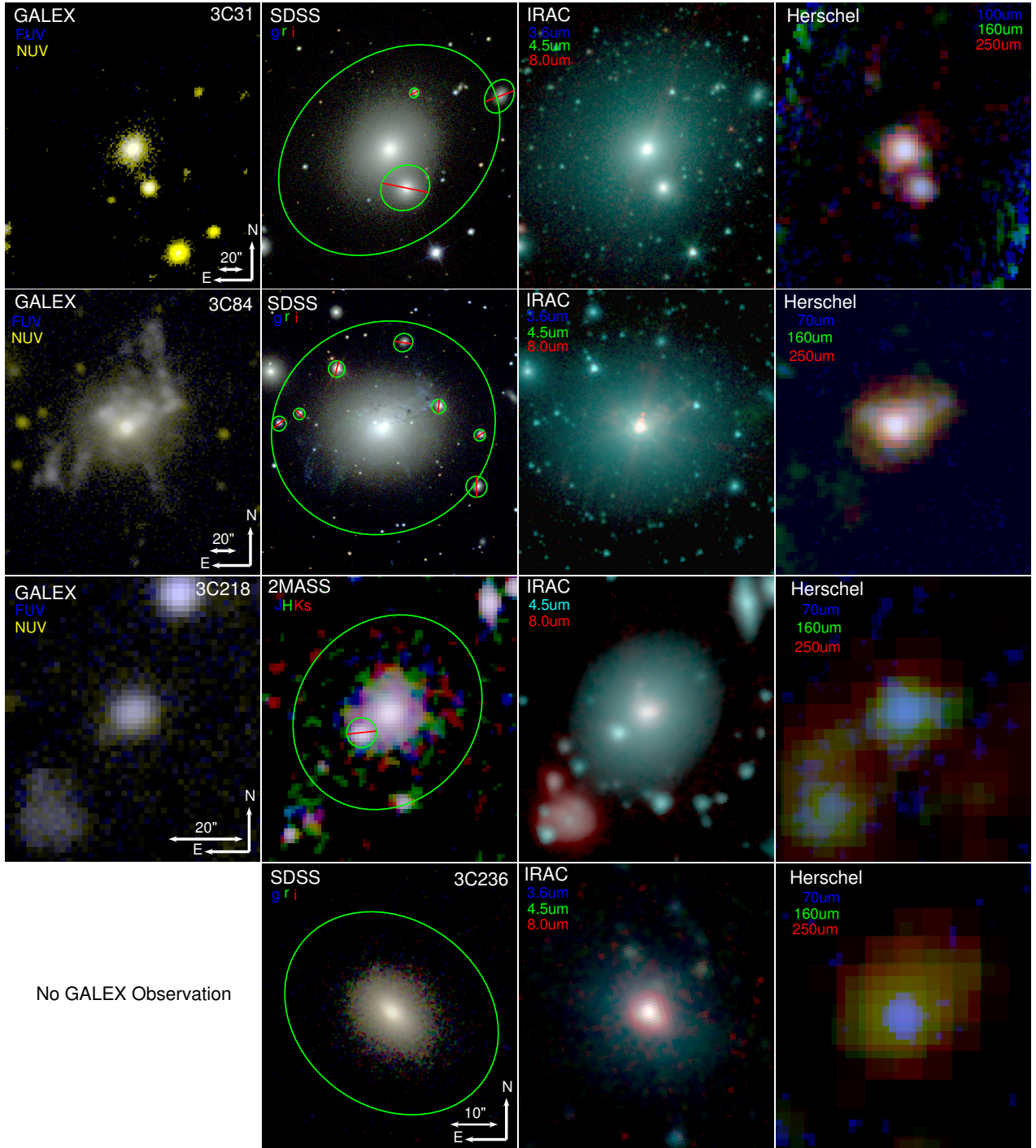


**Figure A1.** 3C 31, 3C 84, 3C 218, and 3C 236 (from top to bottom) as observed by (from left to right) (1) *GALEX* (NUV in yellow; FUV in blue), (2) SDSS ( $g$ / $r$ / $i$  in blue,  $r$ / $H$  in green, and  $i$ / $K_s$  in red), (3) IRAC or *WISE* ( $3.6\ \mu\text{m}$ / $3.4\ \mu\text{m}$  in blue,  $4.5\ \mu\text{m}$ / $4.6\ \mu\text{m}$  in green, and  $8.0\ \mu\text{m}$ / $12.0\ \mu\text{m}$  in red), and (4) *Herschel* (PACS70  $\mu\text{m}$ / $100\ \mu\text{m}$  in blue, PACS160  $\mu\text{m}$  in green, and SPIRE 250  $\mu\text{m}$  in red) or MIPS (24  $\mu\text{m}$  in blue, 70  $\mu\text{m}$  in green, and 160  $\mu\text{m}$  in red). In the optical/NIR image, the extraction aperture and exclusion regions (those with a red line through them) are shown. Section 2.2.6 describes how these were determined.

**3C 236:** No GALEX observations exist of 3C 236; however, we found UV photometry at very similar wavelengths in the literature. An isolated galaxy (Fig. A1), its SED (Fig. A8) shows a MIR excess requiring an AGN component. While this fit is an improvement overall, it is worse in the FUV and the shorter-wavelength PACS bands. There is also the possibility of synchrotron contribution at  $500\ \mu\text{m}$ .

**3C 270:** 3C 270 (NGC 4261; Fig. A2) is a member of the Virgo cluster and is one of the three galaxies in our sample not observed by *Herschel*. As a result, its FIR SED (Fig. A8) is poorly sampled and is not very well fit even with the inclusion of an AGN. We are not convinced of the necessity of an AGN component in this SED fit, so we show both possibilities. Given the poor fit in FIR, we have concerns regarding the reliability of the derived parameters and use them with caution. Due to the proximity of this galaxy, the IRS slit only covers a small portion of this galaxy, so its  $\text{H}_2$  luminosity should be considered a lower limit.

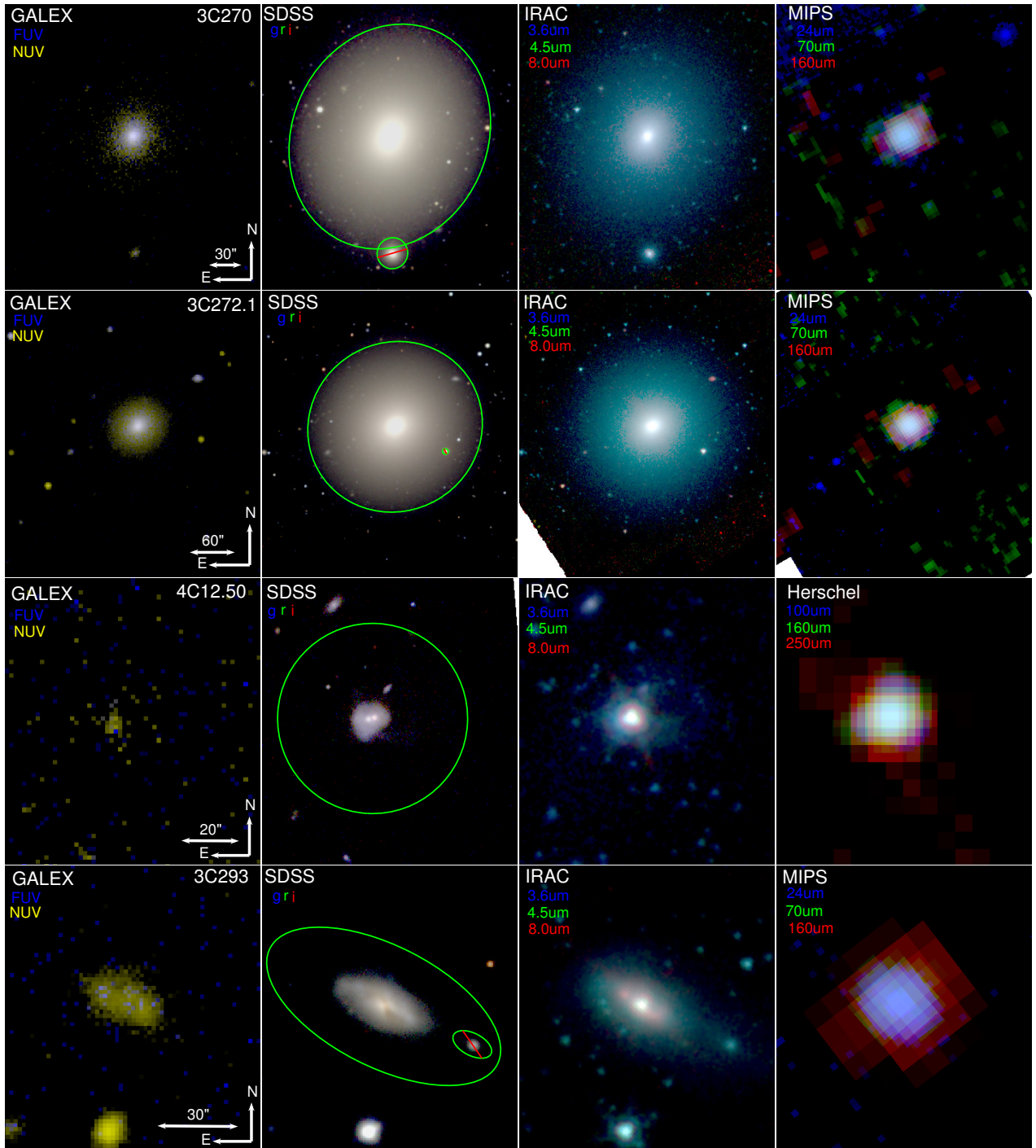


**Figure A2.** Panchromatic images of 3C 270, 3C 272.1, 4C 12.50, and 3C 293. See Fig. A1 for further details.

**3C 272.1:** 3C 272.1 (M84; Fig. A2) is also a member of the Virgo cluster, and lacks *Herschel* imaging. Like 3C270, its FIR SED, although better defined, is poorly fit and the inclusion of an AGN, while shown in Figure A8, is not very convincing. The inclusion of this component improves the fit at 60-70  $\mu\text{m}$ , but worsens it at 100  $\mu\text{m}$ , and neither the FUV nor the MIPS 24  $\mu\text{m}$  is not well modeled by either fit. Therefore, we have concerns regarding the reliability of the derived parameters and use them with caution. Its proximity means that its IRS spectrum only comes from a small fraction of the galaxy, but it shows strong 11  $\mu\text{m}$  PAH emission (Ogle et al. 2010), explaining the 12  $\mu\text{m}$  bump in the SED that we do not match well.

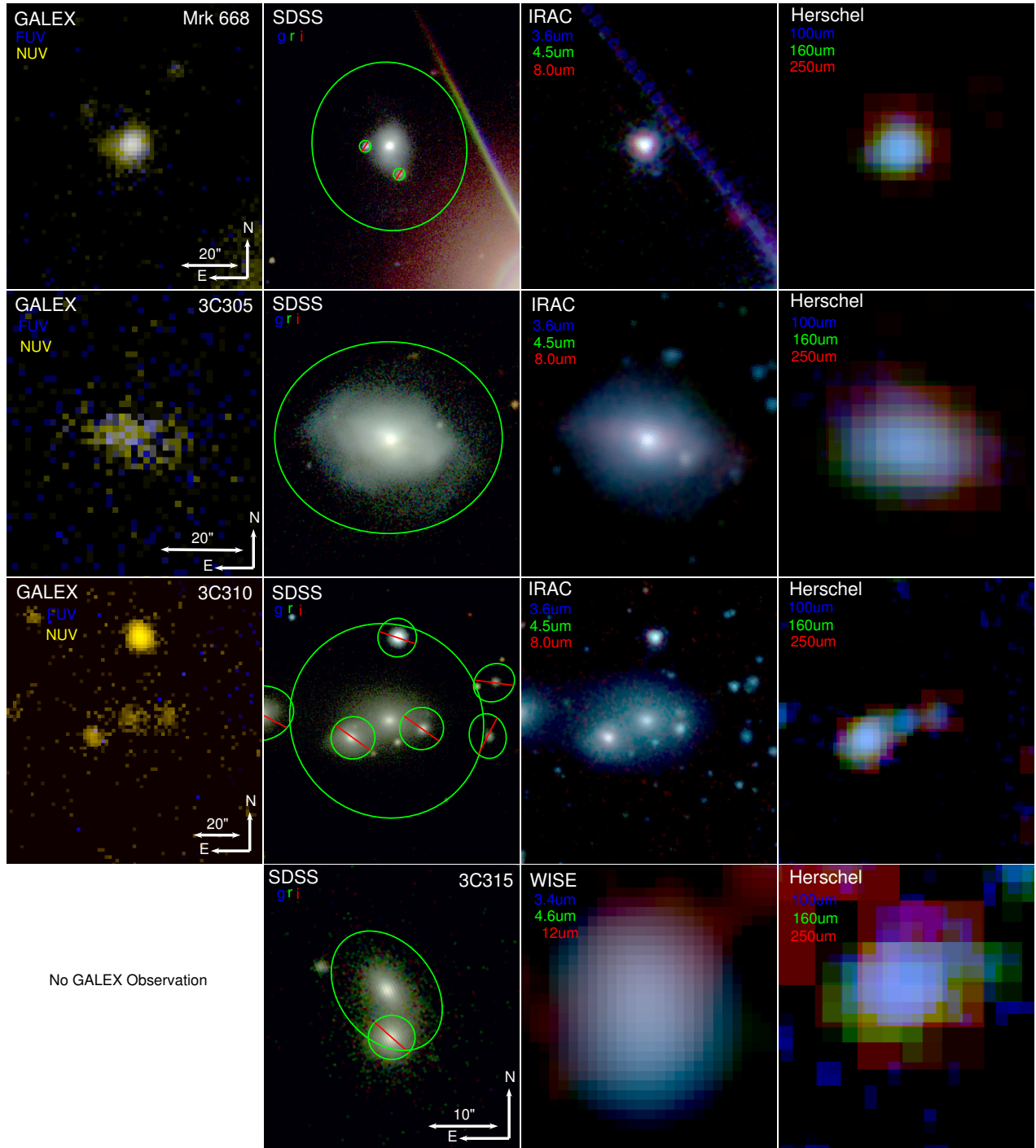


**Figure A3.** Panchromatic images of Mrk 668, 3C 305, 3C 310, and 3C 315. For 3C 310, the emission at FIR wavelengths is dominated by the eastern companion, which becomes difficult to disentangle at wavelengths longer than 100  $\mu\text{m}$ , so we could only determine upper limits for those bands. See Fig. A1 for further details.

**4C 12.50:** 4C 12.50 (PKS 1345+12) is a merging system with barely resolved centers in the SDSS images (Fig. A2). At other wavelengths, it is typically unresolved. Its SED (Fig. A9) shows a strong IR bump. Indeed, it is one of three ULIRGs in our sample. Its fit is improved with the inclusion of a MIR AGN component; however the shape of the model in the FIR suggests this galaxy might be better fit with a combination of dust temperatures not currently implemented in MAGPHYS (i.e. dust temperatures warmer than 60 K).

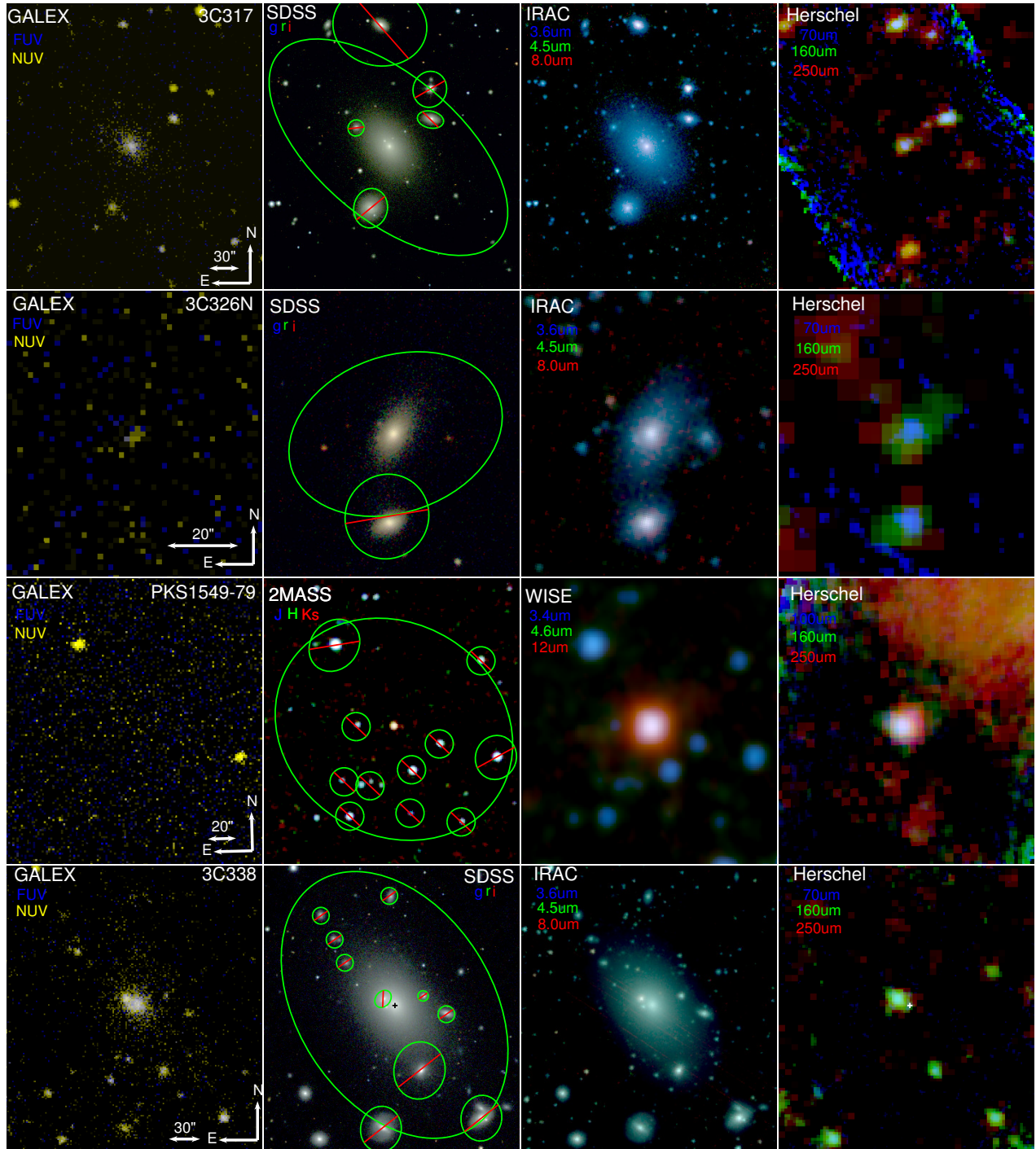


**Figure A4.** Panchromatic images of 3C 317, 3C 326N, PKS 1549-79, and 3C 338. For 3C 317, the emission at FIR wavelengths is approximately equally dominated by 3C 317 and the northwest companion; it becomes difficult to disentangle them at the longer SPIRE wavelengths. The emission in the vicinity of 3C 338 at *Herschel* wavelengths is dominated by the northeastern companion; the black cross on the SDSS image is in the same location as the white cross on the *Herschel* image. See Fig. A1 for further details.

**3C 293:** 3C 293 (UGC 8782) has a nearby companion to the southwest (Fig. A2), which we exclude in measuring the photometry. Although 3C 293 lacks *Herschel* imaging, its FIR SED (Fig. A9) is well constrained by IRAS and MIPS. Its fit is improved with a modest AGN. The inclusion of this component drives the MAGPHYS fit to slightly warmer cold dust temperatures and therefore a smaller derived dust mass than the non-AGN purely MAGPHYS fit done in Lanz et al. (2015). The derived SFR is likewise a little smaller, but agrees with the rate from Lanz et al. (2015) within the uncertainties.

**Mrk 668:** Mrk 668 (OQ 208) has a nearby, bright foreground star (Fig. A3), so care was taken to select a background region with similar levels of scattered optical light. Similarly, we added an additional exclusion region for the diffraction spike from that star in the IRAC images. Mrk 668 has a strong MIR AGN contribution (Fig. A9). Even after the removal of this component, the remaining IR emission is sufficient to classify this galaxy as a LIRG. Its IR spectrum shows emission from the  $10\ \mu\text{m}$  silicate feature (Guillard et al. 2012).

**3C 305:** 3C 305 (IC 1065; Fig. A3) has only been observed in CO with the IRAM 30m, which measured flux but not extent. To estimate the extent of the star-forming and molecular disk, we use the size of the  $8\ \mu\text{m}$  emission as a proxy for star-forming disk. Its SED (Fig. A10) is best fit including an AGN component.

**3C 310:** Figure A3 shows that 3C 310 (VV 204b) lies at the center of a cluster with several nearby galaxies. We have excluded them as shown on the SDSS image. However, due to the proximity of these companions, we are likely excluding some of the source flux and possibly retaining some contamination from the companions. At UV–MIR wavelengths, these galaxies are typically resolved and 3C 310 typically dominates the emission, so we will use the fluxes as measured. However, at FIR wavelengths, the situation becomes more complicated, because 3C 310 no longer dominates the emission and the sources become increasingly blended with increasing wavelength. Therefore, while we do obtain a detection in the PACS  $160\ \mu\text{m}$ –SPIRE  $350\ \mu\text{m}$  bands, we do not find these fluxes to be trustworthy. Therefore, for these bands, we measured the total flux in the aperture without the exclusion regions and treat them as upper limits. As a result, the FIR SED (Fig. A10) of 3C 310 is poorly constrained and we use its derived parameters with caution.

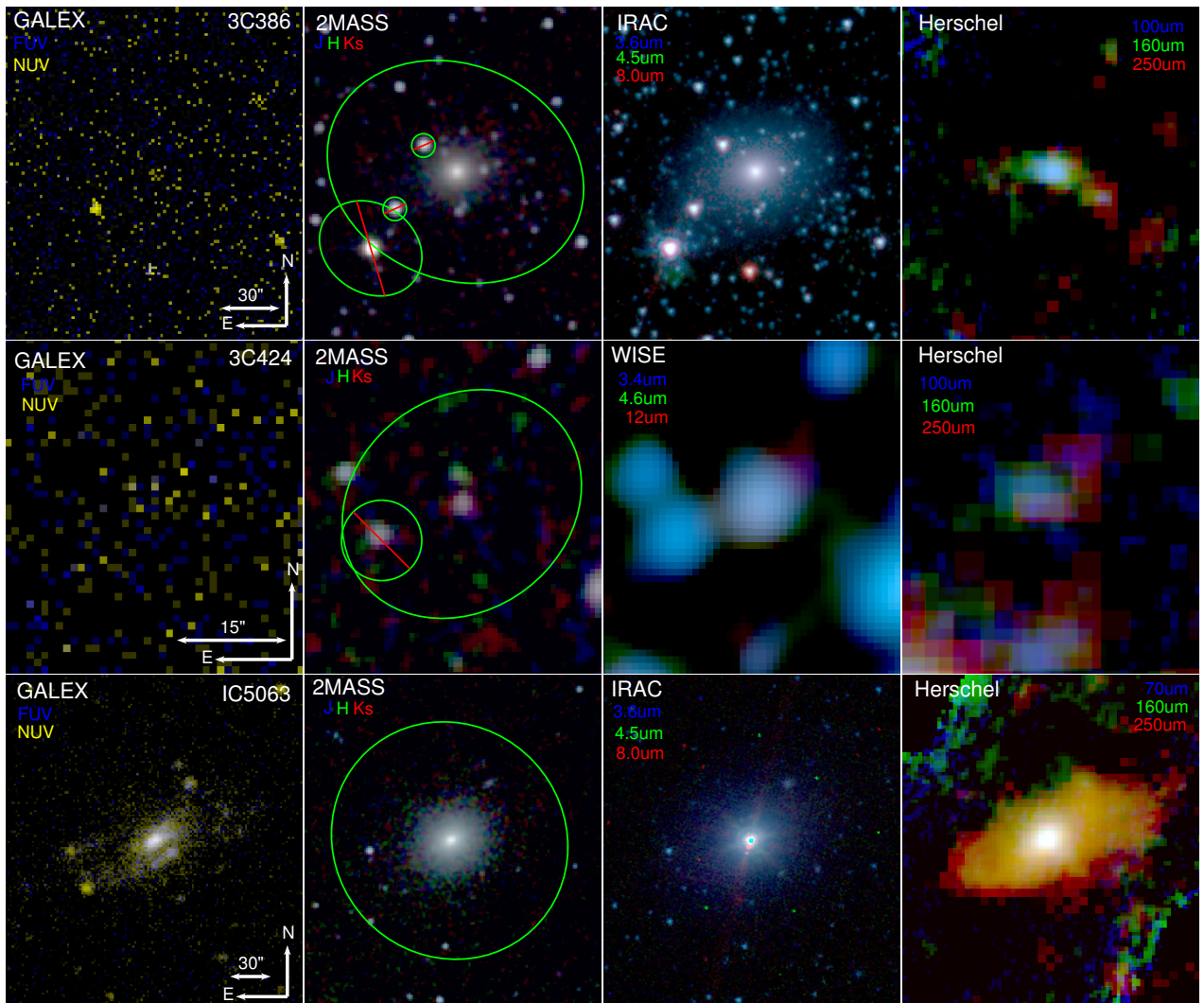


**Figure A5.** Panchromatic images of 3C 386, 3C 424, and IC 5063. IC 5063 is saturated at  $8\ \mu\text{m}$ . See Fig. A1 for further details.



**3C 315:** 3C 315 was not observed with GALEX and has a nearby companion resolved by SDSS (Fig. A3). At IR wavelengths, it only has *WISE* and *Herschel* imaging, so resolving the galaxies becomes very difficult. However, the  $12\ \mu\text{m}$  *WISE* image and the *Herschel* images strongly suggest that the MIR–FIR emission of this system is dominated by our host galaxy instead of its companion. Its SED (Fig. A10) does not require an AGN component, which is consistent with its IRS spectrum that show strong PAH emission from star forming activity (Ogle et al. 2010).

**3C 317:** 3C 317 (UGC 9799) is the BCG of Abell 2052, and as such has a number of close companions (Fig. A4). At FIR wavelengths, the emission of one of its smaller companions (to the north–west) becomes pronounced, so we took care to ensure that the exclusion region was sufficiently large to also include the *Herschel* emission. Its SED (Fig. A11) fit does not improve with the inclusion of an AGN component.

**3C 326N:** 3C 326N has a companion, which is resolved at all *Herschel* wavelengths (Fig. A4). At PACS wavelengths, there is a hint of extended emission along the major axis of this galaxy. Its SED (Fig. A11) does not require an AGN to fit. Its *Spitzer* observations were discussed in detail by Ogle et al. (2007) who measured SFR from the  $7.7\ \mu\text{m}$  PAH feature consistent with our SED-derived SFR.

**PKS 1549-79:** PKS 1549-79 is a ULIRG, whose SED (Fig. A11) is dominated by its IR emission. Its images (Fig. A4) likewise show that it is much dimmer at UV–NIR wavelengths than in the MIR–FIR. Due to its declination, it is too far south to fall in the SDSS footprint and as a result, its UV–optical SED is poorly defined. Therefore, we treat its stellar mass with great caution (the PDF of  $M_*$  is also quite broad). PKS 1549-79 has a quite strong MIR AGN component. In the *Herschel* bands, significant diffuse foreground emission can be seen in the top-right corner of the image, requiring the use of a point source aperture at those wavelengths to minimize contamination.

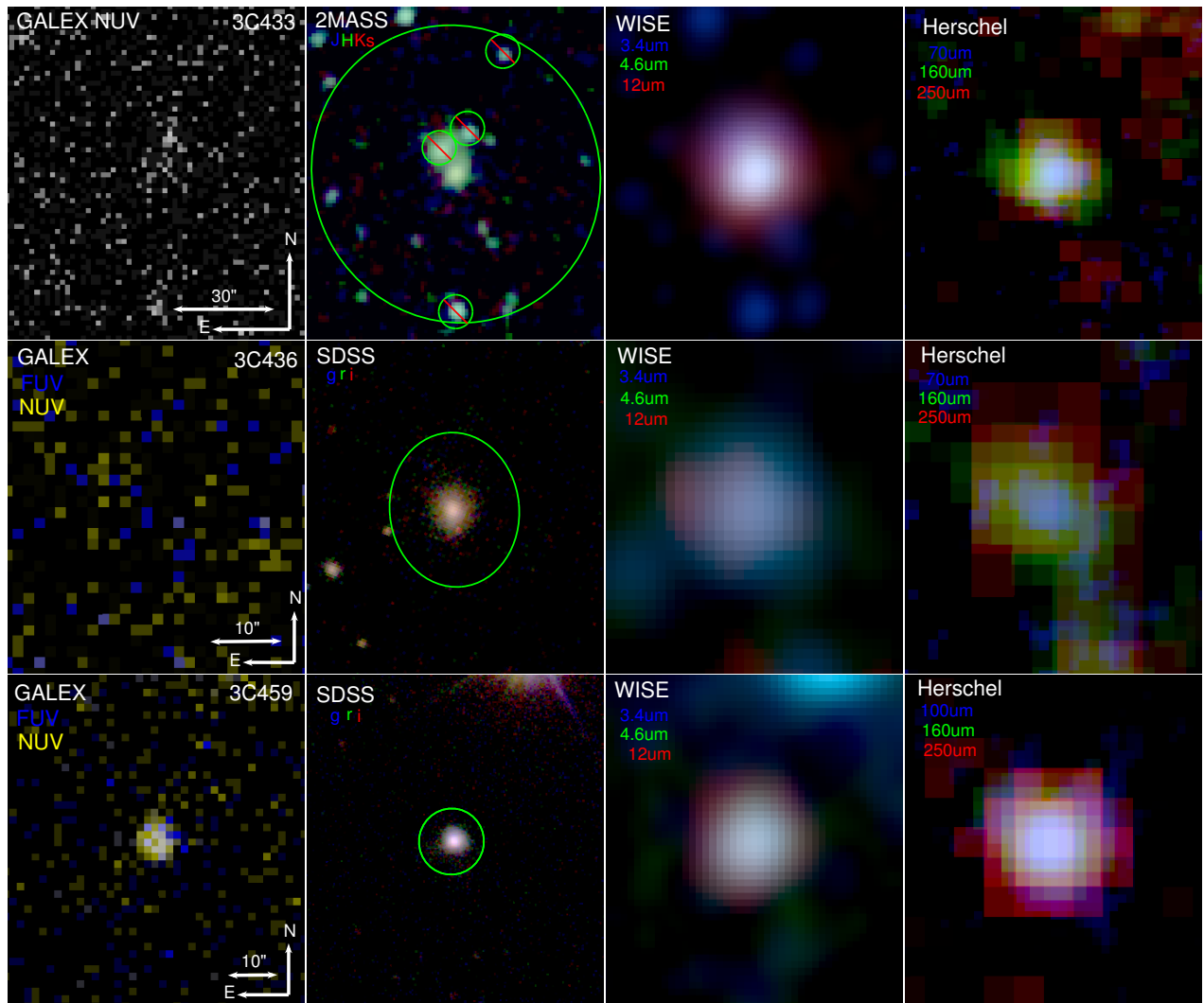


**Figure A6.** Panchromatic images of 3C 433, 3C 436, and 3C 459. 3C 433 was only observed in the NUV band with *GALEX*. See Fig. A1 for further details.

**3C 338:** 3C 338 (NGC 6166) is the BCG of Abell 2052 (Fig. A4). As a result, it has numerous small companions, but still dominates the emission into the MIR. In the *Herschel* bands, however, the emission is dominated by the small galaxy just north-east of the center of 3C 338, as can be seen by the location of the emission in that panel compared to the white cross which is in the same position as the black cross in the SDSS image. Given the proximity of that galaxy and the resolution of the *Herschel* instruments, we cannot disentangle any minor contribution from 3C 338. Therefore, we only have upper limits, measured including the companions, on *Herschel* photometry. As a result, our FIR SED (Fig. A12) is completely undefined, and we treat the derived dust luminosity, dust mass, and SFR as upper limits. The little MIR information that we have does not

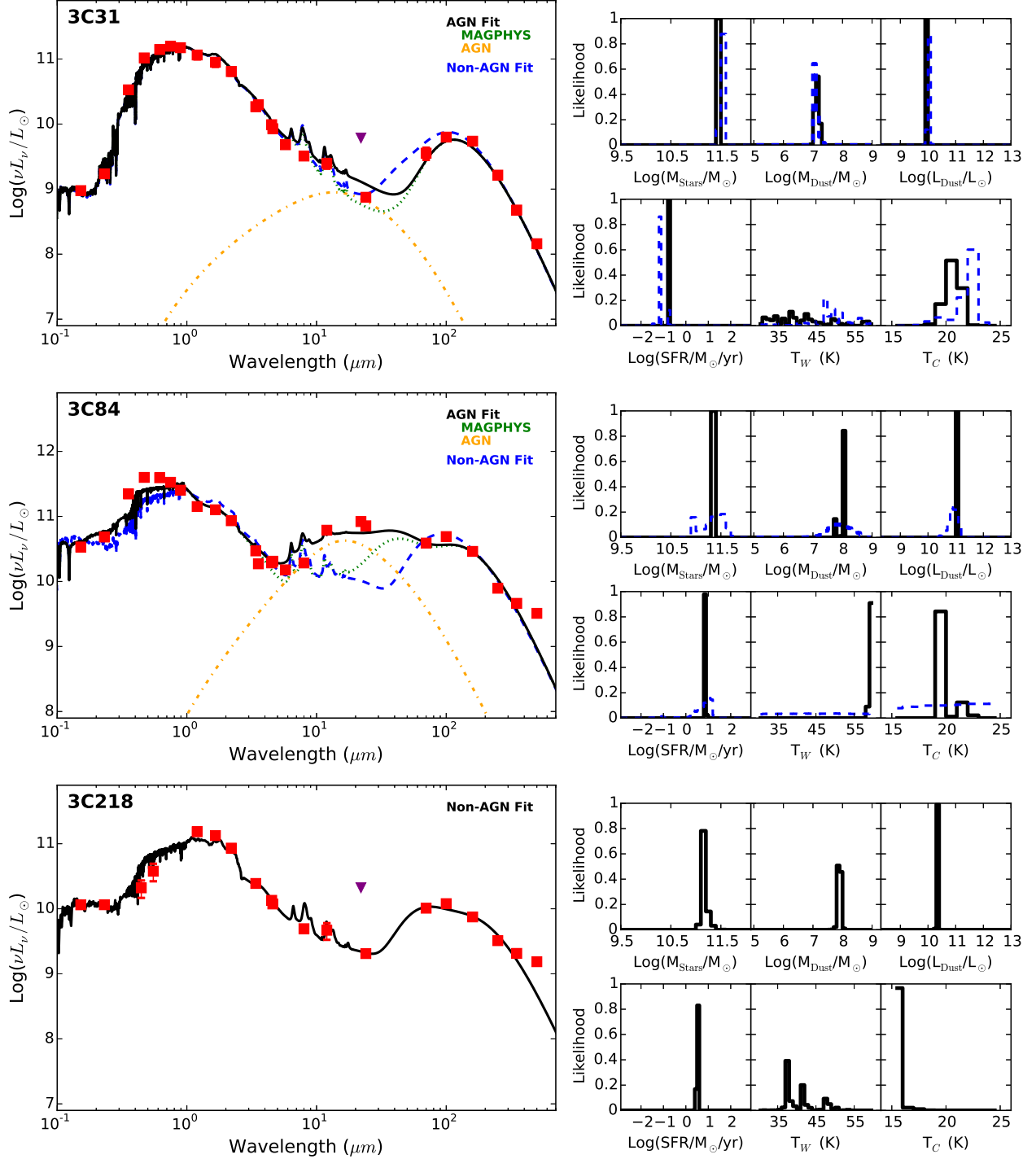


**Figure A7.** SEDs for 3C 31 (top), 3C 84 (middle), and 3C 218 (bottom) with photometry shown as red squares (purple triangles are upper limits) and the best fit model plotted in black. When an AGN component is necessary to improve the fit in the MIR, we also show the AGN component (orange dash-dot line) and the host component (green dotted line), as well as the best fit without an AGN (blue dashed line). To the right of the SED, we plot a subset of the PDFs of the fitted parameters for (from left to right): stellar mass, dust mass, and dust luminosity (top) and SFR, warm dust temperature, and cold dust temperature (bottom). When an AGN is needed, we show the PDFs both for the best fit (black) and for the fit without an AGN (blue dashed).

support the inclusion of an AGN component.

**3C 386:** Figure A5 shows that 3C 386 has indications of extended emission in the FIR, but it is not associated with its fat double radio structure. Its CO observation does not have a measured extent. We therefore estimate the size of the molecular/star-forming region based on the extent of the  $8\ \mu\text{m}$  emission, which, as can be seen in the IRAC panel of Figure A5 is centrally condensed compared to the stellar extent observed in the shorter IRAC bands. Its SED (Fig. A12) is sparsely sampled in the UV and optical. It is not very well fit at  $5.6$  and  $8\ \mu\text{m}$ , which may be due to a difference between the PAH lines in the MAGPHYS template and the reality in this system, in which both the  $7.7$  and  $11.3\ \mu\text{m}$  PAH are weak (Ogle et al. 2010).

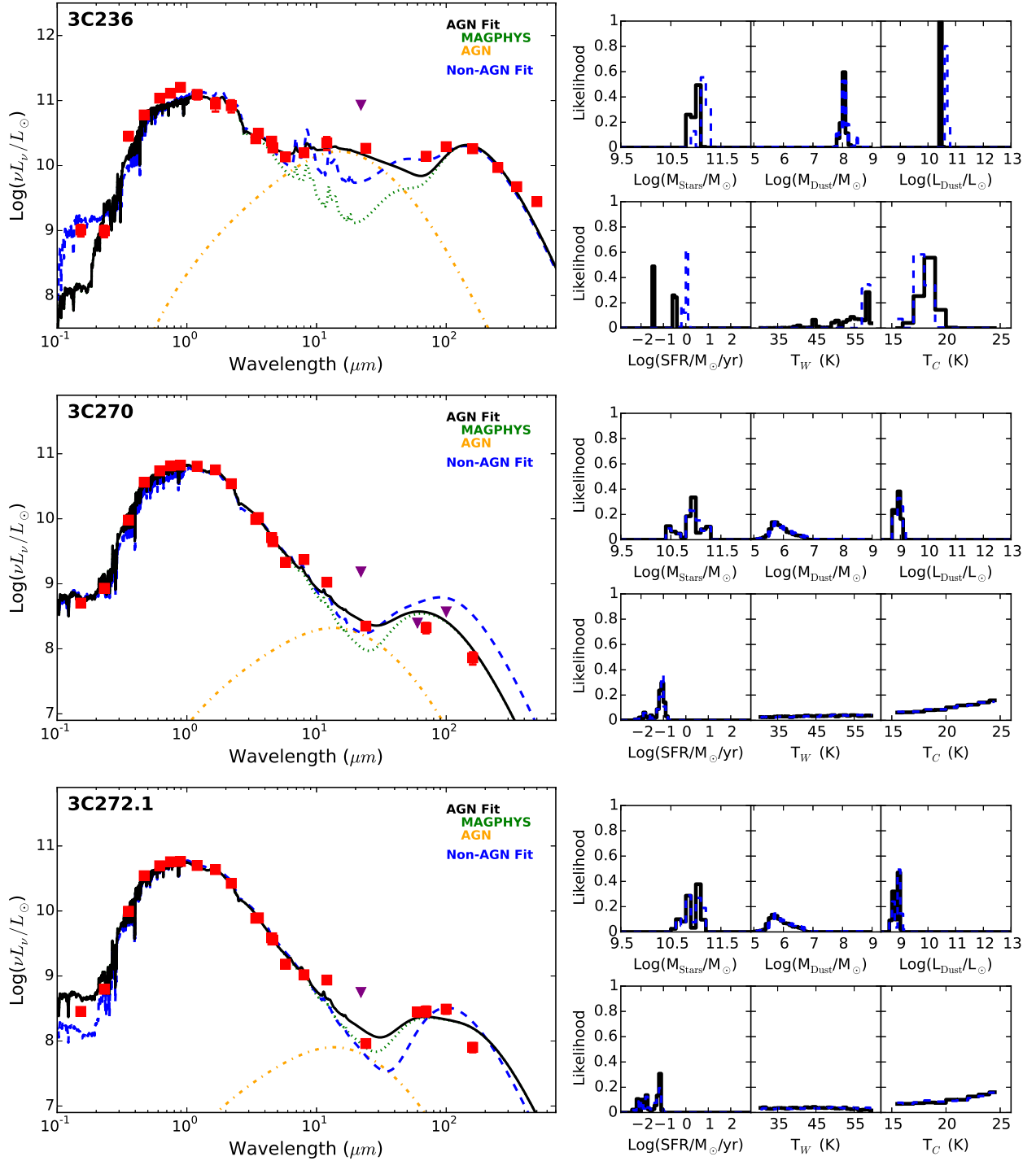


**Figure A8.** SEDs for 3C 236 (top), 3C 270 (middle), and 3C 272.1 (bottom) with photometry shown as red squares (or purple triangles for upper limits) and the best fit model plotted in black. Further details are given in Fig. A7 captions.

**3C 424:** 3C 424, as can be seen in both its images (Fig. A5) and its SED (Fig. A12) is poorly detected in only a few bands. Indeed of the six photometric points used in the fit, three come from the literature (or enhanced archive product). This is also visible in the large widths of its parameter PDFs, so the derived parameters have large uncertainties and should be treated with caution. The relative fluxes at 8 and 24  $\mu\text{m}$  are better fit with the inclusion of an AGN component. Leipski et al. (2009) concluded that star formation contributed little to IR spectrum, which Ogle et al. (2010) found to be flat. Indeed, the IR spectrum could be a continuation of the synchrotron emission from the radio into the IR.

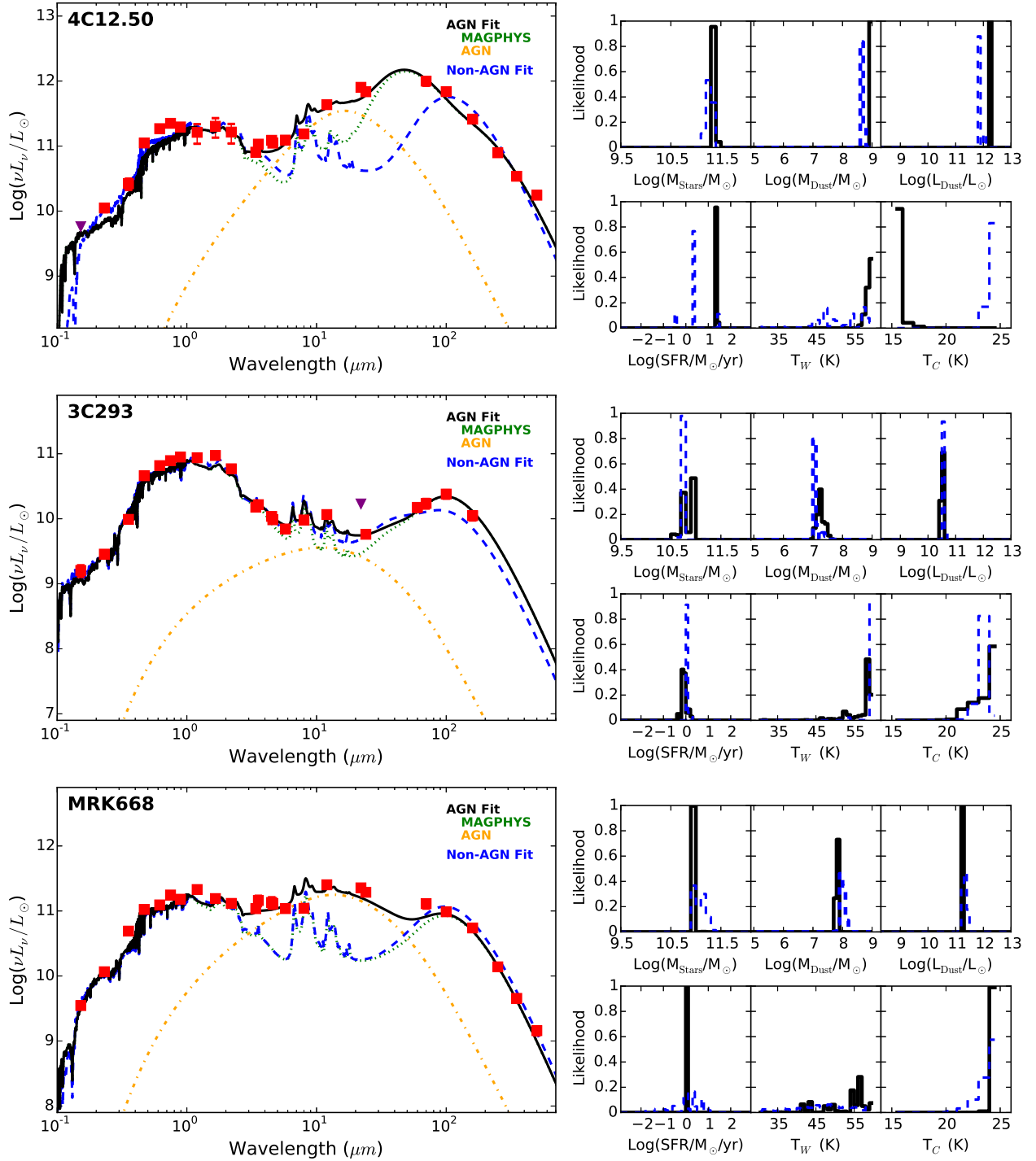


**Figure A9.** SEDs for 4C 12.50 (top), 3C 293 (middle), and Mrk 668 (bottom) with photometry shown as red squares (or purple triangles for upper limits) and the best fit model plotted in black. Further details are given in Fig. A7 captions.

**IC 5063:** IC 5063 is one of our closest galaxies and shows significant filamentary structure in the UV that may be tracing out a star-forming disk (Fig. A5). The extended *Herschel* emission likewise suggests the presence of a dusty disk. Unfortunately, its IRAC  $8\ \mu\text{m}$  image is saturated. Since its CO observations have not provided a measure of the extent of its molecular content, we estimate that size from the extent of the central region of strong UV emission. The SED of IC 5063 (Fig. A13) requires a sizable MIR AGN contribution.

**3C 433:** 3C 433 was only observed by *GALEX* in the NUV (Fig. A6), but was not detected, so we only have limits on the UV emission. It has two nearby companions, resolvable only in our 2MASS images. However, both the *WISE* and *Herschel* emissions appear to be centered on the desired 2MASS source, therefore we assume that this galaxy dominates the IR emission. Its SED (Fig. A13) is better fit with a significant AGN component. Its IRS spectrum has strong silicate absorption and weak PAH

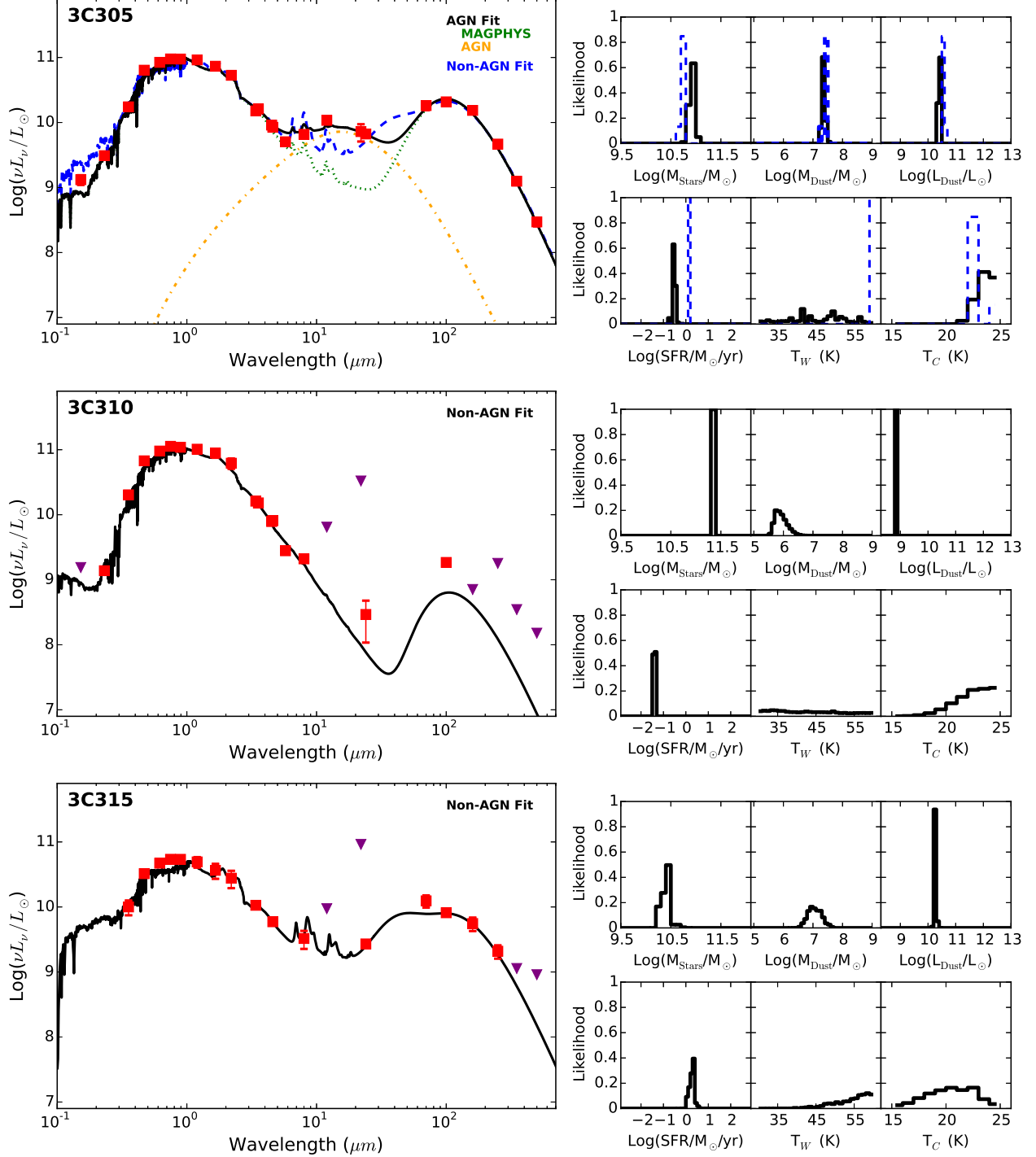


**Figure A10.** SEDs for 3C 305 (top), 3C 310 (middle), and 3C 315 (bottom) with photometry shown as red squares (or purple triangles for upper limits) and the best fit model plotted in black. Further details are given in Fig. A7 captions.

emission, contrary to the SED fit (Ogle et al. 2010).

**3C 436:** Due to its distance, we only marginally resolve 3C 436 in SDSS, where it appears to be a non-interacting ETG (Fig. A6). Its MIR emission is poorly sampled, primarily with IRS-derived 8 and 24  $\mu\text{m}$  photometric points, which suggest the need for an AGN component in the SED fit (Fig. A14).

**3C 459:** 3C 459 is our most distant source, and appears as a point source in all bands (Fig. A6). Its SED (Fig. A14) is dominated by its IR emission, and indeed, it meets ULIRG criteria. The inclusion of a MIR AGN component improves the fit.

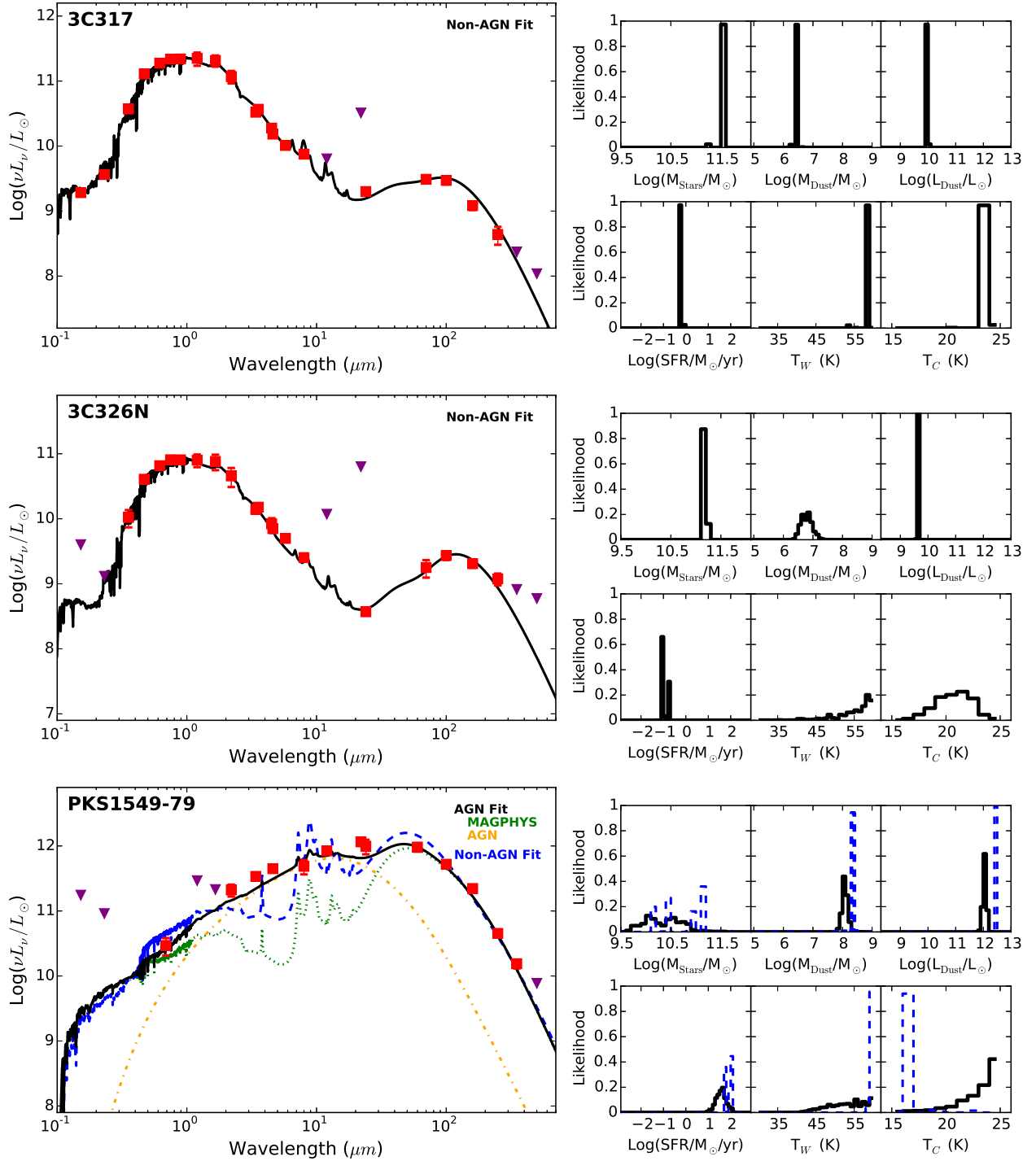


**Figure A11.** SEDs for 3C 317 (top), 3C 326N (middle), and PKS 1549-79 (bottom) with photometry shown as red squares (or purple triangles for upper limits) and the best fit model plotted in black. Further details are given in Fig. A7 captions.

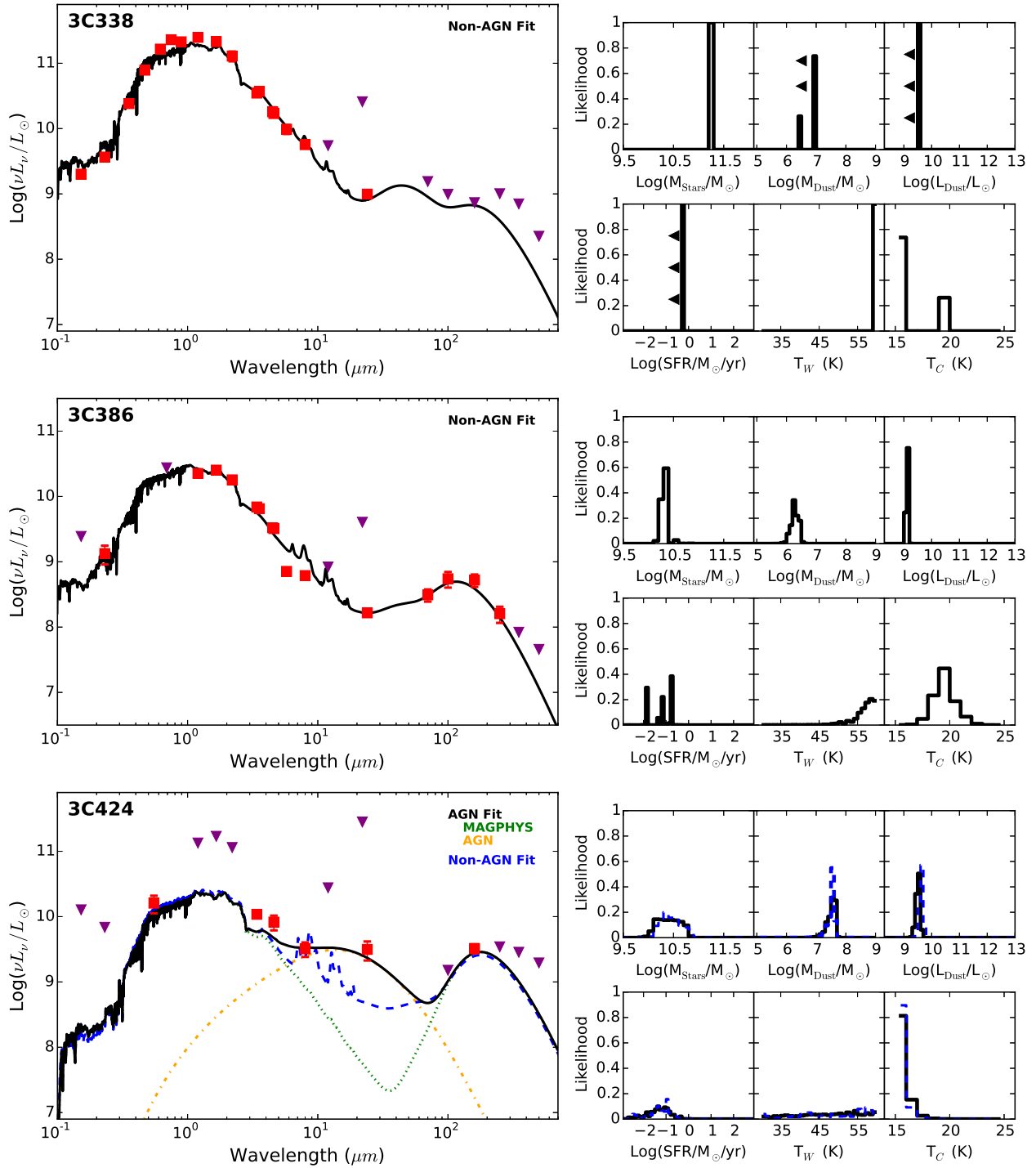


**Figure A12.** SEDs for 3C 338 (top), 3C 386 (middle), and 3C 424 (bottom) with photometry shown as red squares (or purple triangles for upper limits) and the best fit model plotted in black. Further details are given in Fig. A7 captions.

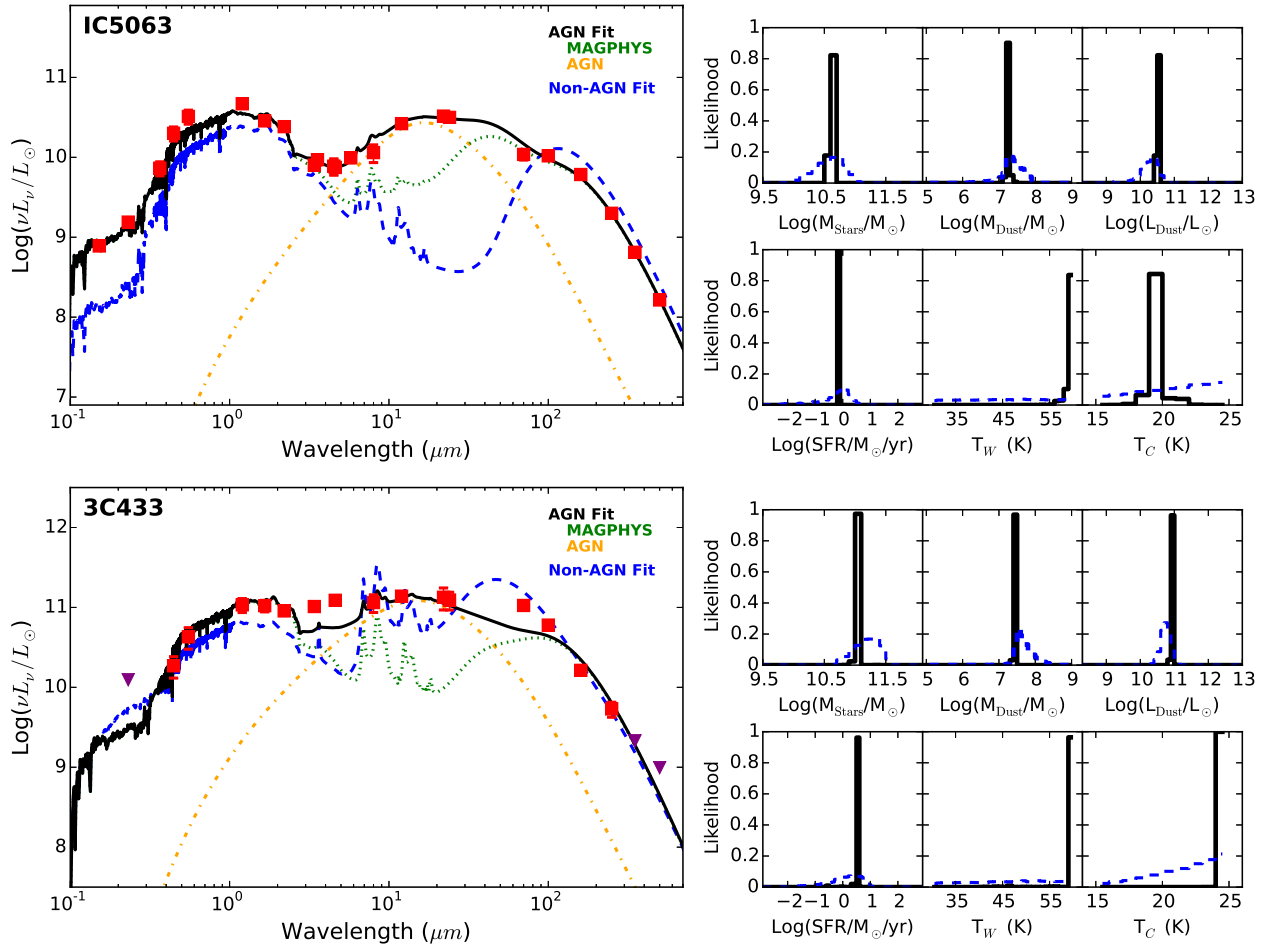


**Figure A13.** SEDs for IC 5063 (top) and 3C 433 (bottom) with photometry shown as red squares (or purple triangles for upper limits) and the best fit model plotted in black. Further details are given in Fig. A7 captions.



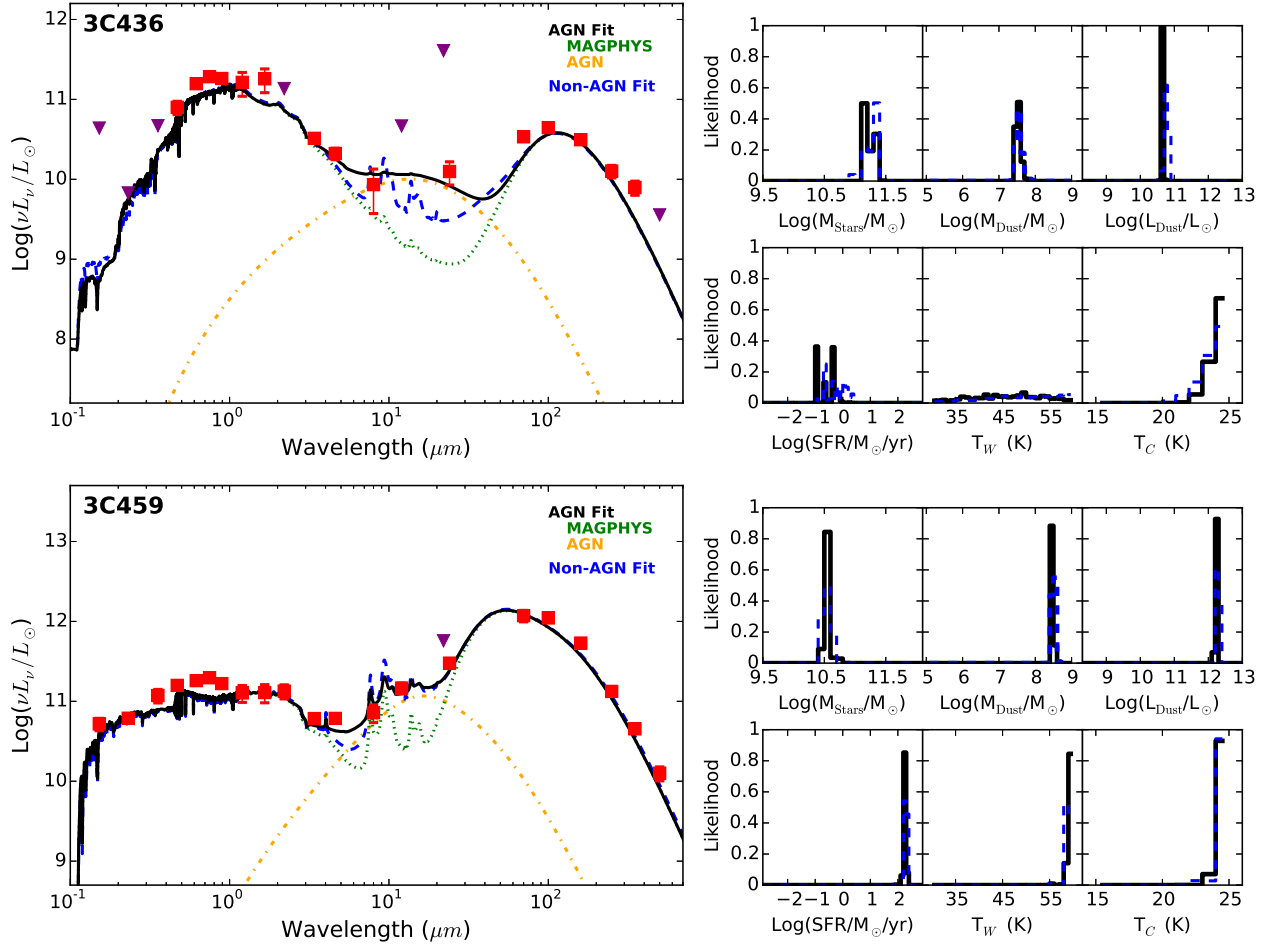


**Figure A14.** SEDs for 3C 436 (top) and 3C 459 (bottom) with photometry shown as red squares (or purple triangles for upper limits) the best fit model plotted in black. Further details are given in Fig. A7 captions.

**Table A1**  
Observation Description

Name	Wavelength Region	Telescope/ Instrument	Obs. ID <sup>a</sup>	Date	Exposure (s; frames) <sup>b</sup>	Notes
3C 31	UV	GALEX/(FUV;NUV)	GI2_019002_3C 31	2005-11-05	4734.2; 4970.2	
	Optical	SDSS	008111-5-0175	2009-10-17	53.9	Drift Mode
	NIR	2MASS	981019n1010115	1998-10-19	273	
	MIR	Spitzer/IRAC	3418/10918400	2005-01-16	24x30s	
	MIR	WISE	0176p318_ab41	2010-07-20	261 <sup>1,2</sup> /253 <sup>3,4</sup>	
	MIR/FIR	Spitzer/MIPS	82/4691968	2004-12-26	28x2.6s; 28x10.5s	24, 70
	FIR	Herschel/PACS	1342224218-19	2011-07-15	445 s × 2 <sup>2</sup>	100, 160
	FIR	Herschel/SPIRE	1342236245	2012-01-03	307	
3C 84	UV	GALEX/(FUV;NUV)	GI1_098001_A0426	2004-10-07	14990.2; 16249.3	
	Optical	SDSS	003629-1-0067	2003-01-28	53.9	Drift Mode
	NIR	2MASS	LGA(ngc1275)	... <sup>c</sup>	...	
	MIR	Spitzer/IRAC	3228/10483456	2005-02-20	40x30s	
	MIR	WISE	0494p408_ab41	2010-02-11	132	
	MIR/FIR	Spitzer/MIPS	3351/11153920	2005-02-25	42x2.6s	24
	FIR	Herschel/PACS <sup>d</sup>	1342216022-23	2011-03-14	153 s × 2 <sup>1</sup>	70, 160
	FIR	Herschel/PACS <sup>d</sup>	1342204217-18	2010-09-09	153 s × 2 <sup>2</sup>	100, 160
3C 218	UV	GALEX/(FUV;NUV)	GI3_103007_HydraA	2008-01-10	2233.1	
	NIR	2MASS	990515s0180009	1999-05-15	274	
	MIR	Spitzer/IRAC	50795/26923008	2008-06-09	36x100s	
	MIR	WISE	1390m122_ab41	2010-05-11	138 <sup>1,2</sup> /130 <sup>3,4</sup>	
	MIR/FIR	Spitzer/MIPS	82 /4707584	2004-05-04	14x10s	24
	FIR	Herschel/PACS	1342207071-74	2010-10-25	571 s × 4 <sup>3</sup>	70, 100, 160
	FIR	Herschel/SPIRE	1342207041	2010-10-24	721	
	3C 236	Optical	SDSS	004469-3-0269	2004-02-17	53.9
NIR		2MASS	981212n1610056	1998-12-12	273	
MIR		Spitzer/IRAC	3418/10921216	2004-12-16	24x30s	
MIR		WISE	1516p348_ab41	2010-05-06	142	
MIR/FIR		Spitzer/MIPS	82 /4708096	2004-04-12	14x10s	24
FIR		Herschel/PACS <sup>d</sup>	1342270912-13	2013-04-26	266 s × 2 <sup>3</sup>	70, 100, 160
FIR		Herschel/PACS <sup>d</sup>	1342246697-98	2012-06-07	895 s × 2 <sup>2</sup>	100, 160
FIR		Herschel/SPIRE	1342246613	2012-06-03	997	
3C 270	UV	GALEX/(FUV;NUV)	GI3_079021_NGC4261	2008-03-04	1655.0	
	Optical	SDSS	002126-5-0438	2001-02-20	53.9	Drift Mode
	NIR	2MASS	LGA(uge5360)	... <sup>c</sup>	...	
	MIR	Spitzer/IRAC	69/4461056	2004-05-27	10x12s	
	MIR	WISE	1853p060_ab41	2010-06-17	209 <sup>1</sup> /127 <sup>2</sup> /112 <sup>3</sup> /120 <sup>4</sup>	
	MIR/FIR	Spitzer/MIPS	82/4692736	2005-06-22	28x10s; 128x10.5s; 68x10.5s	24, 70, 160
	3C 272.1	UV	GALEX/FUV	GI5_057013_NGC4388	2009-05-07	2538.0
UV		GALEX/NUV	Virgo_Epoque_MOS01	2006-03-20	15699.9	
Optical		SDSS	003836-4-0249	2003-03-31	53.9	Drift Mode
NIR		2MASS	LGA(m84)	... <sup>c</sup>	...	
MIR		Spitzer/IRAC	69/4463872	2004-05-27	10x12s	
MIR		WISE	862p136_ab41	2010-06-15	144	
MIR/FIR		Spitzer/MIPS	82/4692992	2004-06-01	28x2.6s; 16x10.5s; 68x10.5s	24, 70, 160
4C 12.50	UV	GALEX/FUV	AIS_220	2007-05-08	132.1	
	UV	GALEX/NUV	AIS_220	2005-05-07	224.1	
	Optical	SDSS	003836-5-0384	2003-03-31	53.9	Drift Mode
	NIR	2MASS	980502n0390256	1998-05-02	273	
	MIR	Spitzer/IRAC	32/3893760	2004-01-13	24x12s	
	MIR	WISE	2070p121_ab41	2010-07-06	256 <sup>1,2</sup> /248 <sup>3,4</sup>	
	MIR/FIR	Spitzer/MIPS	30877/19167488	2007-07-13	14x2.6s; 16x10.5s	24, 70
	FIR	Herschel/PACS	1342224349-50	2011-07-17	445 s × 2 <sup>2</sup>	100, 160
3C 293	FIR	Herschel/SPIRE	1342234792	2011-12-17	307	
	UV	GALEX/FUV	AIS_238	2007-04-06	119.0	
	UV	GALEX/NUV	MISGCN3_02086_0229	2011-06-01	2632.3	
	Optical	SDSS	004623-6-0301	2004-05-12	53.9	Drift Mode
	NIR	2MASS	980310n1340068	1998-03-10	273	
	MIR	Spitzer/IRAC	3418/10922496	2005-06-11	24x30s	
	MIR	WISE	2082p318_ab41	2010-06-29	218	
	MIR/FIR	Spitzer/MIPS	82/4694016	2005-06-28	56x2.6s; 28x10.5s; 68x10.5s	24, 70, 160
MRK 668	UV	GALEX/FUV	GI1_056017_NGC5466	2007-05-01	1838.1	
	UV	GALEX/NUV	GI1_056017_NGC5466	2006-05-11	3529.1	
	Optical	SDSS	004646-6-0117	2004-05-22	53.9	Drift Mode
	NIR	2MASS	980505n0220209	1998-05-05	273	
	MIR	Spitzer/IRAC	30443/17639168	2006-07-10	10x2s	
	MIR	WISE	2125p287_ab41	2010-07-04	229	
	MIR/FIR	Spitzer/MIPS	30443/17640448	2006-07-14	14x2.6s; 16x3.2s	24, 70
	FIR	Herschel/PACS	1342223955-56	2011-07-11	445 s × 2 <sup>2</sup>	100, 160
	FIR	Herschel/SPIRE	1342234785	2011-12-17	307	

**Table A1**  
Observation Description

3C 305	UV	GALEX/(FUV;NUV)	AIS_23	2004-03-13	196.0		
	Optical	SDSS	001412-5-0275	2000-04-27	53.9	Drift Mode	
	NIR	2MASS	000221n0390150	2000-02-21	273		
	MIR	Spitzer/IRAC	3418/10923008	2004-11-25	24x30s		
	MIR	WISE	2212p636_ab41	2010-06-01	391 <sup>1,2</sup> /370 <sup>3,4</sup>		
	MIR/FIR	Spitzer/MIPS	82/4737280	2004-04-12	14x10s; 208x10.5s	24, 70	
	FIR	Herschel/PACS	1342223959-60	2011-07-11	445 s × 2 <sup>2</sup>	100, 160	
	FIR	Herschel/SPIRE	1342234915	2011-12-18	307		
3C 310	UV	GALEX/FUV	AIS_237	2007-04-10	175.0		
	UV	GALEX/NUV	MISGCSN3_21467_0238	2011-05-16	2373.0		
	Optical	SDSS	004588-4-0131	2004-04-22	53.9	Drift Mode	
	NIR	2MASS	990522n0590103	1999-05-22	273		
	MIR	Spitzer/IRAC	3418/10923264	2005-07-16	24x30s		
	MIR	WISE	2266p257_ab41	2010-07-22	315 <sup>1,2</sup> /303 <sup>3,4</sup>		
	FIR	Herschel/PACS	1342235116-17	2011-12-24	2020 s × 2 <sup>2</sup>	100, 160	
	FIR	Herschel/SPIRE	1342234778	2011-12-17	997		
3C 315	Optical	SDSS	004576-2-0703	2004-04-16	53.9	Drift Mode	
	NIR	2MASS	990527n0320103	1999-05-27	273		
	MIR	WISE	2283p257_ab41	2010-07-24	317 <sup>1,2</sup> /304 <sup>3,4</sup>		
	MIR/FIR	Spitzer/MIPS	82/4708864	2004-08-06	14x10s; 28x10.5s	24, 70	
	FIR	Herschel/PACS	1342224636-37	2011-07-21	895 s × 2 <sup>2</sup>	100, 160	
	FIR	Herschel/SPIRE	1342234777	2011-12-17	997		
	3C 317	UV	GALEX/(FUV;NUV)	GI3_103015_Abell2052	2007-06-04	2857.1	
		Optical	SDSS	003903-3-0318	2003-04-27	53.9	Drift Mode
NIR		2MASS	000428s0700044	2000-04-28	274		
MIR		Spitzer/IRAC	30659/18654464	2006-08-10	18x12s		
MIR		WISE	2288p075_ab41	2010-07-31	279 <sup>1,2</sup> /269 <sup>3,4</sup>		
MIR/FIR		Spitzer/MIPS	30659/18641664	2007-03-05	42x10s	24	
FIR		Herschel/PACS	1342237886-89	2012-01-05	840 s × 4 <sup>3</sup>	70, 100, 160	
FIR		Herschel/SPIRE	1342238322	2012-01-28	859		
3C 326N	UV	GALEX/FUV	AIS_135	2007-04-13	96.0		
	UV	GALEX/NUV	AIS_135	2005-06-17	247.1		
	Optical	SDSS	004633-2-0076	2004-05-14	53.9	Drift Mode	
	NIR	2MASS	000422n0520173	2000-04-22	273		
	MIR	Spitzer/IRAC	3418/10923776	2005-03-27	24x30s		
	MIR	WISE	2384p196_ab41	2010-02-10	168 <sup>1,2</sup> /157 <sup>3,4</sup>		
	MIR/FIR	Spitzer/MIPS	3418/10930432	2005-08-28	80x2.6s	24	
	FIR	Herschel/PACS <sup>d</sup>	1342248732-33	2012-07-27	2470 s × 2 <sup>2</sup>	100, 160	
PKS 1549-79	UV	GALEX/(FUV;NUV)	AIS_470	2006-08-16	109.0		
	NIR	2MASS	000408s0730068	2000-04-08	274		
	MIR	WISE	2376m788_ab41	2010-03-10	235 <sup>1,2</sup> /226 <sup>3,4</sup>		
	FIR	Herschel/PACS	1342225387-88	2011-07-24	445 s × 2 <sup>2</sup>	100, 160	
	FIR	Herschel/SPIRE	1342239890	2012-03-01	307		
	3C 338	UV	GALEX/(FUV;NUV)	NGA_NGC6166	2004-08-06	1437.0	
		Optical	SDSS	003225-4-0238	2002-06-09	53.9	Drift Mode
		NIR	2MASS	990603n0430162	1999-06-03	273	
MIR		Spitzer/IRAC	25/3860992	2004-07-06	30x200s		
MIR		WISE	2477p393_ab41	2010-02-13	204 <sup>1,2</sup> /196 <sup>3,4</sup>		
MIR/FIR		Spitzer/MIPS	20651/14957056	2005-08-29	80x2.6s	24	
FIR		Herschel/PACS	1342207019-22	2010-10-23	571 s × 4 <sup>3</sup>	70, 100, 160	
FIR		Herschel/SPIRE	1342207033	2010-10-24	721		
3C 386	UV	GALEX/(FUV;NUV)	AIS_121	2006-07-31	183.0		
	NIR	2MASS	990608n0730232	1999-06-08	273		
	MIR	Spitzer/IRAC	3418/10924800	2005-05-06	24x30s		
	MIR	WISE	2798p166_ab41	2010-04-01	162 <sup>1,2</sup> /150 <sup>3,4</sup>		
	MIR/FIR	Spitzer/MIPS	3418/12418048	2005-04-10	80x2.6s; 52x10.5s	24, 70	
	FIR	Herschel/PACS	1342231672-73	2011-10-30	670 s × 2 <sup>2</sup>	100, 160	
	FIR	Herschel/SPIRE	1342239789	2012-02-29	997		
	3C 424	UV	GALEX/(FUV;NUV)	AIS_242	2006-09-03	176.0	
NIR		2MASS	000806s0550233	2000-08-06	274		
MIR		WISE	3127p075_ab41	2010-05-09	151 <sup>1,2</sup> /138 <sup>3</sup> /139 <sup>4</sup>		
FIR		Herschel/PACS	1342233349-50	2011-12-01	2470 s × 2 <sup>2</sup>	100, 160	
FIR		Herschel/SPIRE	1342244149	2012-04-12	997		
IC 5063	UV	GALEX/(FUV;NUV)	GI3_087016_IC 5063	2007-06-25	2951.1		
	NIR	2MASS	000621s0070127	2000-06-21	274		
	MIR	Spitzer/IRAC	3269/12455680	2005-05-09	2x12s		
	MIR	WISE	3129m576_ab41	2010-04-18	163 <sup>1,2,3</sup> /140 <sup>4</sup>		
	MIR/FIR	Spitzer/MIPS	86/4858624	2005-05-20	28x2.6s	24	
	FIR	Herschel/PACS	1342216469-72	2011-03-20	276 s × 4 <sup>3</sup>	70, 100, 160	

**Table A1**  
Observation Description

	FIR	Herschel/SPIRE	1342206208	2010-10-11	445	
3C433	UV	GALEX/NUV	AIS_154	2011-10-09	128.0	No FUV obs.
	NIR	2MASS	971029n0280220	1997-10-29	273	
	MIR	WISE	3216p257_ab41	2010-05-25	167 <sup>1,2</sup> /156 <sup>3,4</sup>	
	FIR	Herschel/PACS <sup>d</sup>	1342232731- 32	2011-11-10	445 s × 2 <sup>2</sup>	100, 160
	FIR	Herschel/PACS <sup>d</sup>	1342219391-92	2011-04-19	266 s × 2 <sup>3</sup>	70, 100, 160
	FIR	Herschel/SPIRE	1342234675	2011-12-18	307	
3C436	UV	GALEX/(FUV;NUV)	AIS_40	2007-07-17	64.0/328.	
	Optical	SDSS	008155-3-0058	2009-11-17	53.9	Drift Mode
	NIR	2MASS	991110n0460080	1999-11-10	273	
	MIR	WISE	3257p287_ab41	2010-05-31	190 <sup>1,2</sup> /179 <sup>3,4</sup>	
	FIR	Herschel/PACS <sup>d</sup>	1342235316-17	2011-12-25	445 s × 2 <sup>2</sup>	100, 160
	FIR	Herschel/PACS <sup>d</sup>	1342257734-37	2011-04-19	266 s × 4 <sup>3</sup>	70, 100, 160
	FIR	Herschel/SPIRE	1342234676	2011-12-18	997	
3C459	UV	GALEX/(FUV;NUV)	AIS_149	2006-10-02	186.0	
	Optical	SDSS	007807-2-0076	2008-11-17	53.9	Drift Mode
	NIR	2MASS	000825s0250092	2000-08-25	274	
	MIR	WISE	3493p045_ab41	2010-06-13	129 <sup>1,2</sup> /122 <sup>3,4</sup>	
	MIR/FIR	Spitzer/MIPS	20233/14432512	2005-11-30	28x2.6s; 28x10.5s	24, 70
	FIR	Herschel/PACS	1342237979-80	2012-01-06	445 s × 2 <sup>2</sup>	100, 160
	FIR	Herschel/SPIRE	1342234756	2011-12-19	307	

<sup>a</sup> SDSS Obs. IDs are in the form of a 6 digit run number, followed by a one digit camera column, and ending in a four digit field number. 2MASS Obs. IDs are in the form of six digits dates (yyymmdd) followed by scan directions (n/s) followed by a three digits scan number and ending in a four digit image number, except for 3C84, 3C270, and 3C272.1. *Spitzer* Obs. IDs are given as Project ID/AOR number.

<sup>b</sup> If only one exposure time is given, it is the same for all bands. For 2MASS and WISE, we give the exposure in terms of the number of frames that were co-added to create the image. When different bands had different numbers of frames, the super-script indicates which bands the coverage indicates. Exposure times for PACS are given as (Time per Obs. ID) × (Number of Observations). PACS always observes at 160  $\mu\text{m}$  in conjunction with either 70  $\mu\text{m}$  or 100  $\mu\text{m}$ . <sup>1</sup> indicates all observations were done at 160  $\mu\text{m}$  and 70  $\mu\text{m}$ . <sup>2</sup> indicates all observations were performed at 160  $\mu\text{m}$  and 100  $\mu\text{m}$ . <sup>3</sup> indicates the observations are evenly split between the two modes (i.e. the 70 and 100  $\mu\text{m}$  bands were each observed for half of the total 160  $\mu\text{m}$  time).

<sup>c</sup> The 2MASS mosaics of these galaxies come from the Large Galaxy Atlas, which combines multiple observations and does not clearly indicate the dates and number of frames that went into each mosaic.

<sup>d</sup> 3C 84, 3C 236, 3C 326N, 3C 433, and 3C 436 were all observed twice by PACS, with different configurations of bands. For each galaxy, we combine all the available data at each wavelength.





**Table A2**  
Photometry

3C 326N	Opt. (mJy)	27.1 ± 0.9	87.7 ± 4.4	52.2 ± 1.7	...
	Opt./NIR (mJy)	73.1 ± 2.3	...	120. ± 27	...
	NIR (mJy)	116 ± 25	50.5 ± 1.5	58.9 ± 5.5	...
	MIR1 (mJy)	31.5 ± 1.5	26.4 ± 1.8	26.9 ± 1.0	...
	MIR2 (mJy)	< 320	21.5 ± 0.9	...	...
	FIR1 (Jy)	0.0968 ± 0.0122	...	0.133 ± 0.018	...
	FIR2 (Jy)	0.0872 ± 0.0127	0.0491 ± 0.0151	< 0.037	< 0.024
	UV/Opt. (mJy)	< 0.036	0.219 ± 0.065	...	...
	Opt. (mJy)	1.12 ± 0.09	...	2.38 ± 0.14	...
	Opt./NIR (mJy)	3.56 ± 0.17	4.24 ± 0.26	5.63 ± 1.24	...
PKS 1549-79	Opt. (mJy)	7.45	2.79 ± 0.14	3.16 ± 0.20	...
	Opt./NIR (mJy)	2.21 ± 0.50	1.69 ± 0.09	1.19 ± 0.07	...
	NIR (mJy)	< 8.3	0.524 ± 0.021	...	...
	MIR1 (mJy)	...	0.0073 ± 0.0022	0.0160 ± 0.0023	...
	MIR2 (mJy)	...	0.0192 ± 0.0026	< 0.017	< 0.017
	FIR1 (Jy)	< 0.43	0.0175 ± 0.0036	...	...
	FIR2 (Jy)	...	...	...	...
	UV/Opt. (mJy)	< 0.34	...	...	...
	Opt. (mJy)	...	...	...	...
	Opt./NIR (mJy)	0.360	15.2 ± 0.5	< 6.2	R: (4)
3C 338	NIR (mJy)	< 6.3	...	...	...
	MIR1 (mJy)	174 ± 10.	422 ± 106	68.9 ± 17.2	IRS 8 $\mu$ m <sup>c</sup>
	MIR2 (mJy)	...	...	1020 ± 150	IRS24 $\mu$ m <sup>d</sup> ; 60 $\mu$ m: (5)
	FIR1 (Jy)	...	...	0.928 ± 0.093	...
	FIR2 (Jy)	...	0.200 ± 0.023 <sup>1</sup>	0.096 ± 0.015 <sup>1</sup>	< 0.068 <sup>1</sup>
	UV/Opt. (mJy)	0.179 ± 0.020	5.04 ± 0.36	...	...
	Opt. (mJy)	...	...	59.8 ± 1.9	...
	Opt./NIR (mJy)	...	...	176 ± 17	...
	NIR (mJy)	210. ± 28	112 ± 6	77.9 ± 3.0	...
	MIR1 (mJy)	47.8 ± 8.4	69.9 ± 2.1	26.7 ± 1.3	...
3C 386	MIR2 (mJy)	< 39	33.2 ± 5.2	...	...
	FIR1 (Jy)	...	14.0 ± 0.6	...	...
	FIR2 (Jy)	...	< 0.058	< 0.14 <sup>1</sup>	< 0.066 <sup>1</sup>
	UV/Opt. (mJy)	< 0.73	< 0.15 <sup>1</sup>	...	...
	Opt. (mJy)	...	...	...	...
	Opt./NIR (mJy)	< 37	...	52.9 ± 5.1	R: (6)
	NIR (mJy)	82.5 ± 6.9	46.1 ± 1.4	45.4 ± 1.7	...
	MIR1 (mJy)	29.4 ± 1.7	8.06 ± 0.36	9.66 ± 0.40	...
	MIR2 (mJy)	< 20	7.78 ± 0.84	...	...
	FIR1 (Jy)	0.0428 ± 0.0091	...	0.108 ± 0.029	...
3C 424	FIR2 (Jy)	...	0.0787 ± 0.0218	< 0.057	< 0.045
	UV/Opt. (mJy)	< 0.052	...	...	...
	Opt. (mJy)	...	0.238 ± 0.710	...	V: (7)
	Opt./NIR (mJy)	...	...	< 4.3	...
	NIR (mJy)	< 7.6	0.992 ± 0.113	...	...
	MIR1 (mJy)	< 8.9	2.03 ± 0.66	0.692 ± 0.173	IRS 8 $\mu$ m <sup>c</sup>
	MIR2 (mJy)	...	...	< 0.0041	IRS24 $\mu$ m <sup>d</sup>
	FIR1 (Jy)	...	< 0.023	< 0.027 <sup>1</sup>	< 0.026 <sup>1</sup>
	FIR2 (Jy)	...	...	...	...
	UV/Opt. (mJy)	0.526 ± 0.054	1.59 ± 0.16	11.9 ± 2.4	U: (8)
IC 5063	Opt. (mJy)	39.6 ± 7.9	79.6 ± 15.9	...	B/V: (8)
	Opt./NIR (mJy)	...	...	...	...
	NIR (mJy)	211 ± 20.	121 ± 3	250. ± 14	...
	MIR1 (mJy)	156 ± 36	253 ± 34	148 ± 21	...
	MIR2 (mJy)	1410 ± 70	3380 ± 140	408 ± 102	IRS 8 $\mu$ m <sup>c</sup>
	FIR1 (Jy)	...	...	4.65 ± 0.60	...
	FIR2 (Jy)	...	2.22 ± 0.23	1.01 ± 0.11	0.365 ± 0.042

**Table A2**  
Photometry

3C 433	UV/Opt. (mJy)	< 0.13	1.05 ± 0.32	5.74 ± 1.14	B/V: (7)	
	Opt. (mJy)	0.368 ± 0.110	...	...	...	
	Opt./NIR (mJy)	...	...	...	...	
	NIR (mJy)	7.76 ± 1.28	8.84 ± 1.10	15.5 ± 0.5	IRS 8 $\mu$ m <sup>c</sup>	
	MIR1 (mJy)	...	25.1 ± 0.9	40.9 ± 10.2	IRS24 $\mu$ m <sup>d</sup>	
	MIR2 (mJy)	73.8 ± 5.7	131 ± 40	...	...	
	FIR1 (Jy)	...	0.329 ± 0.034	0.267 ± 0.027	...	
FIR2 (Jy)	...	0.116 ± 0.013	< 0.033	< 0.022		
3C 436	UV/Opt. (mJy)	< 0.052	< 0.13	0.762 ± 0.082	...	
	Opt. (mJy)	0.293 ± 0.056	...	1.54 ± 0.51	...	
	Opt./NIR (mJy)	...	1.28 ± 0.11	...	...	
	NIR (mJy)	2.36 ± 0.78	0.870 ± 0.063	...	...	
	MIR1 (mJy)	...	0.760 ± 0.125	0.539 ± 0.305	IRS 8 $\mu$ m <sup>c</sup>	
	MIR2 (mJy)	< 4.4	< 70	2.36 ± 0.76	IRS24 $\mu$ m <sup>d</sup>	
	FIR1 (Jy)	...	0.0187 ± 0.0023 <sup>j</sup>	0.0348 ± 0.0036 <sup>i</sup>	...	
	FIR2 (Jy)	...	0.0393 ± 0.0042 <sup>j</sup>	0.0217 ± 0.0043 <sup>j</sup>	< 0.014 <sup>j</sup>	
	3C 459	UV/Opt. (mJy)	0.0585 ± 0.0104	0.310 ± 0.060	0.828 ± 0.077	...
		Opt. (mJy)	...	0.549 ± 0.068	1.13 ± 0.27	...
Opt./NIR (mJy)		...	1.09 ± 0.08	...	...	
NIR (mJy)		1.58 ± 0.40	1.10 ± 0.09	1.53 ± 0.08	...	
MIR1 (mJy)		...	2.18 ± 0.44	...	...	
MIR2 (mJy)		13.0 ± 2.0	2.08 ± 0.16	4.27 ± 1.07	IRS 8 $\mu$ m <sup>c</sup>	
FIR1 (Jy)		0.611 ± 0.100	< 93	0.817 ± 0.082 <sup>j</sup>	...	
FIR2 (Jy)		...	0.634 ± 0.063 <sup>j</sup>	0.117 ± 0.013 <sup>j</sup>	0.0466 ± 0.0093 <sup>j</sup>	

<sup>a</sup> Upper limits ( $3\sigma$ ) are given when flux was not detected with at least  $3\sigma$  of confidence.

<sup>b</sup> Literature photometry is only obtained in the absence of observations in similar bands. References for literature photometry: (1) Varela et al. (2009), (2) Tremblay et al. (2010), (3) Golombek et al. (1988), (4) Drake et al. (2004), (5) Moshir et al. (1990), (6) Martel et al. (1999), (7) Smith & Heckman (1989), and (8) de Vaucouleurs et al. (1991).

<sup>c</sup> When *Spitzer* did not observe a galaxy with the IRAC instrument, we use IRAC 8 $\mu$ m photometry estimated from the IRS spectrum, as part of the enhanced products of the Spitzer Heritage Archive. We also use this 8 $\mu$ m photometry for IC 5063 whose IRAC image is saturated.

<sup>d</sup> When *Spitzer* did not observe a galaxy with the MIPS instrument, we use MIPS 24 $\mu$ m photometry estimated from the IRS spectrum as part of the enhanced products of the Spitzer Heritage Archive. We also use this 24 $\mu$ m photometry for 3C 310 whose flux was not detected with  $3\sigma$  confidence on the MIPS image.

<sup>e</sup> Used in the complete absence of *Herschel* data (3C 270, 3C 272.1, 3C 293) or in the absence of either PACS or MIPS 70  $\mu$ m observations (PKS 1549-79).

<sup>f</sup> Used in the absence of PACS 70 $\mu$ m photometry.

<sup>g</sup> Used in the complete absence of *Herschel* data (3C 270, 3C 272.1, 3C 293).

<sup>h</sup> 3C 218 was only observed by the IRAC instrument at 4.5  $\mu$ m and 8.0  $\mu$ m.

<sup>i</sup> Although detected at  $> 3\sigma$ , we cannot fully disentangle the emission from the host galaxy from that of the other galaxies in the nest, so we consider this measurement an upper limit.

<sup>j</sup> These photometry were extracted with the point source aperture (12'' for PACS bands; 22'' for 250  $\mu$ m; 30'' for 350  $\mu$ m; 42'' for 500  $\mu$ m), which is larger than the aperture used at shorter wavelengths.

<sup>k</sup> 3C 218 has a nearby (30'') source that likely contaminates the 500  $\mu$ m photometry, so this photometry should be used with caution.

<sup>l</sup> These photometry were extracted with the point source aperture to limit contamination by diffuse foreground structure.



## B. ADDITIONAL X-RAY OBSERVATIONS

At the time of our last paper (Lanz et al. 2015), Mrk 668 did not have a non-proprietary *Chandra* observation. PKS 1549-79 has still not yet been observed with *Chandra*. For completeness, we have reduced the newly released *Chandra* observation of Mrk 668 in the same manner and use the *XMM-Newton* observation of PKS 1549-79 to estimate diffuse X-ray emission. Below, we summarize these observations and the reduction done.

## B1. Mrk 668

Mrk 668 was observed with *Chandra* for 34.6 ks on 2014 September 04 (ObsID 16071; P.I. A. Siemiginowska), and will be discussed in detail by Sobolewska et al. (2016, in preparation). We retrieved the observation from the *Chandra* archive and reduced it in the manner described in Lanz et al. (2015). The X-ray emission is clearly dominated by the central source. However, the hardness ratio ( $HR = (H-S)/(H+S)$  where H is the net counts in the 2–8 keV band and S is the net counts in the 0.5–2 keV band), of that emission is softer at  $-0.12$  than expected for an AGN, suggesting that small scale diffuse emission may also be present. If we exclude that central source, we do not have sufficient counts remaining to fit a spectrum.

We therefore sought to estimate the diffuse X-ray luminosity in two ways. First, we measured the net (background-subtracted) count rate in the aperture, excluding the central  $1''0$  (in the same manner as was done for the galaxies in Lanz et al. 2015), in the 0.5–8 keV, 0.5–2 keV, and 2–8 keV bands. Based on the hardness ratio which provides a sense of the temperature, we estimate its flux assuming a thermal (APEC; Smith et al. 2001) model with the temperature from another radio galaxy with a similar hardness ratio (3C 433;  $\log T = 7.05$ ,  $kT = 0.967$  keV), using the WebPIMMS tool. We assume solar metallicity and a fixed foreground absorption due to the Milky Way’s ISM ( $1.6 \times 10^{20} \text{ cm}^{-2}$ , Kalberla et al. 2005). We also use the 2–8 keV counts within the central  $1''0$  aperture to estimate the AGN’s 2–10 keV luminosity, assuming a power-law with  $\Gamma = 1.7$ .

Second, we extracted a spectrum from the entire aperture (including the central source). We fit a combination of thermal models and an absorbed power-law, all subject to absorption due to the Milky Way’s ISM. Our best model required two thermal components (0.33 keV and 1.6 keV) as well as an absorbed power-law ( $\Gamma = 1.7$ ,  $N_{\text{H}} = 8.3 \times 10^{21} \text{ cm}^{-2}$ ). From this fit, we calculate the 0.5–8 keV luminosity of the diffuse emission (thermal components) and the unabsorbed 2–10 keV emission of the AGN (power-law component).

These two methods yield consistent values for both the diffuse ( $\log(L_{0.5-8 \text{ keV}}/\text{erg s}^{-1}) = 41.4 - 41.7$ ) and the AGN ( $\log(L_{2-10 \text{ keV}}/\text{erg s}^{-1}) = 42.3 - 42.5$ ) emission. Our AGN luminosity is in good agreement with the measurement of Guainazzi et al. (2004), and the ratio of  $L(\text{H}_2)/L_{\text{X,diffuse}}$  that we measure for Mrk 668 is consistent with those of other radio MOHEGs (see Fig. 9 of Lanz et al. 2015). Therefore, we believe that our modeling has yielded reliable values of the diffuse X-ray emission.

## B2. PKS 1549-79

Since *XMM-Newton* has a much poorer spatial resolution than *Chandra*, we cannot hope to achieve the same spatial separation between the AGN and any diffuse emission in the *XMM-Newton* observation of PKS 1549-79. Instead, we estimate the diffuse emission based on a spectral decomposition. We attribute the power-law component to the AGN and any thermal component to the diffuse emission. As discussed in the previous section, we found good agreement for the estimates of diffuse X-ray luminosity from spatial and spectral decompositions for Mrk 668.

PKS 1549-79 was observed with *XMM-Newton* for 86.72 ks on 2008 September 22 (ObsID 0550970101). We retrieved and analyzed the data taken with the European Photon Imaging Camera (EPIC; Jansen et al. 2001) on both the metal oxide semiconductor (MOS) CCDs and the pn CCDs. There is significant background flaring in the last  $\sim 30$  ks, which we filtered out reducing the exposure time to 55.15 ks (MOS1/MOS2) and 53.69 ks (pn). We only retained events with energies between 0.4 and 10 keV with patterns between 0 and 12. We extracted the spectrum in a  $45''$  aperture in each data set and combined them to create the EPIC spectrum. We selected this aperture size, despite being smaller than the aperture in Table 1 because it contains all of the X-ray emission and does not cross the pn chip gap (as the Table 1 aperture would). This aperture contains  $\sim 55000$  counts, dominated by the hard component, likely the AGN.

Spectral modeling was accomplished using the *SHERPA* packages of *CIAO*. We fit a combination of thermal (APEC; Smith et al. 2001) and an absorbed power-law, all of which is subject to a fixed foreground absorption due to the Milky Way’s ISM ( $9.4 \times 10^{20} \text{ cm}^{-2}$ , Kalberla et al. 2005) as well as a fitted intrinsic absorption. Our best model (well fit with  $\chi^2/\text{dof} = 949/1181$ ) requires two thermal components (0.27 keV and 2.3 keV), a power-law index of  $\Gamma = 2.0$ , an intrinsic column of  $N_{\text{H}} = 1.5 \times 10^{22} \text{ cm}^{-2}$ , and an additional column of  $N_{\text{H}} = 3.5 \times 10^{20} \text{ cm}^{-2}$  on the power-law component.

As noted by O’Brien et al. (2010), the *XMM-Newton* spectrum is dominated by its buried AGN. Indeed, we find that 96% of the 0.5–8 keV luminosity comes from the power-law component. From our fit, we measure the 2–10 keV luminosity of the absorption-corrected (both intrinsic and foreground) power-law component as well as the 0.5–8 keV luminosity of the foreground-absorption corrected (as was done for the galaxies in Lanz et al. 2015) thermal component (given in Table 2). We find that our AGN luminosity is in good agreement with that reported by González-Martín & Vaughan (2012) and that the diffuse X-ray luminosity would place PKS 1549-79 in the region occupied by radio MOHEGs in our plot of  $\text{H}_2$  luminosity versus diffuse X-ray luminosity (Figure 9 of Lanz et al. 2015). As a result, we believe that our spectral decomposition provides a reliable value of the diffuse X-ray luminosity.